Tropospheric Ozone Precursors: Global and Regional Distributions, Trends, and Variability

Yasin Elshorbany[1*], Jerald R. Ziemke[2], Sarah Strode[2,3], Hervé Petetin[4], Kazuyuki Miyazaki[5], Isabelle De Smedt[6], Kenneth Pickering[7], Rodrigo J. Seguel[8], Helen Worden[9], Tamara Emmerichs[10], Domenico Taraborrelli[10], Maria Cazorla[11], Suvarna Fadnavis[12], Rebecca R. Buchholz[9], Benjamin Gaubert[9], Néstor Y. Rojas[13], Thiago Nogueira[14], Thérèse Salameh[15], Min Huang[16]

[*]Correspondence to: elshorbany@usf.edu

[1] School of Geosciences, College of Arts and Sciences, University of South Florida, St. Petersburg, FL, USA

[2] NASA Goddard Space Flight Center, Greenbelt, Maryland, USA

[3]Goddard Earth Sciences Technology and Research (GESTAR II), Maryland, USA

[4]Earth Sciences Department, Barcelona Supercomputing Center, Barcelona, Spain

[5]Jet Propulsion Laboratory, California Institute of Technology, Pasadena CA

[6]BIRA-IASB, Ringlaan 3 Av. Circulaire, 1180 Brussels, Belgium

[7]Dept. of Atmospheric and Oceanic Science, University of Maryland, College Park, MD USA

[8]Center for Climate and Resilience Research, Department of Geophysics, Faculty of Physical and Mathematical Sciences University of Chile, Chile.

[9]Atmospheric Chemistry Observations and Modeling (ACOM), National Center for Atmospheric Research (NCAR), Boulder CO, USA.

[10]Institute of Energy and Climate Research, IEK-8: Troposphere, Forschungszentrum Jülich, Jülich, Germany.

[11]Universidad San Francisco de Quito USFQ, Instituto de Investigaciones Atmosféricas, Diego de Robles y Av Interoceánica, Quito, Ecuador.

[12]Center for Climate Change Research, Indian Institute of Tropical Meteorology, MoES, Pune, India.

[13]Department of Chemical and Environmental Engineering, Universidad Nacional de Colombia, Bogota, Colombia.

[14]University of São Paulo, São Paulo, Brazil.

[15] IMT Nord Europe, Institut Mines-Télécom, Univ. Lille, Centre for Energy and Environment, 59000, Lille, France.

[16] Earth System Science Interdisciplinary Center, University of Maryland, College Park, MD, USA.

36   **Abstract**

37   Tropospheric ozone results from in-situ chemical formation and stratosphere-troposphere
38   exchange (STE), with the latter being more important in the middle and upper troposphere than in
39   the lower troposphere. Ozone photochemical formation is nonlinear, and results from the oxidation
40   of methane and non-methane hydrocarbons (NMHCs) in the presence of nitrogen oxide
41   (NO_x=NO+NO_2). Previous studies showed that O_3 short- and long-term trends are nonlinearly
42   controlled by near-surface anthropogenic emissions of carbon monoxide (CO), volatile organic
43   compounds (VOCs), and nitrogen oxides, which maybe also impacted by the long-range transport
44   (LRT) of O_3 and its precursors. In addition, several studies have demonstrated the important role
45   of STE in enhancing ozone levels, especially in the midlatitudes. In this article, we investigate
46   tropospheric ozone spatial variability and trends from 2005 to 2019 and relate those to ozone
47   precursors on global and regional scales. We also investigate the spatiotemporal characteristics of
48   the ozone formation regime in relation to ozone chemical sources and sinks. Our analysis is based
49   on remote sensing products of the Tropospheric Column of Ozone (TrC-O_3) and its precursors,
50   nitrogen dioxide (TrC-NO_2), formaldehyde (TrC-HCHO), and total column of CO (TC-CO) as
51   well as ozonesonde data and model simulations. Our results indicate a complex relationship
52   between tropospheric ozone column levels, surface ozone levels, and ozone precursors. While the
53   increasing trends of near-surface ozone concentrations can largely be explained by variations in
54   VOC and NO_x concentration under different regimes, TrC-O_3 may also be affected by other
55   variables such as tropopause height and STE as well as LRT. Decreasing or increasing trends in
56   TrC-NO_2 have varying effects on the TrC-O_3, which is related to the different local chemistry in
57   each region. We also shed light on the contribution of NO_x lightning and soil NO and nitrous acid
58   (HONO) emissions to trends of tropospheric ozone on regional and global scales.

59

2

1. Introduction

Tropospheric ozone (O_3) is an important air pollutant due to its diverse effects on air quality, ecosystem (Mills et al., 2018), health (Lefohn et al., 2018; Fleming et al., 2018), and climate (Boucher et al., 2013; Myhre et al., 2013; Zanis et al., 2022). O_3 is a photochemical product that results from the oxidation of methane (CH_4) and non-methane hydrocarbons (NMHCs) in the presence of nitrogen oxides (NO_x). Tropospheric ozone burdens can also be affected by stratosphere-troposphere exchange (STE) (Stohl et al., 2003; Zeng et al., 2010; Trickl et al., 2011; Li et al., 2024) and long-range transport (LRT) of ozone (e.g., Hov et al., 1978; Ravetta et al., 2007; Itahashi et al., 2020). O_3 is considered a short-lived climate forcer (SLCF) and is the third-most important greenhouse gas with an effective radiative forcing of ($0.47^{+0.23}_{-0.23}$) W m^{-2}; Forster et al., 2021). Since the mid-1990s, free tropospheric ozone trends based on in situ measurement and satellite retrievals have increased with high confidence (HC) by 1-4 nmol mol^{-1} $decade^{-1}$ across the northern mid-latitudes and 1-5 nmol mol^{-1} $decade^{-1}$ within the tropics (Gulev et al., 2021). In the Southern Hemisphere, with more limited observation coverage compared with the Northern Hemisphere, the tropospheric column ozone shows an increase since the mid-1990s by less than 1 nmol mol^{-1} $decade^{-1}$ with medium confidence at southern mid-latitudes (Gulev et al., 2021, Cooper at al., 2020). Tropospheric O_3 short- and long-term trends are nonlinearly controlled by anthropogenic emissions of carbon monoxide (CO), volatile organic compounds (VOCs), and nitrogen oxides ($NO_x=NO+NO_2$) as well as STE, especially in the midlatitudes (Li et al., 2024). Meteorological parameters such as wind speed and wind direction may also enhance the LRT of O_3, affecting regional ozone burdens, especially in the free troposphere (e.g., Glotfelty et al, 2014; Itahashi et al., 2020). Methane, with an assessed total atmospheric lifetime of 9.1 ± 0.9 years (Szopa et al., 2021), is also a crucial driver of tropospheric ozone (Fiore et al., 2002; Isaksen et al., 2014). Its accelerated growth rate of 7.6 ± 2.7 nmol mol^{-1} yr^{-1} between 2010 and 2019 (Canadell et al., 2021) is largely driven by anthropogenic activities (Szopa et al., 2021). NOAA GML observations of methane (NOAA, 2024) show that methane concentrations in the atmosphere have increased sharply since 2005 (an 8% increase from 2005 to 2023). Future scenarios show that emission control measures can influence future changes to air pollutants. Although the global increases in CH_4 abundance may offset benefits to surface O_3 from local emission reductions (Fiore et al., 2002; Shindell et al., 2012; Wild et al., 2012; Szopa et al., 2021), recent reports (e.g., Itahashi et al., 2020; Zanis et al., 2022), showed the dominant role of precursor emission changes in projecting surface ozone concentrations under future climate change scenarios. In this study, we investigate the relation between ozone trends and the trends of its precursors, with a focus on NO_2, CO, and HCHO.

Coupled Model Intercomparison Project Phase 6 (CMIP6) overestimates observed surface O_3 concentrations in most regions, with larger variability over Northern Hemisphere (NH) continental regions (e.g., Tarasick et al., 2019; Turnock et al., 2020). CMIP6 models simulate large increasing trends of surface concentrations of O_3 and $PM_{2.5}$ in East and South Asia with an annual mean increase of up to 40 ppb and 12 μgm^{-3}, respectively, over the historical periods (1850-2014; Turnock et al., 2020). However, these studies found also that CMIP6 models consistently underestimate $PM_{2.5}$ concentrations in the NH, especially during the winter months, and with larger variability near natural source regions, indicating missing sources (e.g., HONO) of O_3 (e.g., Elshorbany et al., 2014).

Satellite observations have the advantage of large spatial and consistent temporal coverage. Tropospheric columns of ozone (TrC-O_3), in Dobson unit (1 DU=2.69×10^{20} molecules m^{-2}),

are usually used to represent tropospheric ozone levels. The tropospheric column of a species is the species' concentration integrated from the surface to the top of the troposphere, the tropopause. The tropopause height is dynamically changing, and it varies over time, increasing or decreasing as a function of several factors, including tropospheric and stratospheric temperature (warming or cooling). Steinbrecht et al (1998) found that observed tropospheric warming of 0.7 ± 0.3 K per decade leads to an increase in the tropopause high and a decrease (at a rate of 16 DU/decade) in the observed column ozone levels. Similarly, after removing the variations related to major natural forcings, including volcanic eruptions, ENSO (El Niño–Southern Oscillation), and QBO (Quasi–Biennial Oscillation), Meng et al. (2021) concluded that a continuous rise of the tropopause in the Northern Hemisphere (NH) from 1980 to 2020 is evident, which they related mainly to tropospheric warming caused by anthropogenic emissions. Steinbrecht et al (1998) and Meng et al. (2021) calculate the same rate of tropopause increase for the periods 1980-2000 and 1980-2020, respectively. We investigate the trends in TrC-O_3 and ozone precursors at different column depths and determine their relationships.

Global models play a vital role in interpreting the observed trends in ozone precursors, verifying the consistency of emission inventories with observed precursor concentrations, and relating trends in ozone precursor emissions to ozone trends. Because satellite measurements are often sensitive to species concentrations above the surface, models provide additional information on the vertical distribution of ozone precursors needed to relate emissions or surface trends to a column or free tropospheric observations. For example, chemical transport models are used to relate Ozone Monitoring Instrument (OMI) NO_2 columns to surface NO_2 concentrations and their trends over the United States (e.g. Lamsal et al 2008, 2015; Kharol et al, 2015) since they provide vertical information on the NO_2 distribution. Models are also used to infer NO_x emission trends from observations (e.g. Richter et al., 2005; Stavrakou et al., 2008; Miyazaki et al, 2016) or to examine whether simulations driven by state-of-the-art emissions inventories can reproduce observed changes in NO_x (Itahashi et al., 2014; Godowitch et al, 2010). Models also provide insight into the role of background NO_2 versus local sources in relating satellite-observed NO_2 columns to NO_x emissions changes (Silvern et al, 2019). Similarly, global models are vital for understanding trends in CO, since the lifetime of CO allows both local emissions and long-range transport and the global background to influence regional trends of CO and O_3. Duncan and Logan (2008) attributed the decreasing CO in the NH from 1998-1997 to decreasing European emissions and highlighted the role of Indonesian fires in driving interannual variability. Numerical models can also be used to assimilate satellite CO observations to invert for CO emission fluxes, often highlighting differences between bottom-up and top-down inventories (e.g., Kopacz et al., 2010; Fortems-Cheiney et al., 2011; Elguindi et al., 2020; Gaubert et al., 2020). For instance, several modeling studies found that the increasing emissions from China in recent years in some emission inventories were inconsistent with the negative trends observed by MOPITT (Yin et al, 2015; Strode et al., 2016; Zheng et al, 2019), while the decreases over the United States and Europe are supported by the observed decrease in CO. Jiang et al (2017) and Zheng et al (2019) also found that a decrease in biomass burning contributes to the negative CO trend in the NH. Mean calculated O_3 burden using CMIP6 simulation (Griffiths et al, 2021) revealed an increase of 44% from 1850 to the mean of the period of 2005-2014 and by another 17% until 2100 using the SSP370 experiments. Other sources of NO_x such as lightning and soil emissions play an important role in controlling the O_3 budget, especially in low-NO_x regions. We investigate these sources and the role they play in determining O_3 trends and variability on regional and global scales, as well as their determining factors.

153 Previous literature demonstrates the importance of controlling the emissions of ozone
154 precursors to effectively reduce surface O_3 levels. Therefore, a thorough and rigorous
155 understanding of the trends and variability for O_3 precursors is of paramount importance for a
156 global abatement strategy of O_3 levels. In this study, we use ozonesonde, remote sensing, and
157 global models to evaluate tropospheric O_3 and O_3 precursor trends of CO, HCHO, and NO_2,
158 on regional and global scales.

159 2.   Methodology

160 2.1. Trend Analysis

161 We analyze the historical trends of tropospheric ozone and its precursors CO, NO_2, and HCHO,
162 from 2005 to 2019. For trend analysis, we use two methods, the Quantile regression (QR)
163 method (Chang et al., 2023), and the Weighted Least Squares (WLS). For NO_2, CO, and HCHO
164 trends are calculated based on the QR method (Chang et al., 2023), as follows: (1) we first
165 compute the deseasonalized monthly time series of NO_2 and HCHO tropospheric columns
166 (hereafter referred to as TrC-NO_2, TrC-HCHO), and CO atmospheric column (TC_CO), (2) we
167 use the quantile regression method for computing the trend, focusing here on the median, and (3)
168 uncertainties at a 95% confidence level are estimated using the block bootstrapping approach,
169 through 1000 iterations with blocks size of $N^{0.25}$ with N the number of monthly values. They are
170 calculated over a 1°x1° grid and only in cells where at least 75% of the monthly values are
171 available. TC_CO column (see sec. 2.2.1) time series trends are also calculated as Weighted
172 Least Squares (WLS) of the monthly anomaly, weighted by the monthly regional standard
173 deviation (for comparison with the QR method). The tropospheric ozone column (TrC-O_3),
174 trends are calculated based on the WLS method. Tropospheric columns of satellite observations
175 are calculated based on the WMO thermal definition of the tropopause. To account for varying
176 tropospheric column definitions used in previous literature, we also evaluate the trends at varying
177 column depths.

178 2.2. Data resources

179 In this section, we present the different data repositories and their characteristics.

180 2.2.1.   Satellite data

181 A list of the applied satellite data products and their resolution is shown in Table 1. For
182 Tropospheric ozone data, we use the Ozone Monitoring Instrument/Microwave Limb Sounder
183 (OMI/MLS) product (Ziemke et al., 2006). The OMI/MLS product is the residual of the OMI total
184 ozone column and the MLS stratospheric ozone column, available as gridded monthly means. The
185 OMI/MLS tropospheric column ozone product applies all necessary data quality flags to both OMI
186 total ozone and MLS profile ozone; the OMI/MLS product further includes cloud filtering by
187 omitting all scenes with OMI reflectivity greater than 0.30. The tropospheric NO_2 column
188 retrievals used were the QA4ECV project (http://www.qa4ecv.eu/ecvs) version 1.1 level 2 (L2)
189 product for OMI (Boersma et al., 2017a), GOME-2 (Boersma et al., 2017b), and SCIAMACHY
190 (Boersma et al., 2017c). The ground pixel sizes of the OMI, GOME-2, and SCIAMACHY
191 retrievals are 13 km×24 km, 80 km×40 km, and 60 km×30 km, with local Equator overpass times
192 of 13:45, 09:30, and 10:00 LT, respectively. We also use HCHO tropospheric columns retrieved
193 from OMI (De Smedt et al. 2018) from the QA4ECV project. Atmospheric total column CO
194 daytime observations were obtained from the MOPITT instrument aboard the Terra Satellite
195 (Barret et al., 2003; Buchholz et al., 2017). Monthly daytime L3 data were obtained at 1º gridded
196 horizontal resolution from the NASA Langley Research Center Atmospheric Science Data Center

197 (ASDC, 2024), using version 9 (V9) retrievals, and the joint near-infrared/thermal-infrared product
198 (Deeter et al., 2022). Low-quality data were excluded by applying the provided quality flag.

199

200 Table 1 Satellite data products and their reference periods.

Parameter	Resolution (Satellite pixel size)	Instrument/Platform	Reference Period	Reference
NO$_2$	1°x1° (13 km x 24 km)	OMI/Aura	2005–2020	Boersma et al., 2017a
NO$_2$	1°x1° (40 km x 80 km)	GOME-2/METOP-A	2007–2018	Boersma et al., 2017b
NO$_2$	1°x1° (30 km x 60 km)	SCIAMACHY/ENVISAT	2005–2011	Boersma et al., 2017c
CO	1°x1° (22 km x 22 km)	MOPITT/TERRA	2002–2020	Deeter et al., 2022
HCHO	1°x1° (13 km x 24 km)	OMI/Aura	2004–2020	De Smedt et al., 2018
Ozone	1°x1°	OMI/MLS	2004–2020	Ziemke et al., 2006

201

2.2.2. Ozonesonde Data

203 Direct sampling of ozone throughout the atmospheric column by ozonesondes on board of high-
204 altitude balloons is a primary source of information of the ozone abundance and changes in the
205 free troposphere. Ozonesonde data have been used extensively for satellite ozone product
206 validations, trend analyses, and as a priori climatology profiles for satellite retrieval algorithms
207 (McPeters and Labow, 2012; Labow et al., 2015; Hubert et al., 2021; Christiansen et al., 2022;
208 Newton et al., 2016). Ozonesondes networks around the globe have been providing the ozone
209 community with accurate in situ measurements of high vertical resolution (100-m) for the last 5
210 decades in the Northern Hemisphere (Krizan and Lastovicka, 2005), nearing 3 decades at
211 stations in the tropics (Thompson et al., 2017), and in the last decade, new efforts are
212 contributing with data from undersampled regions such as the tropical Andes (Cazorla and
213 Herrera, 2022). Other important contributions include dedicated campaigns for regional studies
214 (e.g. Newton et al., 2016; Fadnavis et al., 2023). Figure 1 shows a map with ozonesonde stations
215 around the globe whose data are publicly available from data providers (station names,
216 coordinates, and links for data access in the Supplementary Material, Table S1). In this work, we

217 present a review of ozonesonde trends calculated and published in previous studies (Wang et al.,
218 2022 and Christiansen et al., 2022).

219
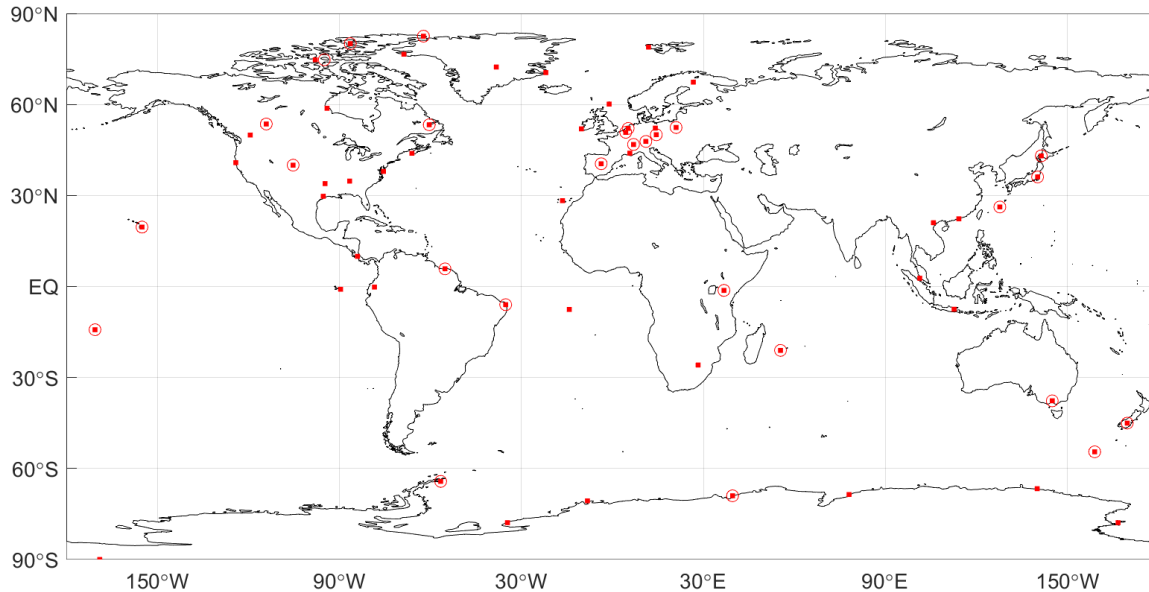
221 Figure 1: Ozone-sounding stations around the globe (red squares) whose data are publicly
222 available (Table S1). Stations that meet the criteria to calculate trends (Wang et al., 2022) are
223 circled in red.

224

225 **2.2.3.   Model simulations of ozone precursors and their vertical distribution**

226 Model simulations provide information on the vertical distribution of trace gases that can help
227 interpret the observed columns. Here, we use a Goddard Earth Observing System (GEOS) Earth
228 System Model (Molod et al, 2015) simulation run with the GMI chemistry mechanism (Duncan
229 et al, 2007; Strahan et al, 2007; Nielsen et al, 2017) to simulate the contributions of the lower,
230 middle, and upper troposphere to the tropospheric columns of ozone and its precursors. The
231 model configuration is described in Fisher et al (2024) and summarized here. The MERRA-2
232 reanalysis (Gelaro et al., 2017) constrains the GEOS-GMI meteorology. The GEOS-GMI
233 meteorology is replayed to the MERRA-2 meteorology as described in Orbe et al (2017).
234 Anthropogenic emissions of NO_2, CO, and VOCs are based on the MACCity inventory (Granier
235 et al, 2011) through 2010 and the RCP8.5 emissions afterward, with NO_2 emissions scaled based
236 on OMI. The emissions are downscaled to higher resolution using the EDGAR 4.2 emission
237 inventory (Janssens-Maenhout et al., 2013). Biomass burning emissions for the analysis period
238 come from the Fire Energetics and Emissions Research (FEER) product (Ichoku and Ellison,
239 2014). Liu et al (2022) evaluated another GEOS simulation with GMI chemistry with satellite
240 observations of $TrC-O_3$, $TrC-NO_2$, TrC-HCHO, and TC-CO.

241 **3.   Data Analysis and Discussion**

242 **3.1. $TrC-O_3$ Sensitivity to Tropopause**

243 Calculated $TrC-O_3$ depends on several factors such as tropospheric ozone levels, atmospheric
244 warming (e.g., due to GHG emissions) or cooling (stratospheric or tropospheric (e.g., after major
245 volcanic eruptions), and tropopause height (TH). Atmospheric warming or cooling can lead to a

246   decrease or an increase, respectively, of TrC-O_3 due to the respective change in the TH. Several
247   methods are used to determine the TH. The WMO thermal definition for the first TH, the lowest
248   altitude level at which the lapse rate decreases to 2° K km^{-1} or less, provided that the average
249   lapse rate between this level and all higher levels within 2 km does not exceed 2° K km^{-1}. A
250   second tropopause may be also found if the lapse rate above the first tropopause exceeds $3°K$
251   km^{-1} (WMO, 1992; Hoffmann and Spang (2022). Other studies define the TH based on fixed
252   pressure levels (from ground to 150, 200, 300, and 400 hPa). Mean OMI/MLS TrC-O_3 values in
253   July (2005-2019) calculated based on the WMO thermal definition, are shown in Figure 2. TrC-
254   O_3 values are comparable to previously reported CMIP6 and satellite measurements (Griffiths et
255   al., 2021). Partial ozone columns (OC) calculated from the ground to different pressure levels,
256   150, 200, and 300 hPa show increasing OC values with increasing column depth, with calculated
257   OC at 150 and 200 hPa being the closest to the TrC-O_3 WMO values, still overestimating OC in
258   the northern hemisphere (50-90° N), especially for the 150 hPa OC, see Figure 2.

259
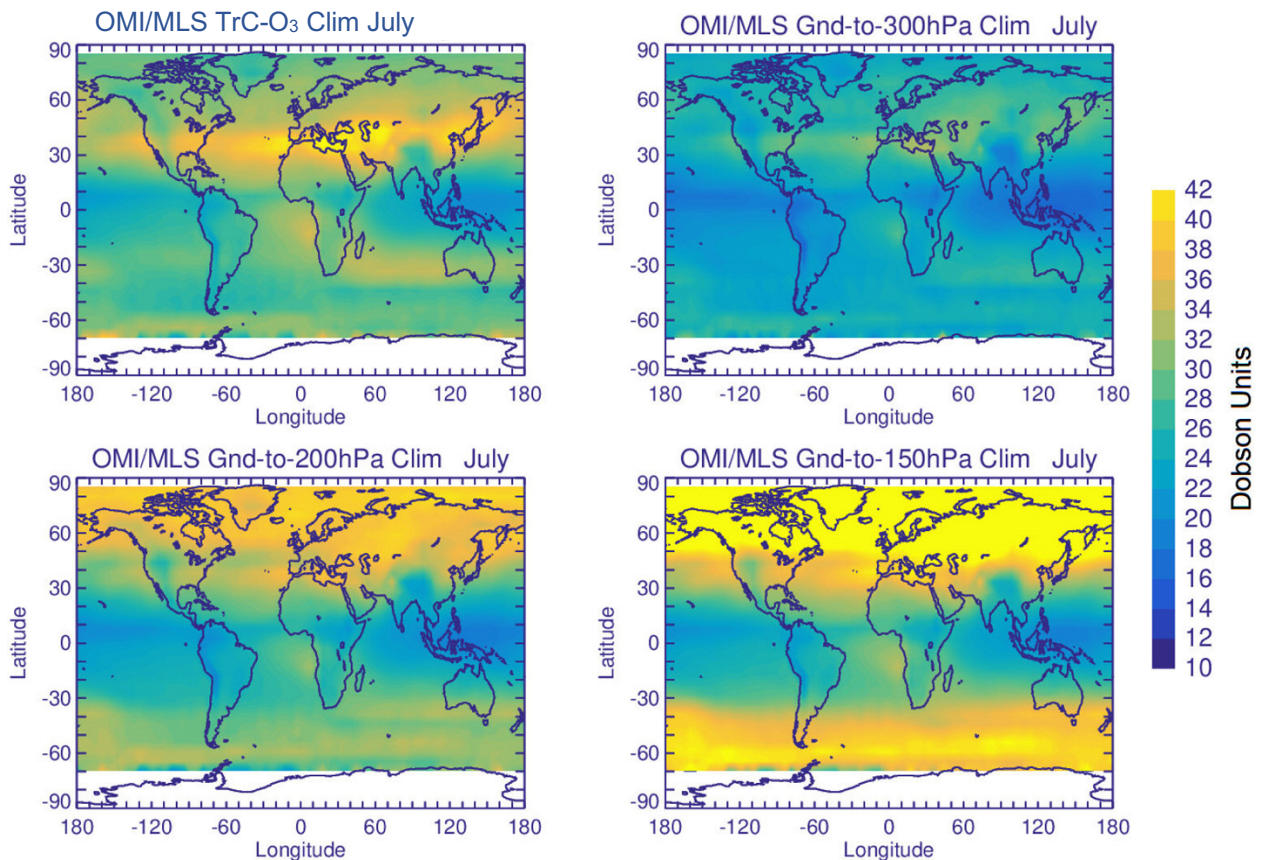
261   Figure 2: Global Mean (2005-2019) Column Ozone based on the WMO definition, and for
262   different column depths.

263

264   Steinbrecht et al (1998) found that observed tropospheric warming of 0.7± 0.3 K per decade
265   leads to an increase in the TH and a decrease in total ozone. They also calculated a decrease of
266   16 DU per kilometer increase in TH. These results indicate the importance of TH on calculated
267   long-term ozone trends. This could also affect comparisons between trends calculated based on
268   different TrC-O_3 definitions and near-surface ozone levels. The time series of deseasonalized TH
269   from 2004 to 2021 are shown in Figure 3 together with their zonal mean trends. Trends in TH are

270 positive reaching 60 meters/decade except in a narrow band in the tropics from 10ºS to 20ºN and
271 at 30ºS, where TH decreases at a rate up to 30 meters/decade. TH in the tropical regions is also
272 characterized by high variability (see Figure 3). These results are also consistent with recent
273 reports showing a positive trend of TH from 20-80ºN at a rate of 50-60 m/decade (Meng et al.,
274 2021). They related this increase primarily to tropospheric warming. These results show that
275 using a fixed pressure level for the tropopause may not be accurate given the change in TH over
276 time. In the following sections, tropospheric columns will be calculated based on the WMO
277 tropopause definition.

278
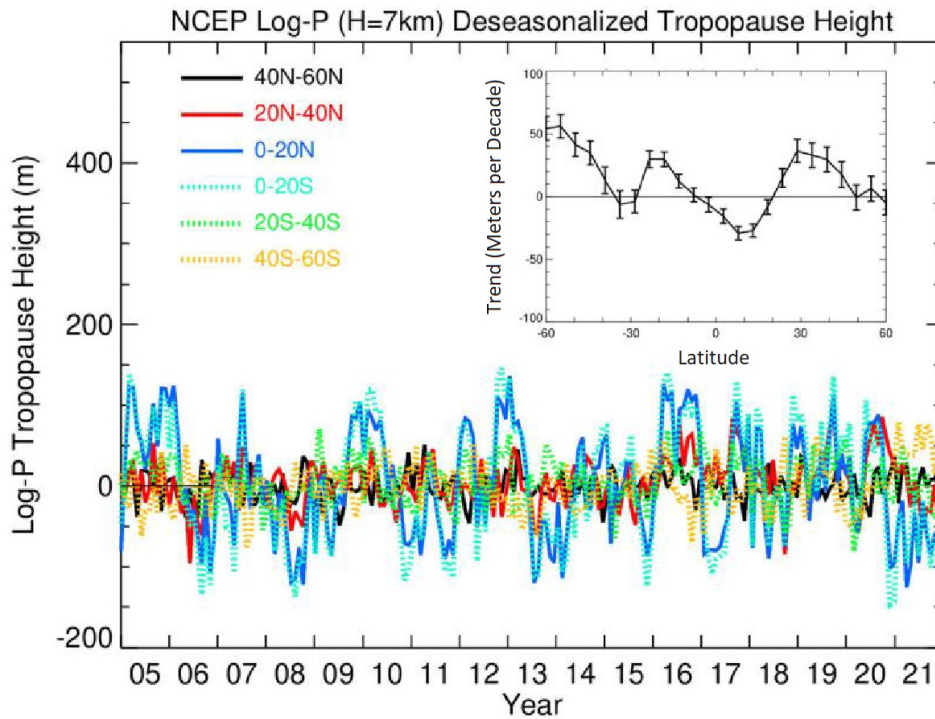
279
280 Figure 3: National Centers for Environmental Prediction (NCEP) WMO (2K/km) tropopause
281 log-P height time series with trends (meters/decade) embedded.

282

3.2. Spatial Distribution of O_3 and its Precursors

284 Tropospheric O_3 results from in-situ photochemical formation and STE. In-situ O_3 results from
285 the photolysis of NO_2. Therefore, the sources and fate of NO_2 in the atmosphere determine O_3
286 burden and distribution. NO_2 is formed from the reaction of hydrogen peroxyl (HO_2) and alkyl
287 peroxyl (RO_2) radicals with NO (R 3.2-1). While photolysis of NO_2 is the main source of ozone,
288 high NO_2 levels can suppress O_3 levels as NO_2 reacts with OH radical forming HNO_3 (R 3.2-2 to
289 R 3.2-4), thus reducing the oxidation rate of hydrocarbons and respectively HO_2 and RO_2 levels,
290 leading to a net loss of O_3 (e.g., Finlayson-Pitts and Pitts, 2000; Elshorbany et al., 2010,
291 Archibald et al., 2020). Ozone production efficiency is calculated as the ratio of the number of
292 NO_2 molecules photolyzed to form O_3 to that lost due to the reaction with OH forming HNO_3.
293 Under NO-sensitive conditions, the decrease in NO_x leads to a reduction in OH, HCHO, and O_3.
294 However, under high NO conditions, a reduction in NO_x could lead to an increase in
295 photochemical products, OH, HCHO, and O_3 because a reduction in NO_2 leads to a decrease in

9

296 OH loss rate, thus higher HO_2 and RO_2 production (Elshorbany et al., 2012; Archibald et al.,
297 2020).

298 R 3.2-1 HO_2/RO_2 +   NO $\rightarrow$ NO_2

299 R 3.2-2 NO_2 + $h\nu$ ($h\nu < 424$ nm) $\rightarrow$ $O(^3P)$ +   NO

300 R 3.2-3 $O(^3P)$ + O_2 +   M $\rightarrow$ O_3 +   M

301 R 3.2-4   OH   + NO_2 (M) $\rightarrow$ HNO_3 (M)
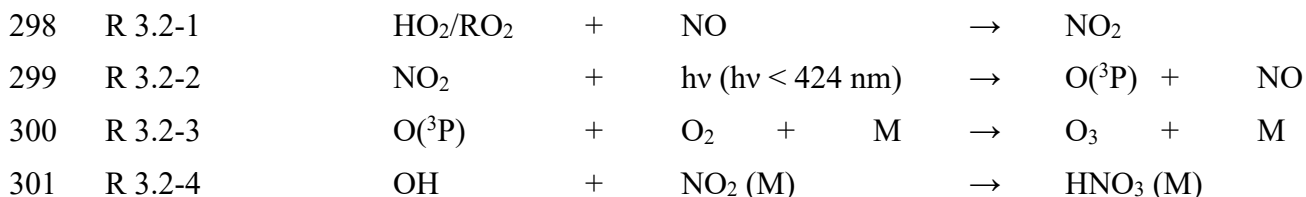
302

303 The observed mean tropospheric columns of O_3, NO_2, and HCHO and atmospheric column of
304 CO from 2005 to 2019 are shown in Figure 4. The unit for column number density is
305 Pmolec/cm^2 ($\times 10^{15}$ molecules per square centimeter), except for TrC-O_3, which is Dobson. NO_2
306 concentration has decreased since 2005 in North America, Europe, and Australia, mainly due to
307 strict measures to reduce air pollution (Lamsal et al., 2015). Since O_3 is a photochemical product
308 that is formed based on non-linear chemistry, a reduction in NO_2 may lead to an increase or
309 decrease in tropospheric O_3 levels based on the dominant photochemical regime in the respective
310 region. In addition, tropospheric ozone levels may be affected by STE especially in the middle
311 and upper troposphere (Li et al., 2024), as well as LRT, especially in the free troposphere (e.g.,
312 Glotfelty et al, 2014; Itahashi et al., 2020). The highest values of the NO_2 tropospheric column
313 are in the northern hemisphere between 10 ºN and 50ºN, especially over the eastern US, northern
314 Europe, and east and south Asia, with elevated levels in the Southern Hemisphere (SH) between
315 10 and 30ºS, especially in sub-Saharan Africa, and Brazil. TrC-O_3 is also highest over the band
316 of 20-50º N, especially over the eastern coast of the US, southern Europe, and east Asia. Some
317 differences exist between TrC-O_3 and TrC-NO_2 spatial patterns which is due to factors including
318 different lifetime, photochemical sensitivity (see sec. 3.4), and STE. On average, the northern
319 hemisphere has higher TC-CO than the southern hemisphere due to a larger number of sources
320 (Buchholz et al., 2021). Additionally, high amounts of CO are found in regions with large
321 anthropogenic sources (e.g., eastern China) or in regions with large and regular fire seasons (e.g.,
322 central Africa) (Buchholz et al., 2021). HCHO and CO show a similar spatial pattern over
323 western Africa due to emissions from biomass burning (Marais et al., 2012, Buchholz et al.,
324 2021). In the following sections, global and regional trends of TrC-O_3 are investigated along
325 with tropospheric ozone precursors.

326
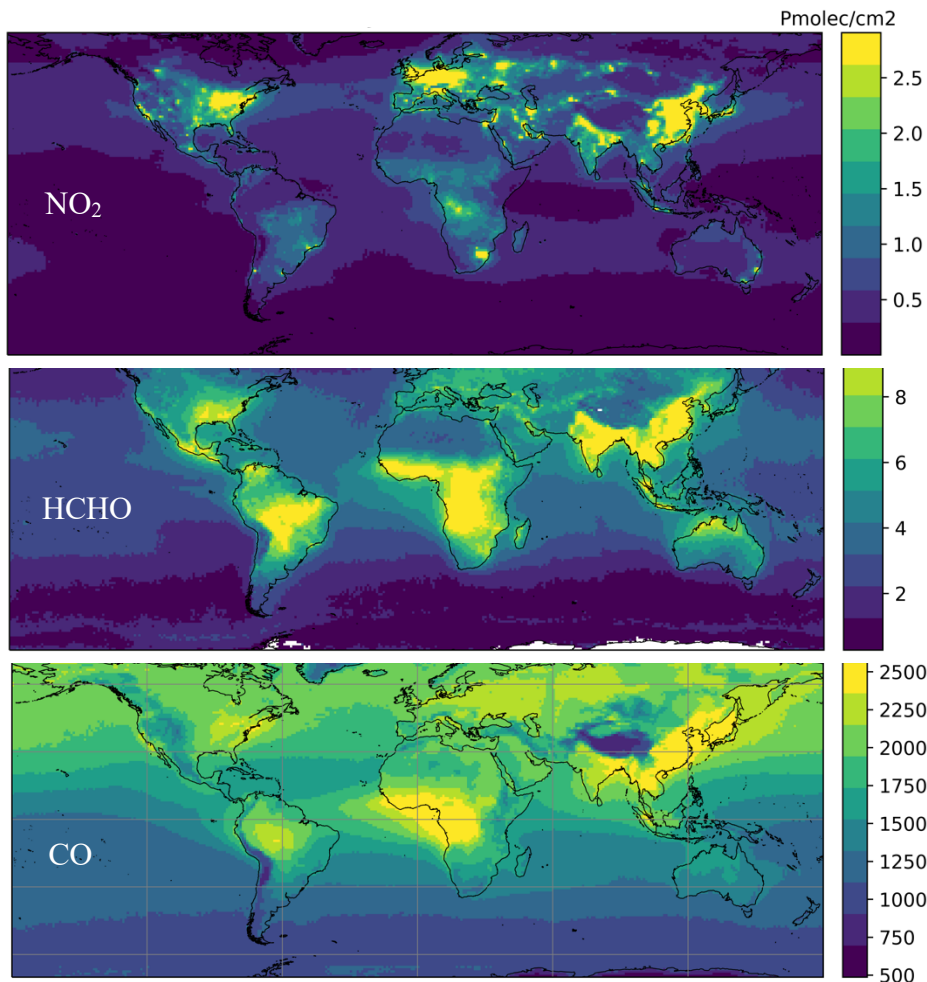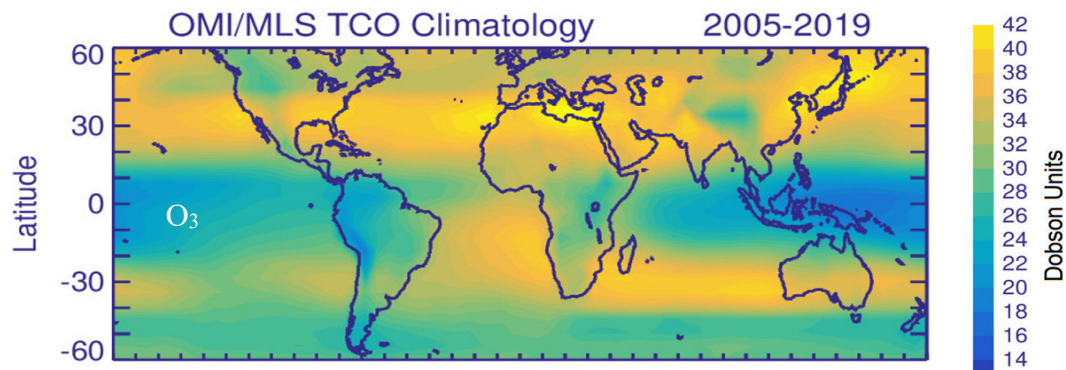
Figure 4: Mean (2005-2019) of TrC-O_3, TrC-NO_2, TrC-HCHO, and TC-CO.

3.3. Simulated O_3 Precursors

Ozone and its precursors differ in their vertical distribution through the troposphere. In this section, we use the GEOS -simulations to show how the lower, middle, and upper troposphere contribute to the simulated columns of O_3 and its precursors to complement the column information from satellites. Figure 5 shows the simulated mean (2005-2019) contributions to tropospheric columns of O_3, NO_2, formaldehyde, and CO, partitioned into the lower (up to 700hPa), middle (700-400hPa), and upper (400hPa to tropopause) portions of the troposphere for the tropical band (30ºS:30ºN) and the global mean. The middle and upper troposphere make

11

large contributions to the simulated TrC-O$_3$ and its variability (Figure 5). The lower troposphere makes the largest contribution to the TrC-HCHO since it is mainly a photochemical product (e.g., Elshorbany et al., 2009), and all three levels make substantial contributions to the CO column. Globally, the relative contributions for TrC-O$_3$, TrC-HCHO and CO are similar to those of the tropics. However, for TrC-NO$_2$ the lower troposphere makes a smaller contribution in the tropics than globally.
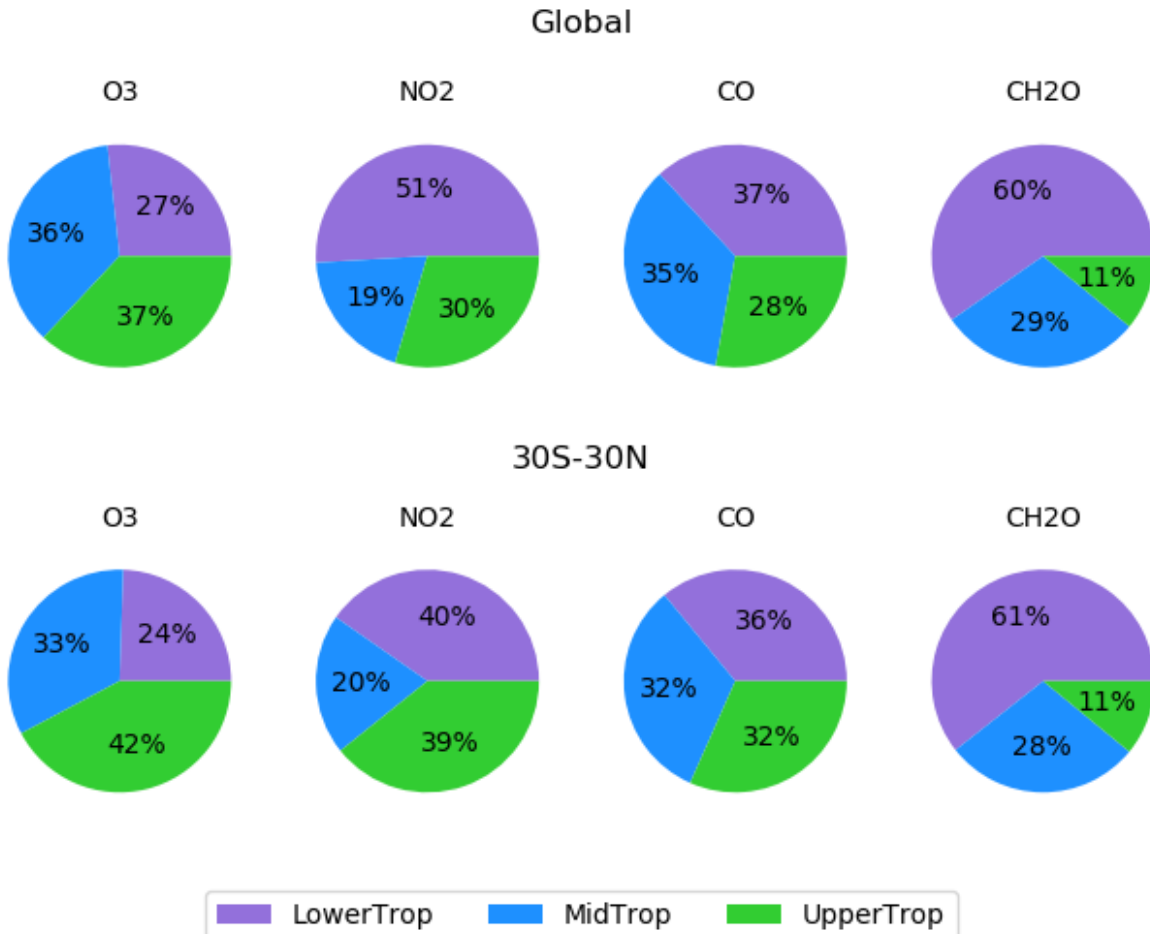
Figure 5: Simulated average (2005-2019) contributions to the tropospheric columns of O$_3$, NO$_2$, formaldehyde, and CO from the lower (surface-700hPa), middle (700-400hPa), and upper troposphere (400hPa-tropopause) using NASA GEOS-GMI. The top row is for the global mean, while the bottom row is averaged from 30°S-30°N.
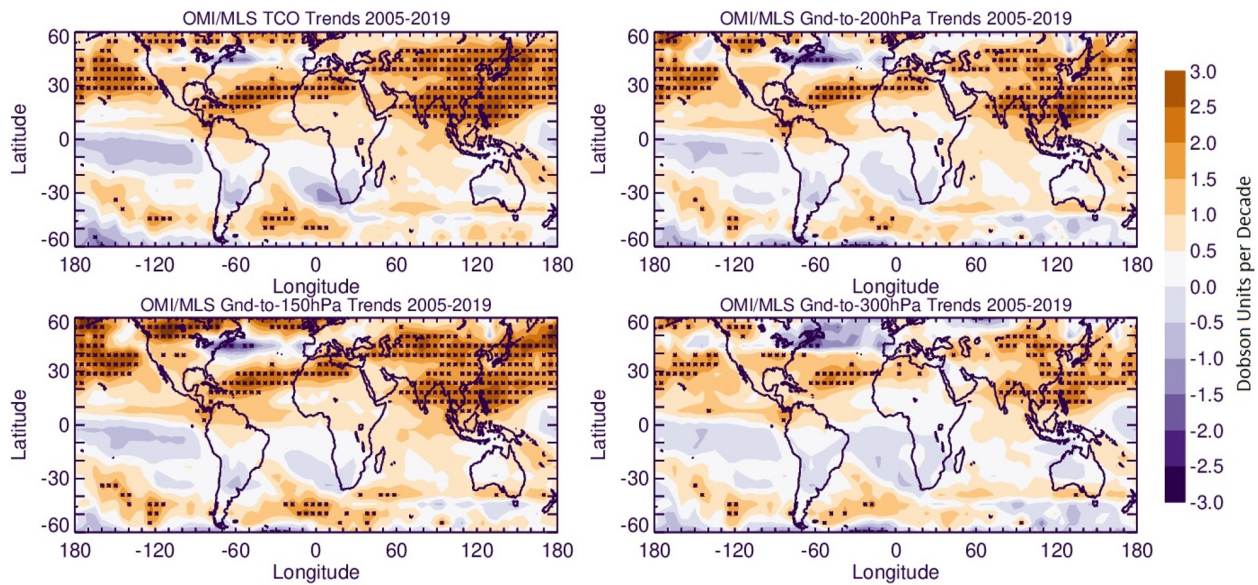
3.4. Tropospheric Trends

3.4.1.   Global Tropospheric Ozone

Global TrC-O$_3$ trends calculated for different column depths are shown in Figure 6. Compared to TrC-O$_3$, OC trends up to 150 hPa seem to be the closest despite OC values being much higher than that of the TrC-O$_3$ (Figure 2). All trends with high confidence, HC (at 95% confidence) are positive indicating increasing trends of ozone columns, regardless of the tropopause height. Low confidence, LC (at 2 σ levels) decreasing TrC-O$_3$ trends were also found in some locations, e.g., South Australia, South Africa, and the northeastern coast of the US. Increasing trends in the

357 northern midlatitudes may also be partially related to STE (Willimas et al, 2019; Li et al., 2024).
358 While the annual trends inform about overall trends, seasonal trends provide insights into local
359 chemistry and meteorology. For example, during the boreal summer months, June, July, and
360 August (JJA), TrC-O_3 HC trends are similar to the annual trends except for HC decreasing trends
361 over South America and South Africa and HC increasing trends over the west and central Africa
362 and Central America (Figure S7). During the boreal winter months, HC trends are also similar to
363 the annual trends (Figure 6) except for HC increasing trends over Europe, North America, South
364 America, and South Africa (Figure S7).

365

366
367 Figure 6: Trends in tropospheric column ozone, based on the WMO thermal definition, and the
368 trends on ozone columns (from ground to 150, 200, and 300 hPa). Trends are calculated based on
369 deseasonalized monthly data from 2005 to 2019. Asterisks denote 95% confidence trends.

370

371 The time series of OMI/MLS TrC-O_3 averaged over several latitudinal bands and at different
372 column depths are shown in Figure 7. Zonal mean TrC-O_3 compares well with partial ozone
373 columns in the tropics (from 30ºS to 30ºN) with the OC of up to 300 hPa differing by about 10
374 DU from the TrC-O_3 (Figure 7b). The lowest TrC-O_3 trends are located in the northern
375 hemisphere (30 – 60ºN) at 0.78±1.16 DU/decade, followed by the southern hemisphere (30-60ºS
376 (0.95±0.75 DU/decade) and the tropical band (30-30ºN (1.06±0.40 DU/decade). In addition, the
377 continental trends over Australia, South Africa, and South America in the 30 ºS -60ºS band are
378 essentially negative and the positive trends in this band are contributed mainly by oceanic
379 regions (see Figure 6). The positive trends in the 30ºN -60ºN band are slightly offset by the
380 negative trends over the northeastern US and western Europe (see Figure 6).

381
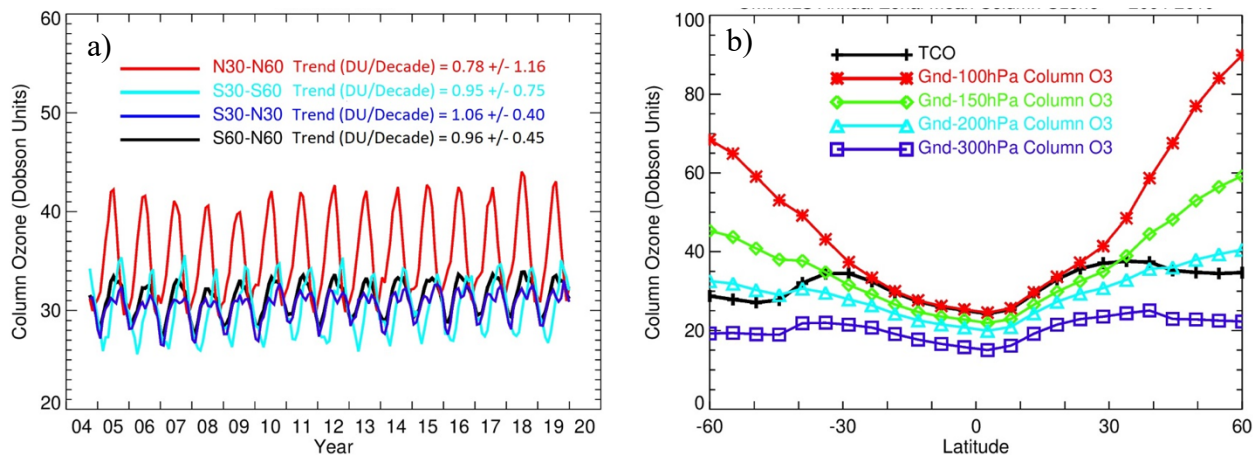
Figure 7: Time series and zonal mean trends of OMI/MLS TrC-O_3 in different latitudinal bands (left) and zonal mean of different column depths (right) from 2005-2019.

Observed trends for the time period before COVID-19 (2005-2019) show that OC trends were highest in the northern latitudes (0-30º N) reaching about 1.5 DU/decade, followed by the northern midlatitudes 30-60ºN (Figure 8). The high trends in the 30-60ºN band are dominated by transpacific impacts as well as some impacts from East Asia. The positive trends in the southern hemisphere (0-30º S) are mainly over Amazonia and Southeast Asia, being offset by small negative trends over Western Australia and South Africa. The trends during the time period (2005-2021) show a decline in O_3 column trends in the northern hemisphere but a slightly increasing trend in the southern hemisphere (Figure 8b). The decreasing trends in the northern hemisphere during the COVID-19 is consistent with previous literature showing a decrease in several pollutants including NO_2 and O_3 due to the extended lockdown periods imposed during the pandemic (e.g., Bauwens et al., 2020; Elshorbany et al., 2021; Steinbrecht et al., 2021; Putero et al., 2023). The decrease of NO_2 in some parts of Europe and the northeastern USA led to a decrease in tropospheric O_3.

Zonal mean trends (Figure 8) show that OC up to 150 hPa is almost identical to that of TrC-O_3 except for the high latitudes 45º-60º S and 45º-60º N. The decreasing trends above 30ºN and 30ºS are due to the offsetting impact of negative trends over the northeastern US and western Europe in the north, and Australia and South Africa in the south, respectively. This impact is less apparent in the 150 hPa OC due to the lower positive trends in that band compared to TrC-O_3. The 200 hPa OC comes next with a very good agreement from 60º S to 10º N. followed by the 100 hPa which is only in good agreement from 30º S to 30ºN, while the 300 hPa OC was the farthest from the TrC-O_3. The decrease of O_3 in the northeastern US and western Europe is consistent with decreasing NO_2 trends and NO-sensitive conditions dominating these regions. The decreasing trends of NO_2 (see below) are due to the successful measures applied since 2004 to mitigate air pollution in these regions. The increase of O_3 in the western US maybe due to LRT from eastern Asia (e.g., Itahashi et al., 2020).

14
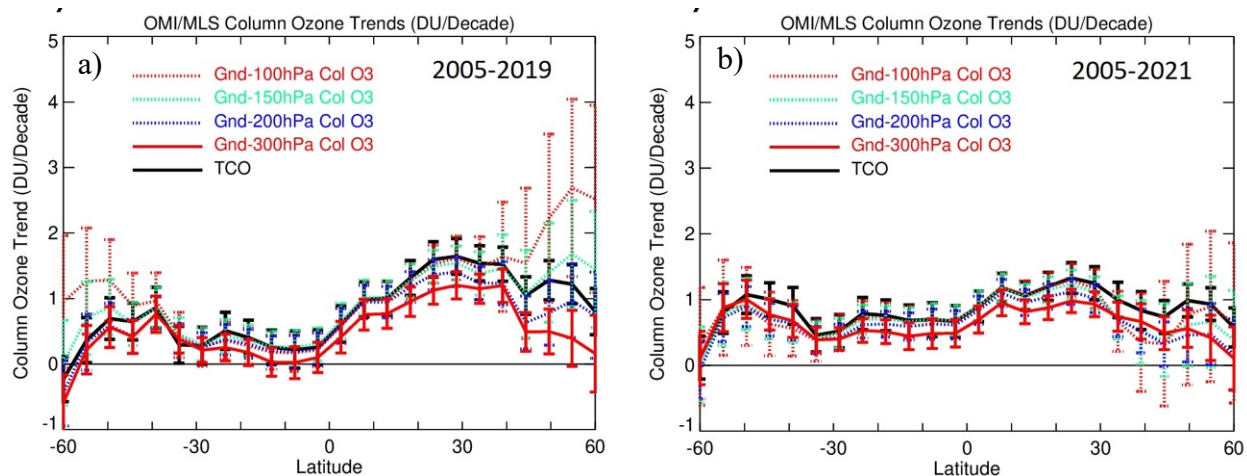
Figure 8: Tropospheric column ozone (TrC-O$_3$) and trends for different column depths before the COVID-19 pandemic (2005-2019) and including the pandemic (2005-2021).
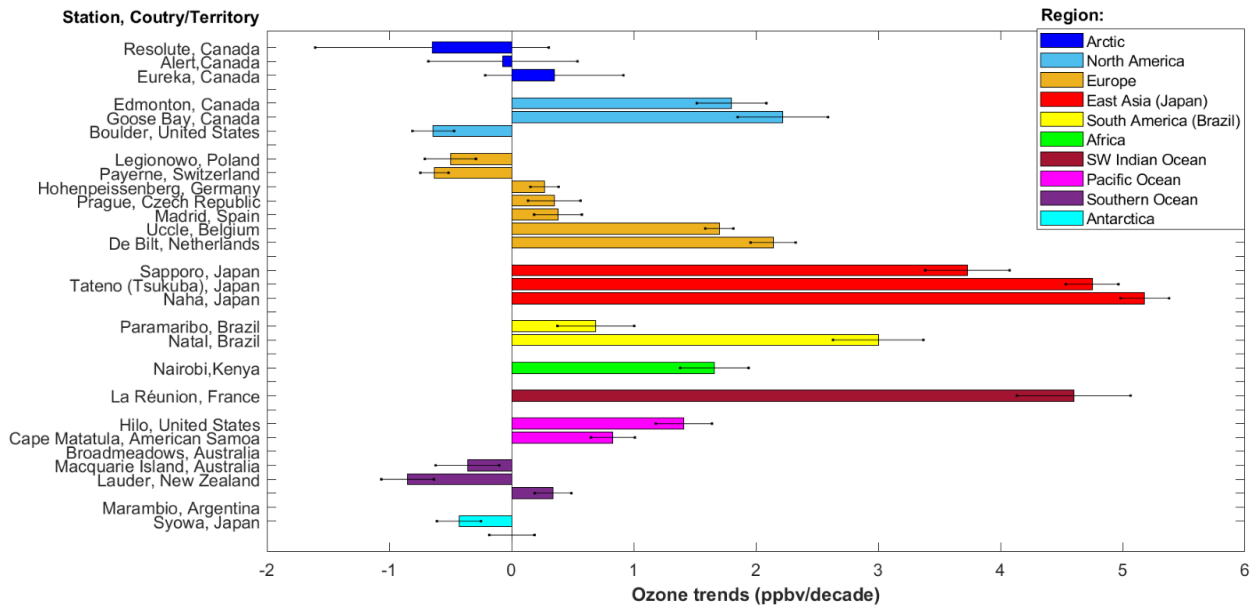
3.4.2.   Free tropospheric trends

Trends of ozone in the free troposphere presented here are based on previous work published in the literature. Despite the high stability of ozonesonde measurements across the global networks over several decades (Stauffer et al., 2022), the spatial sparsity of sounding stations and non-uniform sampling frequency among sites is a limitation in using these data to produce trends. These shortcomings have constrained the ability to include data from many stations in previously published analyses. For example, Chang et. al (2020) estimated that at least 18 profiles per month are needed at a single station to calculate accurate long-term trends, while uncertainty increases at lower sampling rates (Chang et al 2024). However, such high sampling frequency is only achieved at three European stations (Hohenpeissenberg, Germany; Payerne, Switzerland, and Uccle, Belgium), while the rest of the global stations work at lower sampling rates. Nonetheless, high-quality ozonesonde observations continue to be the gold standard against which satellite measurements are validated. Likewise, ozonesonde data continue to provide spaceborne observations with climatological feedback. Thus, recent studies have softened the sampling frequency criteria in order to take advantage of the valuable data set collected by the global ozonesonde networks. For example, the latest trend studies establish the minimum frequency requirement to calculate trends to at least three profiles per month (Wang et al., 2022; Christiansen et al., 2022) with at least eight months of sampling in a year, and at least 15 annual means for an analysis of about two decades (Wang et al., 2022). With these criteria, recent ozonesonde trend analyses indicate that ozone concentration increased globally by 1.8+/-1.3 ppbv/decade in the free troposphere within 800 to 400 hPa (Christiansen et al., 2022). However, there is high regional variability, as illustrated in Figure 9 where ozone trends published by Wang et. al. (2022) (1995-2017 data between 950-250 hPa) are organized by regions and stations. For example, ozone in East Asia (Japan) has been increasing at a rate of 3.5 to 5 ppbv/decade, particularly since 2010 (Christiansen et al., 2022), which may lead to transpacific LRT of O$_3$ to the western US (e.g., Itahashi et al., 2020). Over the Southwestern Indian Ocean (La Réunion), trends are of similar magnitude (>4.5 ppbv/decade). In tropical South America, over the Atlantic basin region (Paramaribo and Natal), sounding measurements also show ozone increases by almost 3 ppbv/decade (Natal), but other regions in South America continue to lack sufficient measurements to produce trends. At tropical stations in Africa (Nairobi) and the

Pacific Ocean (Hilo and American Samoa) trends are also positive, although of lower magnitudes (0.83-1.7 ppbv/decade). In contrast, polar stations both at the Arctic and Antarctica as well as the Southern Ocean show overall decreasing ozone concentrations to low-confidence trends. Exceptions are the Eureka station in Canada and Lauder station in New Zealand, which both show slight ozone increases (less than 0.5 ppbv/decade). The direction of regional trends by Wang et. al. (2022) is consistent with regional trends presented in similar independent research (Christiansen et al., 2022). As atmospheric composition continues to become modified under the current regime of climate change, building consistent and longer time series of ozonesonde measurements at other regions will continue to be an important source of firsthand information to assess tropospheric ozone changes and trends.

Figure 9: Ozone trends in the free troposphere from ozonesonde measurements calculated by Wang et. Al. (2022) and organized by region and station. Data covers the 1995-2017 period within 950 to 250 hPa. Error bars show 1-σ uncertainty. The coordinates of ozonesonde stations are listed in Table S1.

3.4.3.   Regional Ozone Trends

As shown in Figure 10, the highest OMI/MLS regional trend is observed over East Asia (2.16±1.27 DU/decade) while the lowest trend is calculated over Eastern USA (0.63±1.72) followed by Western Europe (0.89±1.60) and Australia (1.05±1.44) DU/decade. We next calculate the monthly trends from the GEOS-GMI simulation to investigate how the simulated trends vary through the tropospheric column.

16
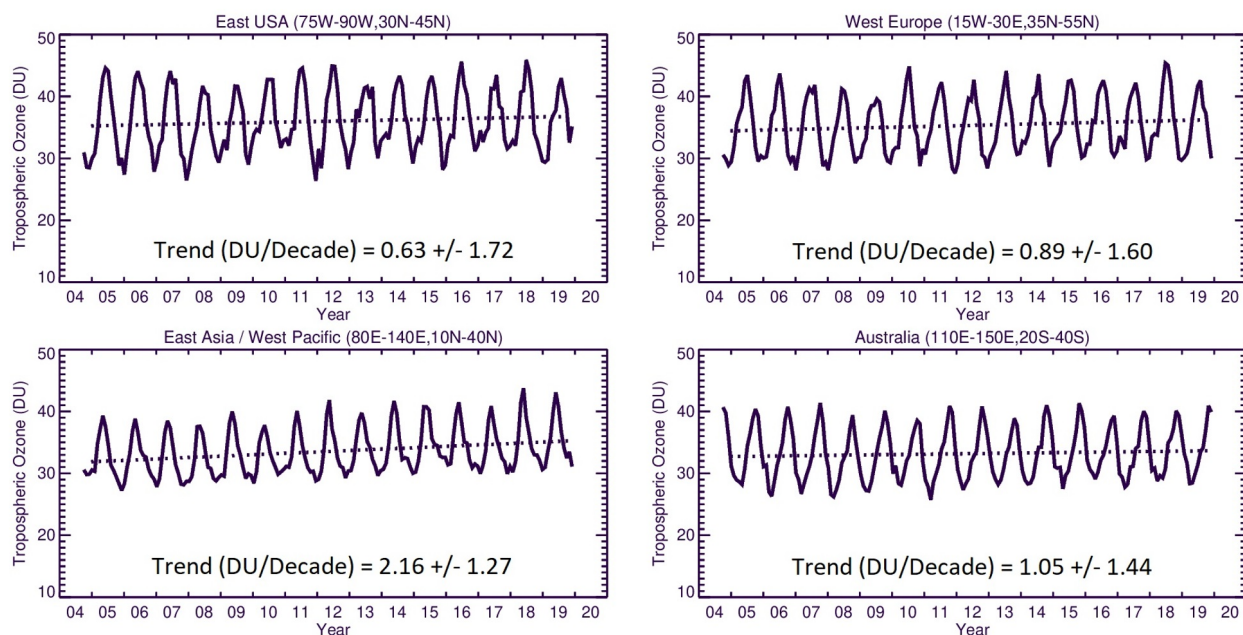
Figure 10: OMI/MLS observed regional mean trends of TrC-O$_3$.

The simulated trends in partial columns (lower, middle, and upper troposphere), as well as the TrC-O$_3$, TrC-NO$_2$, TrC-HCHO, and TC-CO from 2005 to 2019, are shown in Figure 11. The simulated tropospheric columns of TrC-O$_3$ and TrC-HCHO show a positive trend in most regions (Figure 11), consistent with the results of Liu et al (2022) using a different GEOSCCM simulation. Liu et al (2022) highlighted the importance of formaldehyde trends for analyzing the simulated trends in tropospheric ozone. Considering different latitude bands, the highest trends are simulated between 30º S and 60º N, consistent with calculated trends based on satellite observations (see sec. 3.4). In contrast, the simulated NO$_2$ and CO trends are mostly negative, although positive trends are simulated over East Asia. The largest NO$_2$ negative trends are in the northern hemisphere between 30ºN and 60ºN. The decrease in NO$_2$ trends is consistent with the successful measures to curb emissions of pollution criteria in the US and Europe. The increased trends in TrC-O$_3$ but decreased trends in TrC-NO$_2$, and TC-CO might indicate STE contribution (Trickl et al., 2020; Li et al., 2024) in addition to the local chemistry.
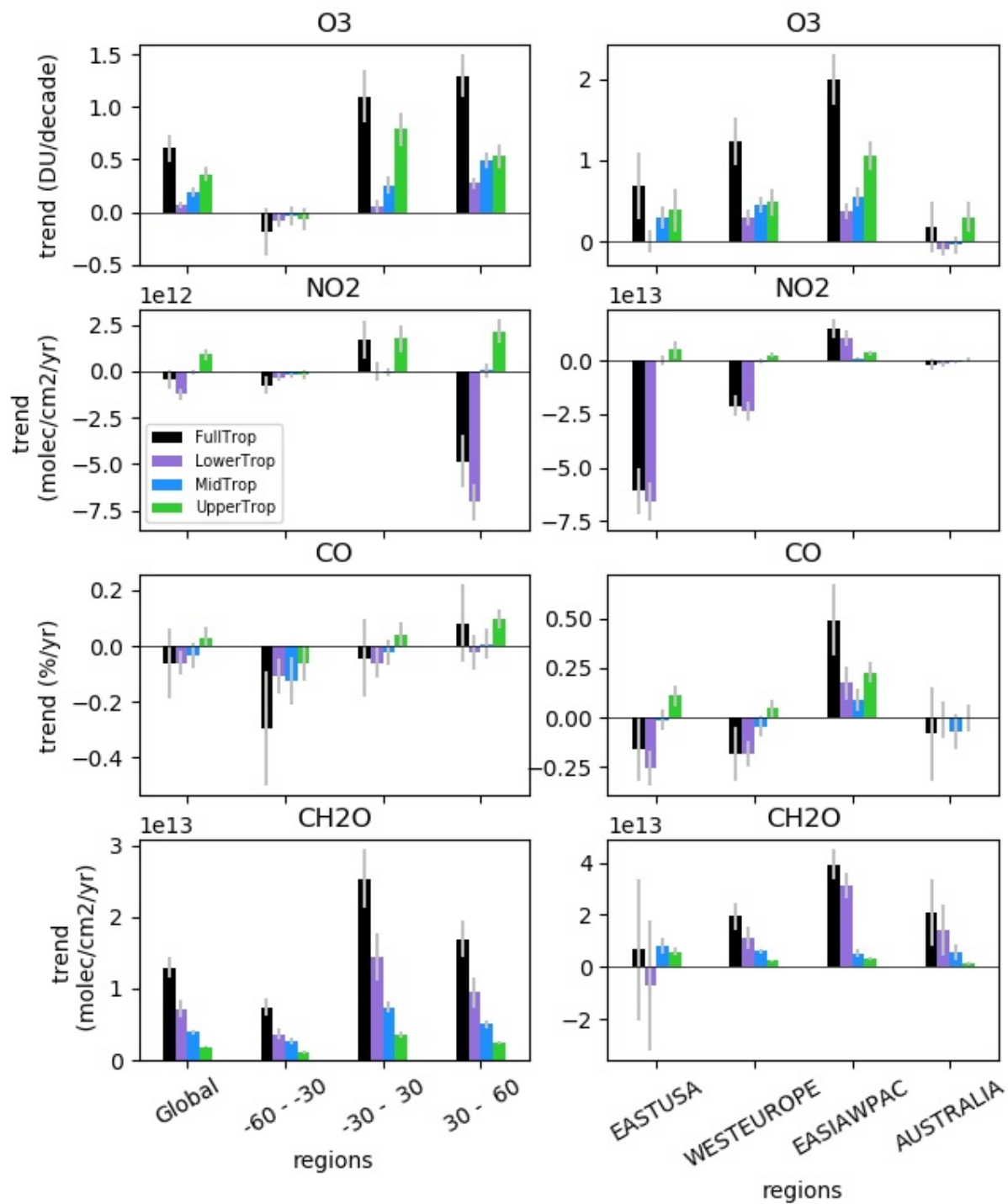
Figure 11: Global and regional trends in O_3, NO_2, CO, and HCHO calculated from the GEOS-GMI simulation for the tropospheric column (black), lower troposphere (purple), middle troposphere (blue), and upper troposphere (green) from 2005 to 2019. The lower, middle, and upper troposphere are defined as in Figure 5.

The GEOS-GMI simulation provides an estimate of the relative contribution from different portions of the tropospheric column to the column trends and shows that this contribution varies by region and constituent. The middle and upper troposphere make the largest contributions to

495 the simulated TrC-O₃ trend globally, with large contributions from the upper troposphere driving
496 the simulated TrC-O₃ trend at 30°S-30°N (Figure 11). The middle and upper troposphere
497 contribute most of the simulated positive TrC-O₃ trend over the eastern USA, while all three
498 levels contribute over western Europe and East Asia. The upper troposphere makes the primary
499 contribution to the simulated trend over Australia. Simulated TrC-O₃ trends are also quite
500 comparable to those observed by OMI/MLS within the measurement model uncertainty (see
501 Figure 10 and Figure 7). Over Australia, the OMI/MLS trend of 1.05±1.44 DU/decade is higher
502 than the model trend of about 0.18±0.308 DU/decade (see Figure 11). However, since OMI/MLS
503 trend has a calculated uncertainty (2σ) of 1.44 DU/decade, both the model and OMI/MLS for
504 Australia are not statistically different.

505 While the upper troposphere is a major driver of the simulated TrC-O₃ trends, the lower
506 troposphere is the largest contributor to the simulated trends in the tropospheric NO₂, CO, and
507 HCHO globally and over many regions (Figure 11). Exceptions include the simulated NO₂ in the
508 tropics (30°S-30°N), which is dominated by the upper troposphere, the simulated HCHO column
509 over the eastern USA, which is driven by the middle and upper troposphere; an important role
510 for upper tropospheric CO over East Asia; and the CO trend over Australia driven by the middle
511 tropospheric contribution. Figure 11 also shows that in some regions, such as the eastern USA
512 for all 3 precursors, the upper and lower tropospheric trends counteract each other, reducing the
513 magnitude of the column trend. In the following sections, we investigate trends and variability in
514 O₃ precursors, NO₂, CO, and HCHO.

3.4.4. NO₂ Trends

516 The TrC-NO₂ trends over 2005-2019 are shown in Figure 12 with a regional summary in Figure
517 13. On a global scale, there is a strong spatial variability of the TrC-NO₂ trends. About a third of
518 the oceans show HC increase of TrC-NO₂ trends (at 95% confidence level), especially at mid-
519 latitude, with trends up to +0.01 Pmolec/cm²/yr while only a few cells in the equatorial Pacific
520 show an HC decrease.

521

Annual trend of OMI TrC-NO2
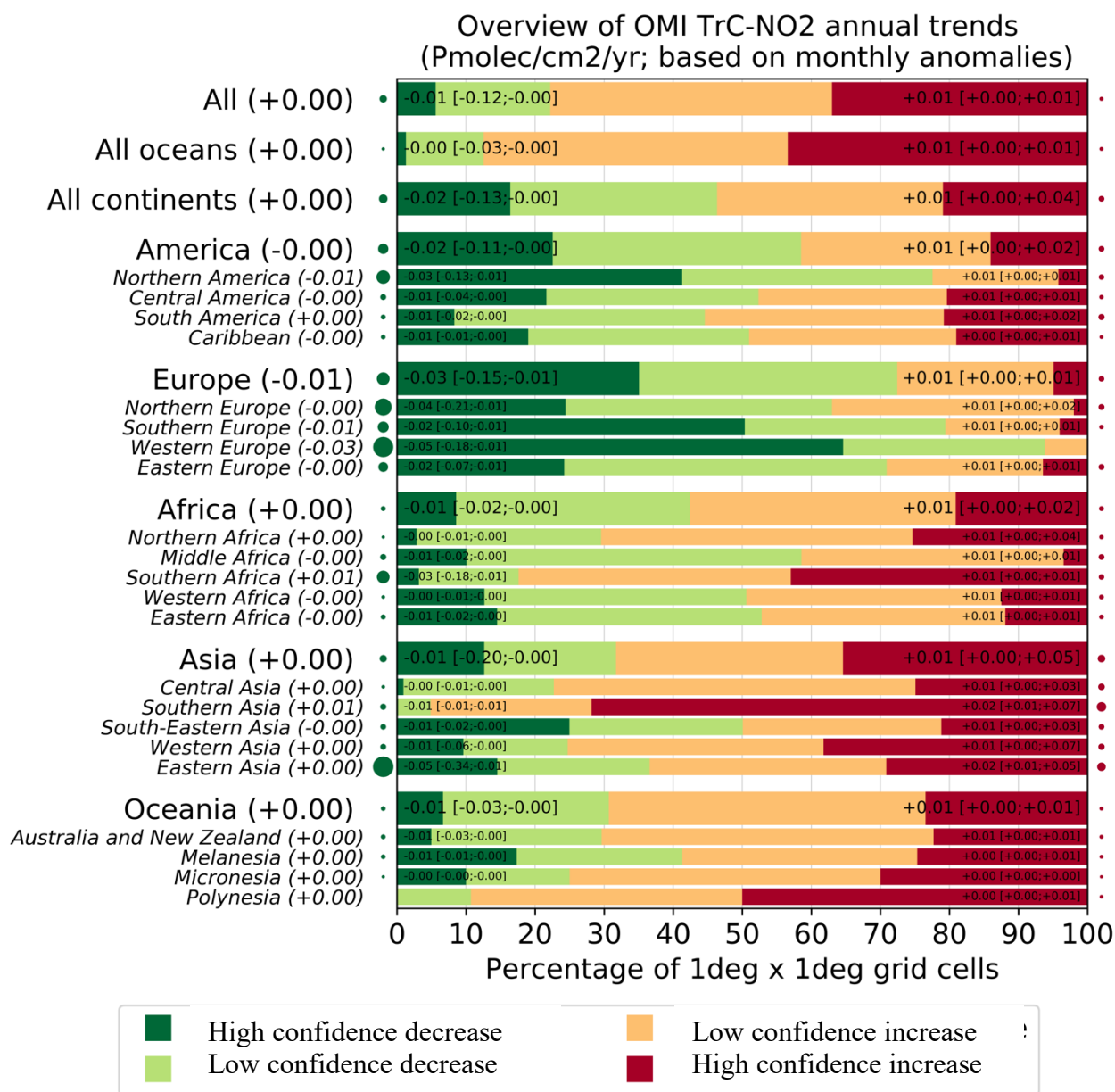(based on monthly anomalies)
(Jan-Dec)
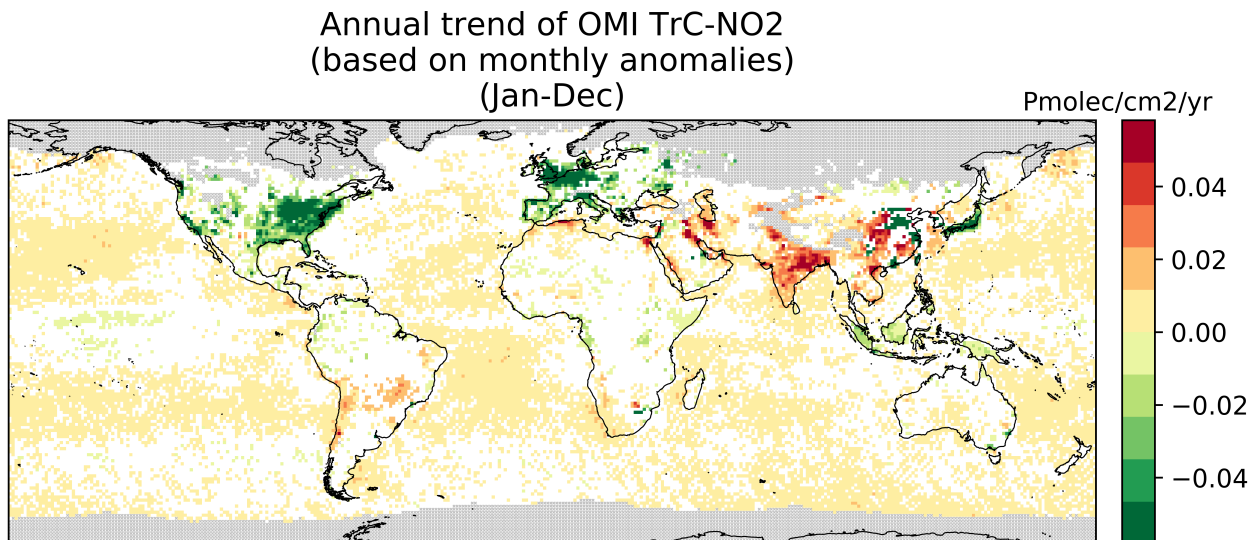
523 Figure 12: Global trends of OMI NO₂ tropospheric column (TrC-NO₂) over 2005-2019 (see text
524 for details on the calculation of the trends). Grey areas correspond to areas without enough data,
525 white areas correspond to regions where the trends remain at low confidence (at a 95%
526 confidence level).

527   Regional trends are shown in Figure 13. For high-confidence trends in a given region, the
528   numbers correspond to the percentiles 5/50/95 of trends among the different cells of the region
529   where trends are considered high-confidence. Each region is tagged with a circle whose size is
530   proportional to the p50 of the high-confidence trends (red for positive and green for negative),
531   which allows us to quickly see regions where the trend is strong. For instance, for Eastern Asia
532   (this region includes 1442 $1°\times1°$ grid cells) about 15% of the grid cells (about 216 grid cells) in
533   this region show a high-confidence decrease in TrC-NO_2. Over these specific 216 cells with a
534   high-confidence decrease of TrC-NO_2, the 5th and 95th percentile of the trend is -0.34 and -0.01,
535   respectively, Pmolec/cm^2/yr. About 28% of the grid cells in this region show a high-confidence
536   increase of TrC-NO_2 (which means about 403 grid cells). Over these specific 403 cells with a
537   high-confidence increase of TrC-NO_2, the 5th (resp 95th) percentile of the trend is +0.01 (resp
538   0.05) Pmolec/cm^2/yr. Therefore, the Eastern Asia region shows sub-regions with high-
539   confidence decreasing TrC-NO_2, others with high-confidence increasing TrC-NO_2, and the rest
540   with low-confidence (positive and negative) trends. This figure allows us to quickly understand
541   the distribution of the trends within a given region while the overall regional trend is given by
542   the 50th percentile and the circles tagging each region. It's a regional summary of what is shown
543   in the trend global map. In Eastern Asia, the area where trends are with high-confidence positive
544   is more extended than for the high-confidence decrease (28% versus 15%), but the trend values
545   tend to be smaller (at least when comparing the 50th percentiles, -0.05 versus +0.01
546   Pmolec/cm^2/yr). The map of regions is included in the supplement. Canada is included in
547   northern America but as shown in the trend map, most of Canada does not have OMI data

548   Over continental areas, high-confidence positive and negative trends are found in about
549   15-20% of the grid cells each (Figure 12). Regions with predominantly decreasing TrC-NO_2
550   include western and southern Europe (where about 50-60% of cells with a high-confidence
551   decrease), northern America (40% of cells with a high-confidence decrease, mostly located in the
552   eastern United States), Japan, and Indonesia. In absolute terms, these negative trends reach
553   values of about -0.03 Pmolec/cm^2/yr. Specific eastern regions of China also show similar high-
554   confidence TrC-NO_2 decreases but overall, a larger part of the country faces increasing trends up
555   to +0.03 Pmolec/cm^2/yr. Similar positive trends are observed over most of India, as well as in
556   specific parts of south-eastern Asia (mainly Vietnam) and the Middle East (mainly Iran and
557   Iraq). Conversely, TrC-NO_2 trends in Africa and South America remain mainly low-confidence ,
558   except in a few specific regions with high-confidence increases (e.g. South Africa, Morocco,
559   Chile, and parts of Brazil).

560   The trends in NO_2 have varying effects on the tropospheric ozone column, which is
561   related to the different local chemistry in each region. The concomitant decrease in TrC-O_3 and
562   TrC-NO_2 trends over some parts of the eastern US, and western Europe is consistent with the
563   strict NO_x control measures that were applied over the last two decades. STE can also contribute
564   to increased TrC-O_3 trends, especially in the mid-latitudes. A decreasing trend of TrC-NO_2 but
565   an increasing trend of TrC-O_3 is present in some other regions such as in the central US, which
566   might be due to local chemistry and STE.

567

20

Overview of OMI TrC-NO2 annual trends (Pmolec/cm2/yr; based on monthly anomalies)

Region	High confidence decrease value	High confidence increase value
All (+0.00)	-0.01 [-0.12;-0.00]	+0.01 [+0.00;+0.01]
All oceans (+0.00)	-0.00 [-0.03;-0.00]	+0.01 [+0.00;+0.01]
All continents (+0.00)	-0.02 [-0.13;-0.00]	+0.01 [+0.00;+0.04]
America (-0.00)	-0.02 [-0.11;-0.00]	+0.01 [+0.00;+0.02]
Northern America (-0.01)	-0.03 [-0.13;-0.01]	+0.01 [+0.00;+0.01]
Central America (-0.00)	-0.01 [-0.04;-0.00]	+0.01 [+0.00;+0.01]
South America (+0.00)	-0.01 [-0.02;-0.00]	+0.01 [+0.00;+0.02]
Caribbean (-0.00)	-0.01 [-0.01;-0.00]	+0.00 [+0.00;+0.01]
Europe (-0.01)	-0.03 [-0.15;-0.01]	+0.01 [+0.00;+0.01]
Northern Europe (-0.00)	-0.04 [-0.21;-0.01]	+0.01 [+0.00;+0.02]
Southern Europe (-0.01)	-0.02 [-0.10;-0.01]	+0.01 [+0.00;+0.01]
Western Europe (-0.03)	-0.05 [-0.18;-0.01]	
Eastern Europe (-0.00)	-0.02 [-0.07;-0.01]	+0.01 [+0.00;+0.01]
Africa (+0.00)	-0.01 [-0.02;-0.00]	+0.01 [+0.00;+0.02]
Northern Africa (+0.00)	-0.00 [-0.01;-0.00]	+0.01 [+0.00;+0.04]
Middle Africa (-0.00)	-0.01 [-0.02;-0.00]	+0.01 [+0.00;+0.01]
Southern Africa (+0.01)	-0.03 [-0.18;-0.01]	+0.01 [+0.00;+0.01]
Western Africa (-0.00)	-0.00 [-0.01;-0.00]	+0.01 [+0.00;+0.01]
Eastern Africa (-0.00)	-0.01 [-0.02;-0.00]	+0.01 [+0.00;+0.01]
Asia (+0.00)	-0.01 [-0.20;-0.00]	+0.01 [+0.00;+0.05]
Central Asia (+0.00)	-0.00 [-0.01;-0.00]	+0.01 [+0.00;+0.03]
Southern Asia (+0.01)	-0.01 [-0.01;-0.01]	+0.02 [+0.01;+0.07]
South-Eastern Asia (-0.00)	-0.01 [-0.02;-0.00]	+0.01 [+0.00;+0.03]
Western Asia (+0.00)	-0.01 [-0.06;-0.00]	+0.01 [+0.00;+0.07]
Eastern Asia (+0.00)	-0.05 [-0.34;-0.01]	+0.02 [+0.01;+0.05]
Oceania (+0.00)	-0.01 [-0.03;-0.00]	+0.01 [+0.00;+0.01]
Australia and New Zealand (+0.00)	-0.01 [-0.03;-0.00]	+0.01 [+0.00;+0.01]
Melanesia (+0.00)	-0.01 [-0.01;-0.00]	+0.00 [+0.00;+0.01]
Micronesia (+0.00)	-0.00 [-0.00;-0.00]	+0.00 [+0.00;+0.00]
Polynesia (+0.00)		+0.00 [+0.00;+0.01]

Percentage of 1deg x 1deg grid cells (x-axis: 0 10 20 30 40 50 60 70 80 90 100)

Legend:
- High confidence decrease
- Low confidence decrease
- Low confidence increase
- High confidence increase

Figure 13: Summary of the high-and low-confidence regional trends of OMI NO$_2$ tropospheric column (TrC-NO$_2$) trends over 2005-2019, at a 95% confidence level (see text for details on the calculation of the trends). For each region, the trend on the bars is in the format: p50 [p5; p95], which represents the 50th[5th, and 95th] percentiles of the trends.

Figure 14 shows the time series of regional mean tropospheric NO$_2$ concentrations from three satellite instruments, OMI for 2005-2020, GOME-2 for 2007-2018, and SCIAMACHY for 2005-2012. All the instruments exhibit common large seasonal and year-to-year variations over both industrial regions and biomass-burning areas. Slight systematic differences among the instruments can mainly be attributed to the different overpass times. The satellite observations show positive trends over China by 2010, followed by a continued decrease. Over the USA and Europe, all the retrievals show a downward trend over the analysis period. Over the US, the observed TrC-NO$_2$ levels decreased rapidly during 2005–2009 and subsequently show weaker reductions, as

582   discussed by Jiang et al. (2018). A similar slowdown trend is found in Europe. Over India, the
583   OMI observations show positive trends over the 14 years (+1.6 % yr^{-1}). The seasonal and year-to-
584   year variations over Southeast Asia and northern and central Africa are associated with changes in
585   biomass-burning activity (Ghude et al., 2009).

586
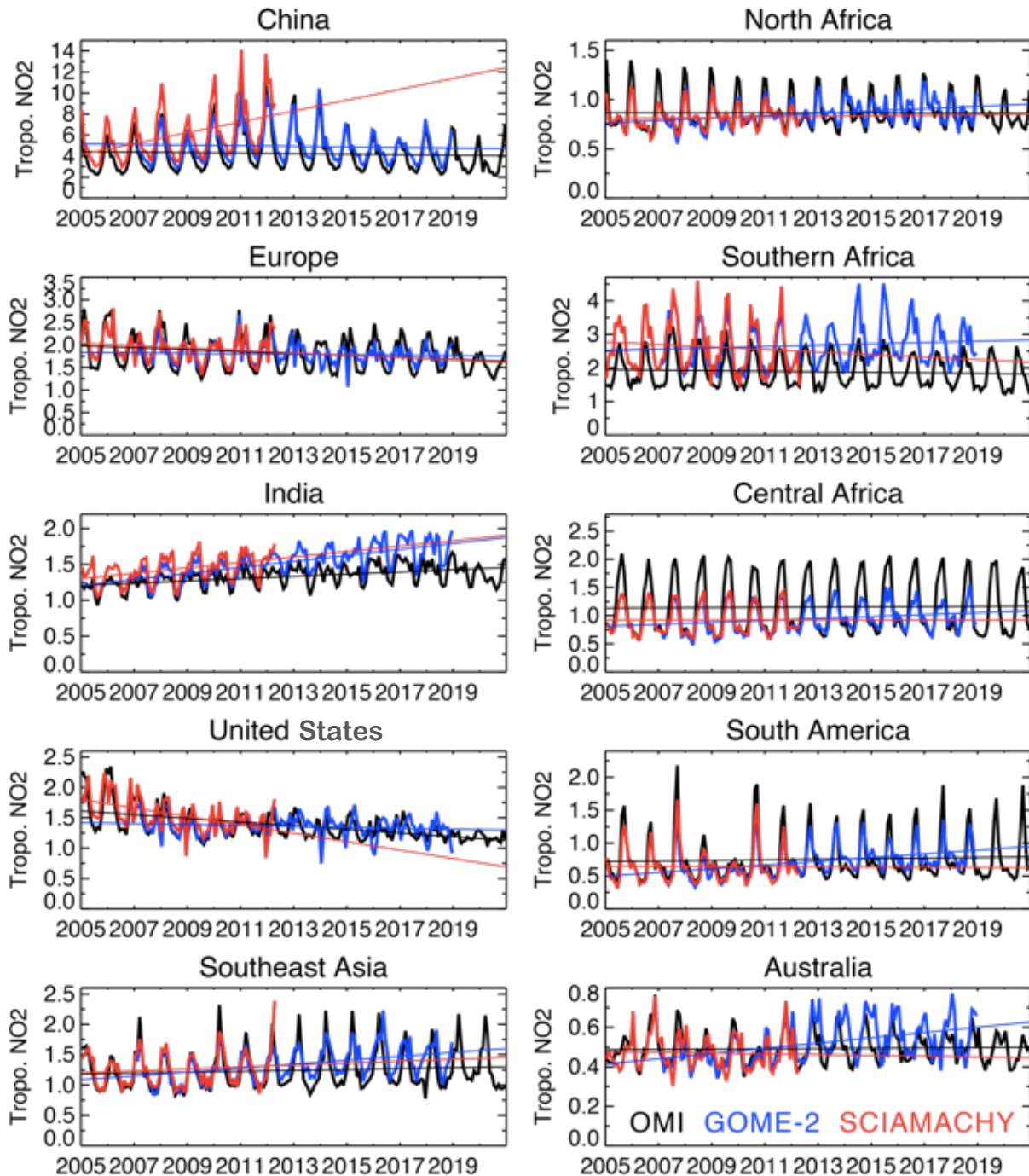
587

588   Figure 14: Time series of regional monthly mean tropospheric NO_2 columns (in 10^{15} molecules
589   cm^{-2}) averaged over China (110–123° E, 30–40° N), Europe (10° W–30° E, 35–60° N), the US
590   (70–125° W, 28–50° N), India (68–89° E, 8–33° N), South America (50–70° W, 20° S–Equator),
591   northern Africa (20° W–40° E, Equator–20° N), central Africa (10–40° E, Equator–20° S),

592   southern Africa (25–34° E, 22–31° S), southeastern Asia (96–105° E, 10–20° N), and Australia
593   (113–155° E, 11–44° S) obtained from OMI (black), GOME-2 (blue), and SCIAMACHY (red).

594   **3.4.5.   CO Trends**

595   CO trends are calculated based on MOPITT v9 products, see sec. 2.2.1. Observed CO trends
596   below show a slowing in the trend compared to a previous analysis (Buchholz et al. (2021). In
597   the northern hemisphere, CO trends are largely negative over the US and Europe, which is
598   consistent with improvements in combustion efficiency and policies implemented to reduce air
599   pollution since 2004. Except for small sporadic positive trends, no HC trends can be calculated
600   over Central Asia (India and China), while there is a strong negative trend in East China due to
601   the recent strong focus on air quality improvement, and no HC trend in the SH.

Annual trend of MOPITT TC-CO
(based on monthly anomalies)
(Jan-Dec)
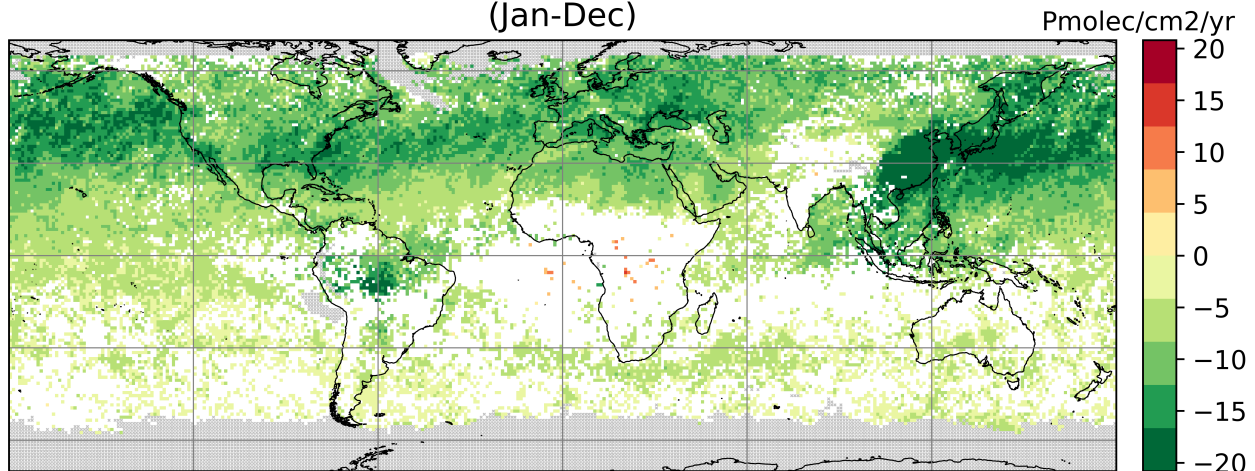
602

603   Figure 15: Trends in TC-CO from MOPITT V9J data, 2005-2019 (see text for details on the
604   calculation of the trends). Grey areas correspond to areas without enough data, white areas
605   correspond to regions where the trends remain statistically low-confidence at a 95% confidence
606   level.

607

608   A regional summary of the trends in the global map is shown in Figure 16. CO trends are
609   predominantly negative everywhere except for some sporadic positive trends over middle Africa.
610   Decreasing TC-CO trends are highest in Europe, followed by Asia and America with about 86%,
611   75%, and 69% of their cells being negative, respectively. The 50 percentiles of the trends in
612   these cells are -12.01, -10.21, and -10.16 Pmolec/cm^2/yr, respectively. Africa shows the lowest
613   decreasing trends as the negative trends in North Africa are being offset by small increasing
614   trends in middle Africa. Overall, about 41% of the cells in Africa show decreasing trends, and
615   50% of the trends in these cells account for -8.71 Pmolec/cm^2/yr. Thus, even though the NH
616   accounts for most of CO emissions, decreasing trends of TC-CO are evident in these regions.

617
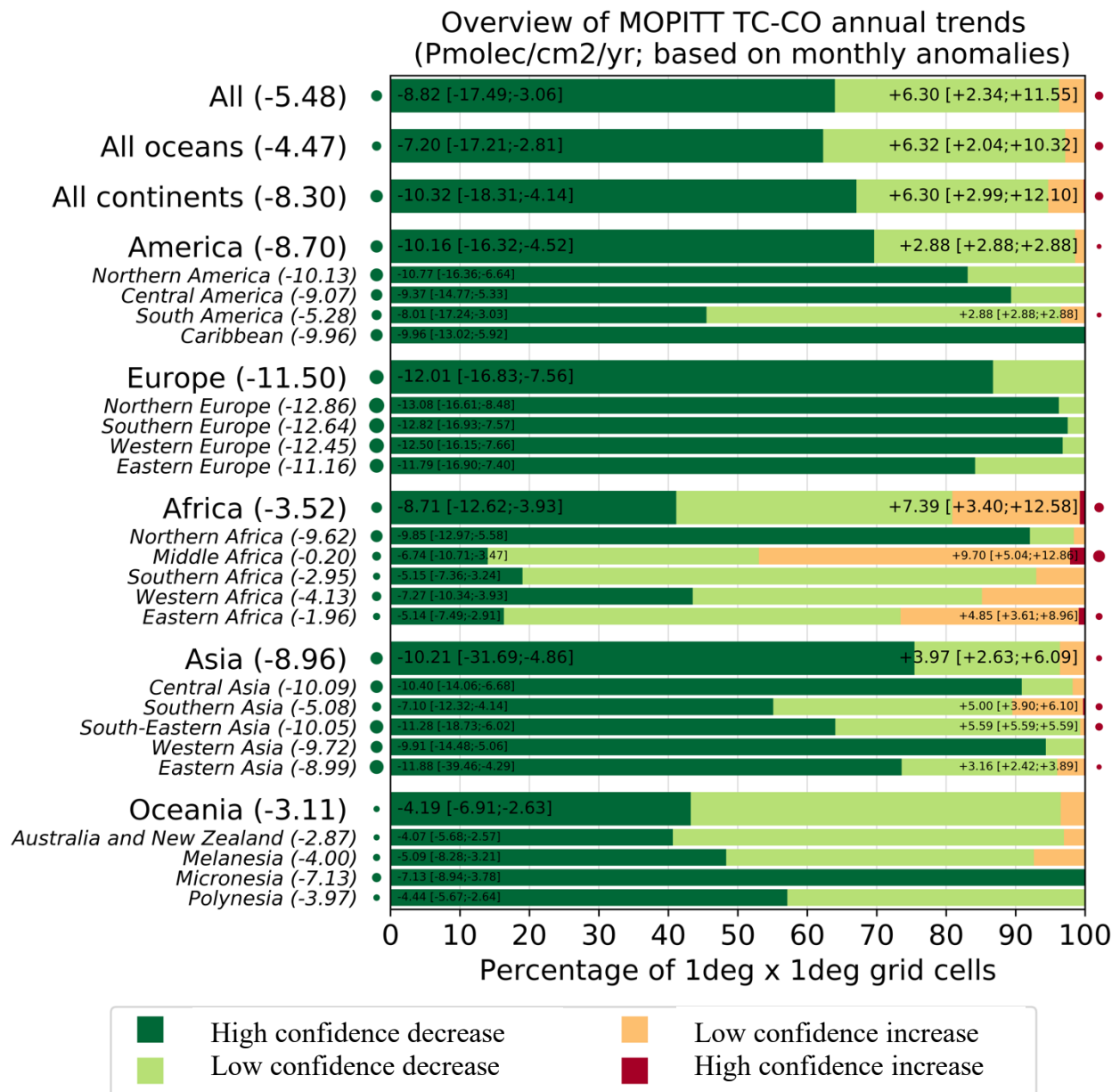
Figure 16: Summary of the statistically high- and low-confidence regional trends of MOPITT TC-CO trends over 2005-2019, at a 95% confidence level (see text for details on the calculation of the trends). For each region, the trends reported on the left (resp. right) represent the 50th[5th, and 95th] percentiles of the trends calculated over the different grid cells showing a high-confidence TC-CO increase or decrease.

Shown below are also the trends in the MOPITT column average volume mixing ratio (VMR) anomalies from 2005 to 2019 (Figure 17) using QR as well as Weighted least squares (WLS)) as Buchholz et al. (2021). The region boundaries are the same as used in Fig. 10 and 11. Results show a HC decreasing trend in the NH (-0.35 ±0.1% annually), a smaller decreasing trend in the Mid-latitudes (-0.26 ±0.1% annually), and LC trend in the SH (-0.14 ±0.1% annually). The three anthropogenic regions investigated in the NH all show strong decreases in CO. The larger negative trend over Australia (-0.2 ±0.1% annually) than the average SH, suggests sources from

632 the other two land regions (Southern Africa and South America) may be counteracting negative
633 trends in CO for the SH.

634
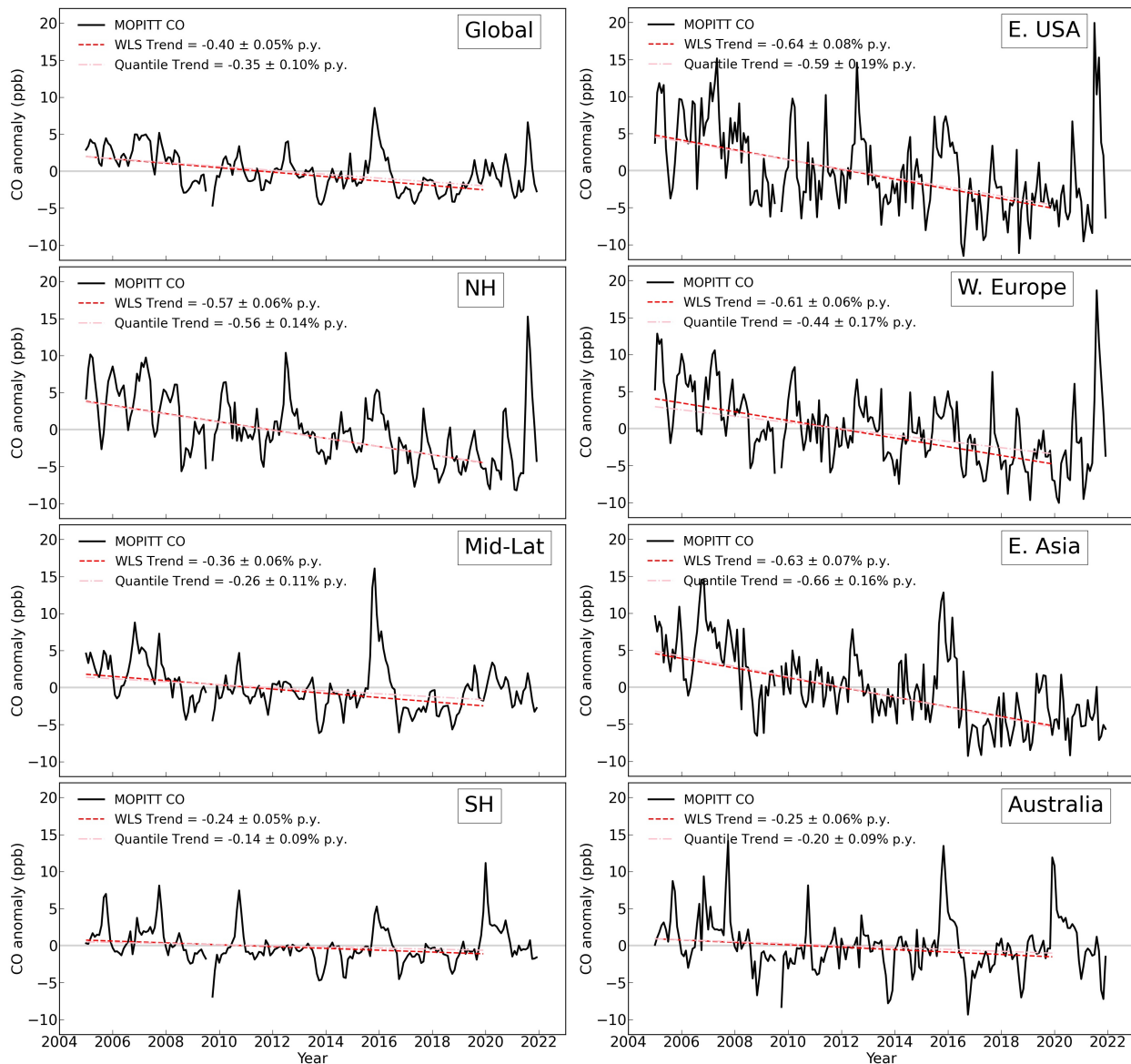
635

636 Figure 17: MOPITT monthly average CO anomalies in column average volume mixing ratio
637 (VMR, ppb), 2005-2021 (black). Updated dataset based on Buchholz et al. (2021). Data is Level
638 3, monthly average daytime observations, using version 9 joint NIR/TIR retrievals (V9J).
639 Regions are defined in Figure 10 and Figure 11. Trends are calculated on anomalies 2005-2019.
640 The weighted Least Squares trend (red) is weighted by the monthly regional standard deviation.
641 The quantile regression trend is also shown (pink). Grey dashed lines indicate a zero trend.

642

643 We also compare CO trends with Community Earth System Model (CESM) simulations
644 (Supplement Fig S1). While the magnitude of modeled CO tends to be underestimated relative to
645 observations, the anomalies between the model and measurements are comparable, indicating the
646 model reproduces interannual variability well. The negative trends in the NH are also reproduced

25

647 by CESM, although to a smaller degree than observations, suggesting that the trends in sources
648 or loss processes (such as OH oxidation) are underestimated in the model. These processes will
649 impact the feedback into modeled ozone and the resulting interpretation of driving factors for
650 ozone abundance and variability. Interestingly, CESM correctly represents a negative trend in
651 CO for the NH and East Asia while GEOS-GMI has a positive CO trend in those regions (Fig.
652 11), likely due to the well-known misrepresentation of East Asia air quality improvements in
653 emission inventories (Yin et al, 2015; Strode et al., 2016; Zheng et al, 2019). In the SH, CESM
654 does not predict HC trends.

655

656 ### 3.4.6. HCHO Trends

657 HCHO, mainly a photochemical product results from hydrocarbon oxidation. HCHO is itself a
658 source of OH and ozone through its photolysis producing HO_2, which can be recycled back to
659 OH if sufficient NO levels are present.

660 R 3.4-1 $HCHO$ + $h\nu$ ($\lambda < 325$ nm) $\rightarrow$ H   +   HCO

661 R 3.4-2   H   + O_2 +   M $\rightarrow$ HO_2 +   M

662 R 3.4-3   HCO   + O_2 $\rightarrow$ HO_2 +   CO

663 R 3.4-4 HO_2 +   NO $\rightarrow$ OH   + NO_2
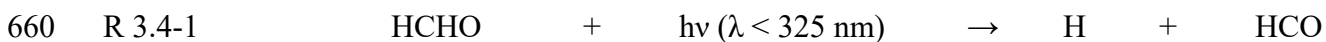
664 Unlike higher aldehydes, the OH reaction with HCHO leads also to the formation of a formyl
665 radical (HCO), which ultimately forms HO_2 (R 3.4-3).

666 R 3.4-5 $HCHO$ +   OH $\rightarrow$ H_2O +   HCO

667 Due to its solubility, the variability of HCHO also depends on the presence of clouds, and wet
668 deposition ultimately represents another important sink for HCHO (Lelieved and Crutzen, 1991).
669 Overall, HCHO plays a key role in the O_3 budget, both in polluted and remote regions.

670 Trends of the OMI HCHO tropospheric columns (hereafter referred to as TrC-HCHO) are
671 computed as described for OMI TrC-NO_2. TrC-HCHO trends over 2005-2019 are shown in
672 Figure 18 with a regional summary in Figure 19. The first global feature to highlight on the
673 global trends map is the presence of stripes along the OMI orbits. The number of rows affected
674 by the OMI row anomaly has increased over the years (Boersma et al., 2018). The affected rows
675 are filtered out in the HCHO data, but the change in the sampling and the related increase in the
676 noise impact the trend analysis. Along orbit stripes in the trend analysis should be ignored but
677 zonal trends are still valid (Figure 18).

678

**Annual trend of OMI TrC-HCHO
(based on monthly anomalies)
(Jan-Dec)**

Pmolec/cm2/yr
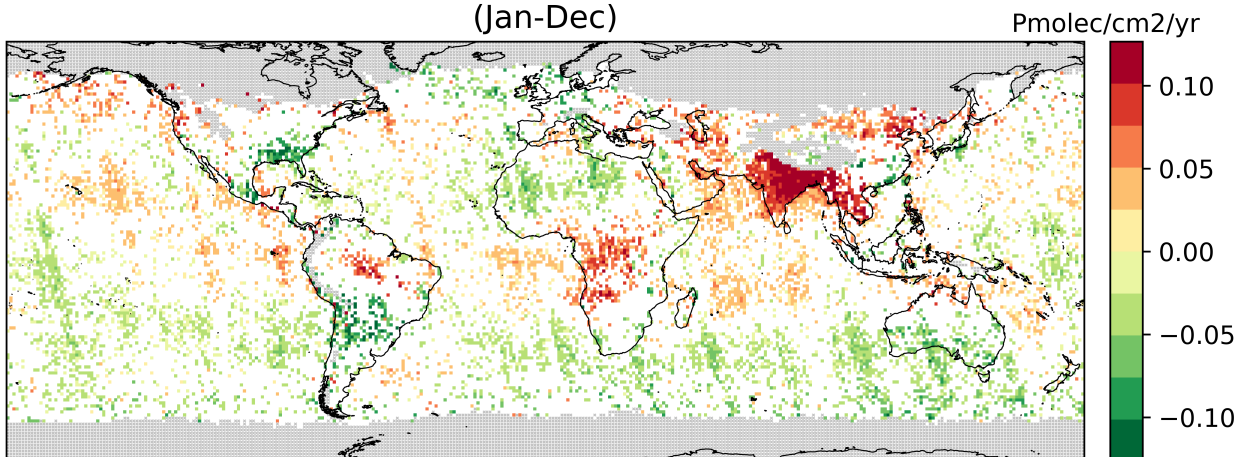
Figure 18: Global trends of OMI HCHO tropospheric column (TrC-HCHO) over 2005-2019 (see text for details on the calculation of the trends). Grey areas correspond to areas without enough data, white areas correspond to regions where the trends remain statistically low-confidence at a 95% confidence level.

Despite the fact that TrC-HCHO trends remain LC over a large part of the globe, specific regions do highlight clear trends. The region with clearest changes is unambiguously southern Asia where about 65% of the cells show increasing trends with a median of +0.09 Pmolec/cm^2/yr. The other regions with a large portion (25-30% of the cells) of increasing trends include the rest of Asia and central Africa, with median TrC-HCHO trends ranging between +0.05 and +0.08 Pmolec/cm^2/yr, as well as some parts of central Brazil (Amazonians). Conversely, some HC decreases of TrC-HCHO are observed in the south-eastern US, the southern half of Southern America, North and western Africa, and southern Australia, although part of them overlap with the aforementioned stripes and might thus not be real.
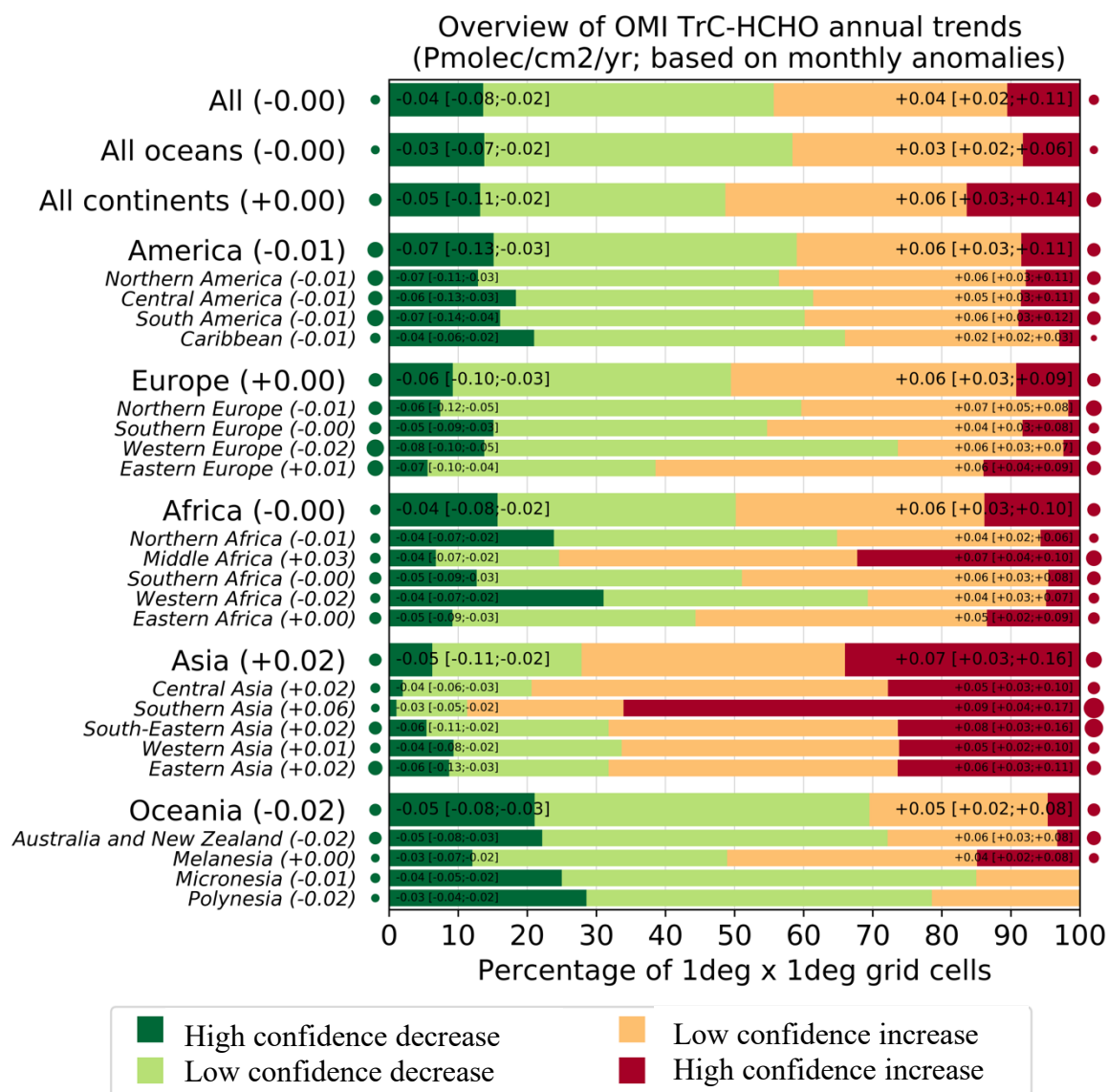
Figure 19: Summary of the statistically high- and low-confidence regional trends of OMI HCHO tropospheric column (TrC-HCHO) trends over 2005-2019, at a 95% confidence level (see text for details on the calculation of the trends). For each region, the trends reported on the left (resp. right) represent the 50th[5th, and 95th] percentiles of the trends calculated over the different grid cells showing a HC TrC-HCHO increase or decrease.

HCHO trends varies with that of O_3 (sec. 3.4.1) which might be due to several factors, such as their different sensitivity to NO_x and hydrocarbons (Luecken et al., 2018) but also possible STE contribution to tropospheric ozone levels, especially in midlatitudes (Willimas et al., 2019; Li et al., 2024). For example, while TrC-O_3 is increasing in the southeastern US, TrC-NO_2, TC-CO, and TrC-HCHO are decreasing, which, in addition to the local chemistry, might indicate a STE signal. TrC-NO_2 trends are decreasing over the northern coast of Australia while those of TrC-O_3 and TrC-HCHO are increasing. While the increase of HCHO/NO_2 might indicate a trend toward NO-limited conditions (see below), the increase of TrC-O_3 trends in this region might also indicate increasing trends of STE contribution (Li et al., 2024). However, TrC-HCHO trends are

710 consistent with that of TrC-O_3 in other regions, e.g., over the northeastern US and Europe.
711 Similarly, while NO_2 trends are slightly increasing over central and southern Australia, trends of
712 TrC-O_3 and TrC-HCHO are decreasing, which indicates a trend toward VOC-limited conditions
713 (see below).

714

715 ### 3.4.7.   HCHO/NO_2

716 The ratio of TrC-HCHO/TrC-NO_2 observed from space (e.g., Martin et al., 2004) has been used
717 in a number of studies to give insights on the O_3 chemical regime, higher (resp. lower) TrC-
718 HCHO/TrC-NO_2 ratios indicate NO_x-limited (resp. RO_x-limited) regimes. Although imperfect
719 (e.g. Souri et al., 2023), this indicator yet provides some qualitative information on the evolution
720 of the O_3 regime over the last years (Nussbaumer et al., 2023). We note that this analysis does not
721 consider variations in the ratios and their trends with respect to season or altitude. The mean TrC-
722 HCHO/TrC-NO_2 over 2005-2019 are shown in Figure 20, and the trend results are in Figure 21
723 with a regional summary in Figure 22. The highest ratios are observed in the tropical regions due
724 to strong TrC-HCHO from biogenic sources and fire NMVOC emissions in tropical South America
725 and Africa combined with relatively low TrC-NO_2. Conversely, lower TrC-HCHO/TrC-NO_2 ratios
726 are observed across western Europe and north-eastern Asia, and to a lesser extent, the northeastern
727 US.
728
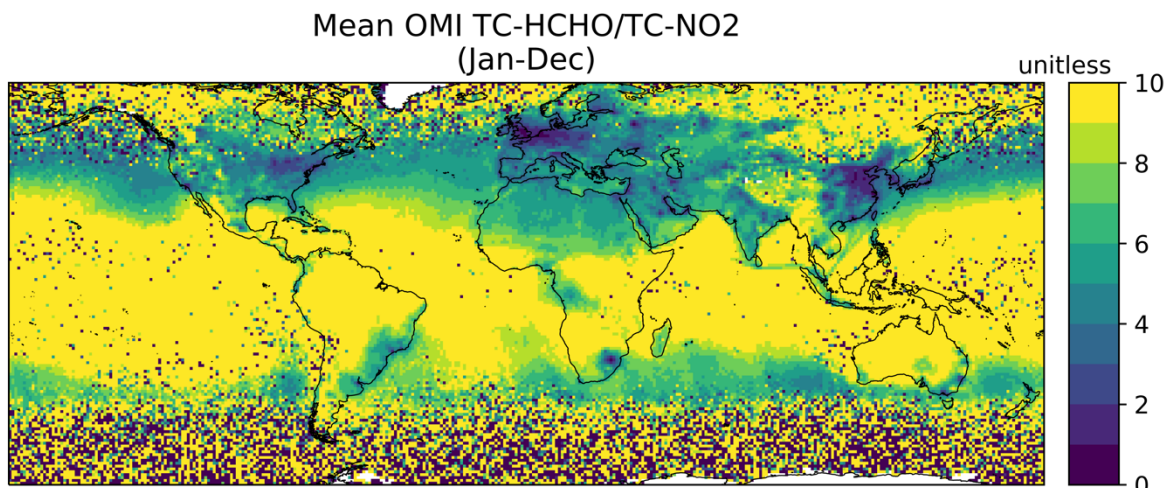
729
730 Figure 20: Global mean OMI HCHO/NO_2 tropospheric column ratio over 2005-2019.
731
732 At a global scale, the HC changes in TrC-HCHO/TrC-NO_2 trends (Figure 21-Figure 22) mostly
733 go in the direction of a reduction, with about 25% of the grid cells showing a median trend of -
734 0.52 yr^{-1}. (while only 5% of the cells show an HC increase of +0.03 yr^{-1}) as shown in Figure 22.
735 This suggests that these areas are evolving toward VOC-sensitive conditions (which does not
736 necessarily imply that they are already in this regime). This situation is observed over a large part
737 of Oceania (especially Polynesia) and specific parts of Africa, Asia, and South America. The
738 opposite HC trends, toward more NO-sensitive conditions, are mainly observed over Europe and
739 northern America, as well as South Asia. We note that the mean TrC-HCHO/TrC-NO_2 indicates
740 the mean status of the chemical regime over this period of time (2005-2019). However, the trends
741 of the TrC-HCHO/TrC-NO_2 ratio show the changing sensitivity of the chemical regime over this

period of time. For example, while the ratio in the Eastern US indicates VOC-sensitive conditions, the trends of TrC-HCHO/TrC-NO$_2$ indicate a direction toward NO-sensitive conditions.

Annual trend of OMI TrC-HCHO/NO2 (based on monthly anomalies) (Jan-Dec)
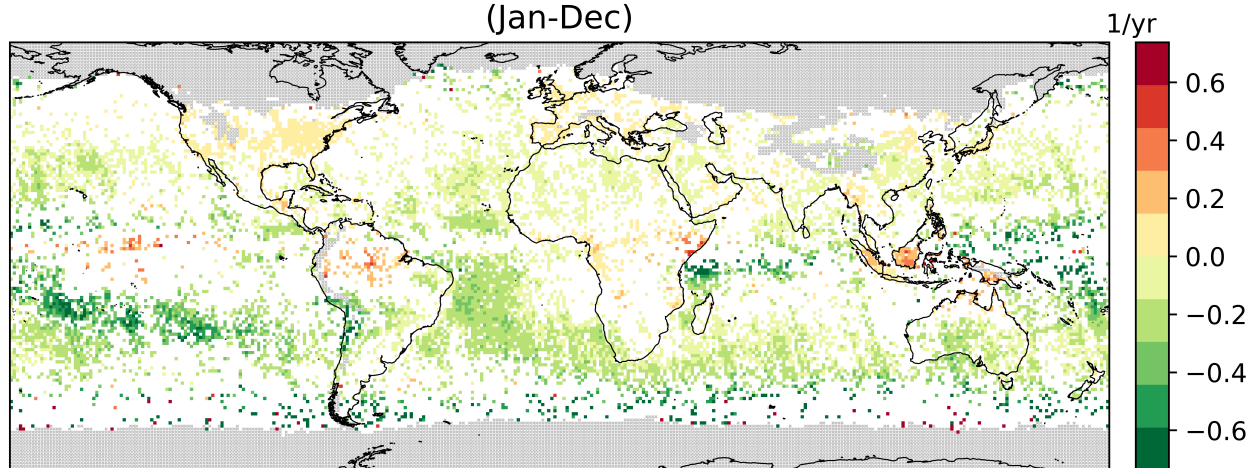
Figure 21: Global trends of OMI HCHO/NO$_2$ tropospheric column ratio over 2005-2019 (see text for details on the calculation of the trends). Grey areas correspond to areas without enough data, white areas correspond to regions where the trends remain statistically low-confidence at a 95% confidence level.

The trends on the TrC-HCHO/TrC-NO$_2$ ratio is mainly driven by specific trends on TrC-HCHO and/or TrC-NO$_2$, depending on the region. The ratio increase in southern and western Europe and southeast Asia appears primarily due to decreasing TrC-NO$_2$, since TrC-HCHO does not change with HC. Over North America, observed TrC-HCHO values decrease but less than TrC-NO$_2$, which thus drives the ratio toward an increase. Conversely, the increase of TrC-HCHO/TrC-NO$_2$ in equatorial Africa and Amazonians appears mainly driven by increasing TrC-HCHO. The regions with HC decreasing TrC-HCHO/TrC-NO$_2$ ratio include Chile and Australia, due to both decreasing TrC-HCHO and increasing TrC-NO$_2$ (Figure 22), indicating a trend towards a VOC-limited regime. Note that over the US, Jin et al. (2020) demonstrated the reasonable ability of the OMI-based TrC-HCHO/TrC-NO$_2$ trends to capture the transition from RO$_x$-limited to NO$_x$-limited regimes over main US cities and found a relatively good consistency between observed changes of the surface O$_3$ and space-based HCHO/NO$_2$ increasing trends.
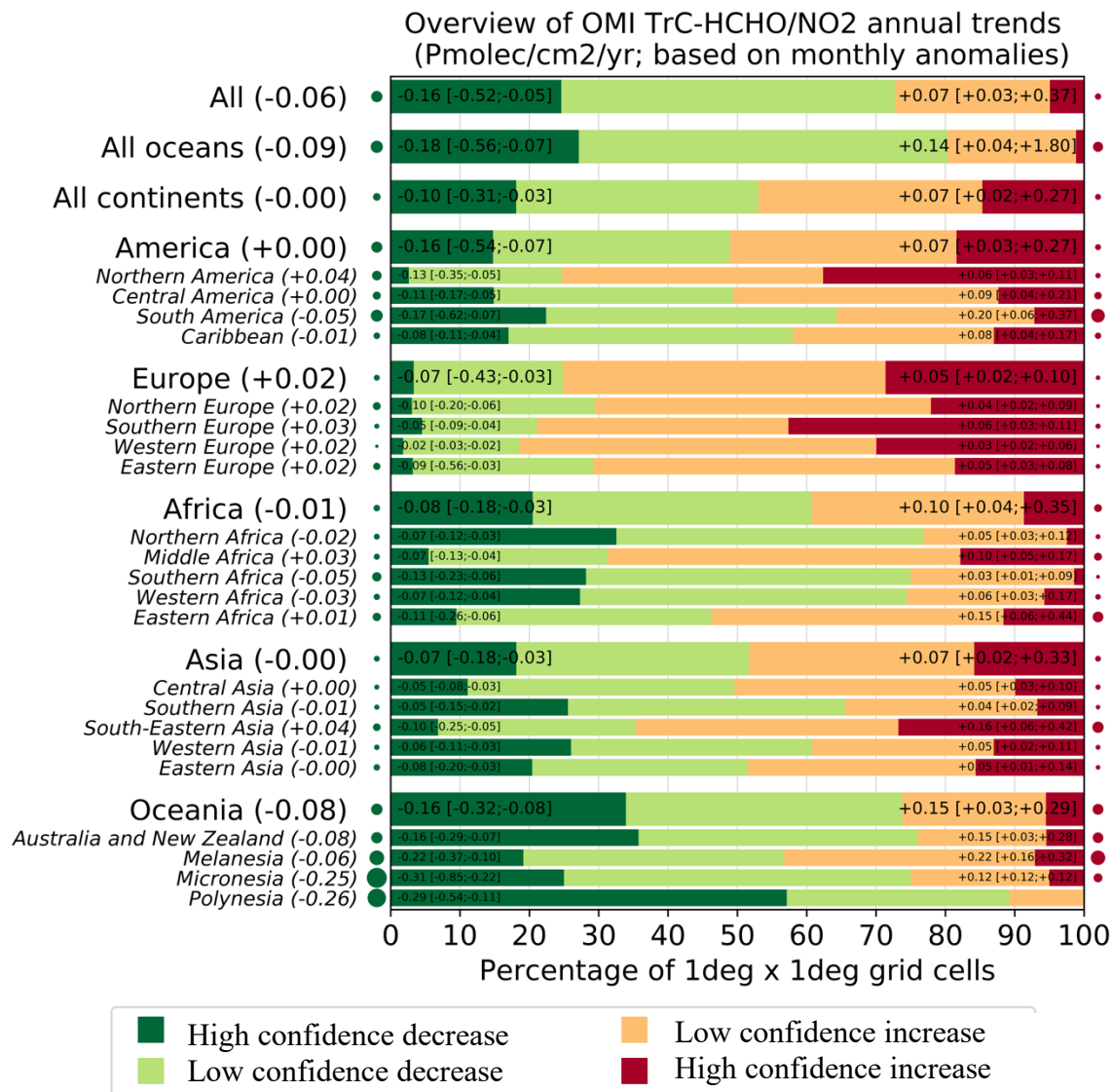
Figure 22: Summary of the statistically high- and low-confidence regional trends of OMI TrC-HCHO/TrC-NO$_2$ tropospheric column ratio trends over 2005-2019, at a 95% confidence level (see text for details on the calculation of the trends). For each region, the trends reported on the left (resp. right) represent the 50th[5th, and 95th] percentiles of the trends calculated over the different grid cells showing a high confidence TrC-HCHO/TrC-NO$_2$ increase or decrease.

773

3.5. Lightning NO_x and Its Effects on Tropospheric NO_x and O_3

Nitric oxide (NO) is produced in lightning flash channels and quickly comes into equilibrium with NO_2. Cloud-scale simulations of thunderstorms indicate that 55-75% of lightning NO_x (LNO_x) is detrained above 8 km (Pickering et al., 1998) where it enhances upper tropospheric NO_y, OH, and O_3 (Labrador et al., 2005; Allen et al., 2010; Liaskos et al., 2015) and contributes to enhanced longwave radiative absorption by O_3 (Lacis et al., 1990; Finney et al., 2018). Enhanced OH leads to a decrease in CH_4 lifetime and decreased longwave radiative absorption (Fiore et al., 2006; Finney et al., 2018). The lifetime of NO_x in the upper troposphere is controlled by the chemical cycling of NO_x with reservoir species and is 10-20 days away from deep convection (Prather and Jacob, 1997) but only 2-12 hours in the vicinity of convection (Nault et al., 2016, 2017). This chemical recycling provides a source of NO_x downwind of thunderstorms, which causes the ozone production efficiency of emitted NO_x to be 4-20 times higher in the upper troposphere than at the surface. Thus, LNO_x has a disproportionate impact on the tropospheric O_3 budget (Pickering et al., 1990; Grewe et al., 2001; Sauvage et al., 2007).

The distribution of lightning is fairly well known over much of the Earth due to remote sensing observations and an increase in the number and capability of ground-based lightning networks. However, the LNO_x production efficiency (PE, mol fl^{-1}) is a continued source of uncertainty. Schumann and Huntrieser (2007) reviewed the literature on LNO_x production, finding a best estimate of 250 moles per flash, with uncertainty factors ranging from 0.13 to 2.7. The PE can be estimated from theoretical and laboratory considerations (Price et al., 1997; Koshak et al., 2014), using thunderstorm anvil observations by aircraft (Ridley et al., 2004; Huntrieser et al., 2008, 2011; Pollack et al., 2016; Nault et al., 2017; Allen et al., 2021a), based on satellite data (Bucsela et al., 2010; Beirle et al., 2010; Pickering et al., 2016; Bucsela et al., 2019; Lapierre et al., 2020; Zhang et al., 2020; Allen et al., 2019, 2021b), or using cloud-resolved (e.g., DeCaria et al., 2000; 2005; Fehr et al., 2004; Ott et al., 2007, 2010; Cummings et al., 2013; Pickering et al., 2023) or global model simulations with chemistry (e.g. Martin, et al., 2007; Murray et al., 2012; Miyazaki et al., 2014; Marais et al., 2018). These various techniques have yielded PE estimates ranging from <50 to >1000 mol fl^{-1}, with most estimates in the 100-400 mol fl^{-1} range. Miyazaki et al. (2014) assimilated OMI NO_2, MLS and TES O_3, and MOPITT CO into a chemical transport model to provide comprehensive constraints on the global LNO_x source, resulting in an estimate of mean PE of 310 moles per flash. Marais et al. (2018) used cloud-sliced upper tropospheric NO_2 from OMI together with the GEOS-Chem model to estimate a mean LNO_x PE of 280 moles per flash. Lightning is the dominant source of NO_x in the tropical upper troposphere year-round and in the northern mid-latitudes in summer. Lightning is responsible for 10-15% of NO_x emissions globally. Assuming 100-400 mol fl^{-1}, the global LNO_x production is likely $2 - 8$ Tg N a^{-1} (Schumann and Huntrieser, 2007; Verma et al., 2021). LNO_x impacts air quality and deposition (Kaynak et al., 2008; Allen et al., 2012). On average LNO_x adds 1-2 ppbv to surface O_3 (Kang et al., 2019b), although contributions as large as 18 ppbv have been seen for individual events (Murray et al., 2016). Allen et al. found that the addition of LNO_x to the Community Multiscale Air Quality (CMAQ) model increased wet deposition of oxidized nitrogen at National Atmospheric Deposition Program (NADP) sites by 43%, reducing low biases from 33% to near-zero. Kang et al. (2019b) found similar improvements for wet deposition and also found that including LNO_x resulted in smaller biases with respect to ozonesondes and aircraft profiles taken during the NASA DISCOVER-AQ field campaign (Flynn et al., 2016). Thus, to accurately assess its impacts on air quality, it is critical that LNO_x-producing deep convection is accurately simulated.

Only in recent years with the advent of satellite observations of lightning flashes and improved coverage by ground-based lightning networks has there been sufficient data to make estimates of trends in the occurrence of lightning. However, it is unknown whether trends in LNO_x production are similar to those of lightning itself. Lightning characteristics such as the ratio of intracloud (IC) flashes to cloud-to-ground (CG) flashes, the multiplicity (i.e., the number of strokes per flash), and the peak current or energy associated with flashes may vary over time. All of these lightning characteristics may have effects on the magnitude of LNOx production. We have insufficient data to take into account these possible effects on LNO_x production over large spatial domains or over sufficiently long periods of time.

3.5.1. Global Historical Trends of Lightning

The first attempts at an examination of trends in thunderstorm activity were conducted in terms of thunder-days (in Japan by Kitagawa et al., 1989; in Brazil by Pinto et al., 2013). A more recent global analysis was conducted by Lavigne et al. (2019), who analyzed trends in thunder-days (number of days with audible thunder at weather observation stations) over 43 years and in flashes recorded by the Lightning Imaging Sensor (LIS) on the Tropical Rainfall Measuring Mission (TRMM) for 16 years. Thunder-days increased since the 1970s in the Amazon Basin, the Maritime Continent, India, Congo, Central America, and Argentina. Decreases in thunder-days were found in China, Australia, and the Sahel region of Africa. Lavigne et al. (2019) do not provide a global trend in thunder days, but an average trend computed over the nine primary lightning regions that they considered, weighted by the mean annual thunder days in each region, yields a near global estimate of +3.8% per decade. How well do thunder-days represent lightning flash rate? Lavigne et al. found a positive correlation between thunder-days and LIS flash rates in China, the Maritime Continent, South Africa and Argentina, but disagreement on the trend in India and West Africa.

Large-scale (±38º latitude) trends in lightning flashes have been examined in the data collected by the LIS on the TRMM satellite (January 1998 – December 2014) and on the International Space Station (February 2017 – December 2021). Füllekrug et al. (2022; see Figure SB2.1b) demonstrate that the annual mean deviations from the 1998 – 2021 mean are no more than ~5% except for ~-10% in 2020 and ~-8% in 2021. However, no long-term trend is evident from the LIS data. The possibility that these larger negative deviations in 2020 and 2021 are due to Covid-19 lockdowns and general declines in economic activity has been speculated. The link may be provided by changes in Aerosol Optical Depth (AOD) as suggested by Liu et al. (2021) who demonstrated 10-20% flash reductions in March – May 2020 relative to the 2018 – 2021 mean for those months from the GLD360 and WWLLN ground-based lightning networks. Regional lightning reductions were consistent with AOD reductions noted by Sanap (2021). Larger reductions in lightning were noted over Africa/Europe and Asia/Maritime Continent and lesser reductions over the Americas.

3.5.2. Regional Historical Trends of Lightning

Widely varying trends in lightning over China have been reported in the literature. To some extent, whether the trend in lightning is upward or downward depends on the particular region studied and on the period of time considered. Yang and Li (2014) were the first to report on lightning trends in China. They used lightning data from the TRMM/LIS sensor and human-observed thunderstorm day occurrence over the period 1990 to 2012 in southeastern China. Thunderstorms and lightning occurrence increased over the period as well as LIS precipitation radar echo tops heights. These increases were accompanied by decreases in visibility, indicating increases in pollution aerosol. Detailed work on lightning trends in China has been performed in relation to aerosols. Shi et al. (2020) correlated flashes from the TRMM/LIS Low-Resolution Monthly Time Series (2.5 deg. resolution) with AOD from MODIS-Terra V6.1 Level 3 over the period 2001 to 2014. For AOD

866 < 1.0, r = 0.64, indicating a likely microphysical effect on lightning flash rate. For AOD > 1.0, r =
867 -0.06, which could indicate that with higher aerosol concentration there is a radiation effect
868 stabilizing the atmosphere and/or a decrease in the number of graupel particles in the mixed-phase
869 region of the storms that is important for charging. Flashes were also correlated with surface
870 relative humidity and Convective Available Potential Energy (CAPE). As AOD generally
871 increased over much of the early portion of this time period and then decreased, lightning flash
872 rates followed similar trends. Wang et al. (2021) examined a 9-year record (2010- 2018) of CG
873 lightning from the China Lightning Detection Network in three polluted urban areas of China
874 (Chengdu, Wuhan, and Jinan). They found decreasing trends (see Wang et al., 2021) in CG
875 lightning and total AOD (from the MERRA-2 reanalysis). Annual mean lightning density in these
876 three regions decreased by 50 – 75% as annual mean AOD fell from 0.70 – 0.75 to 0.53 to 0.62.

877 Qie et al. (2022) analyzed the OTD/LIS record from 1996 through 2013, and found that lightning
878 increased over the eastern Tibetan Plateau by $0.072 \pm .069$ fl km^2 yr^{-1}. Over the 18 years, this
879 increase amounted to a total of 1.3 fl km^2 yr^{-1}, compared with a climatological value of 7.7 fl km^2
880 yr^{-1}, thereby indicating a HC increase. The ground-based World Wide Lightning Location Network
881 (WWLLN) also showed increased strokes in this region. The increase in lightning frequency in
882 this region was found to be due to an increase in thunderstorm frequency, not increased storm
883 intensity.

884 Koshak et al. (2015) analyzed National Lightning Detection Network (NLDN) CG flashes over
885 the contiguous United States (CONUS) from 2003 to 2012. The five-year mean flashes over 2008
886 to 2012 decreased by 12.8% from the five-year mean for 2003 to 2007 (Table 1). The CONUS
887 average wet bulb temperature also trended downward during this period, which may have led to
888 lesser or weaker storms. However, US Environmental Protection Agency air quality trends show
889 an 18% decrease in PM2.5 concentrations over CONUS between the two subperiods, which also
890 could have had an influence on the flash rates. A recent effort to update the Koshak et al. (2015)
891 analysis is underway. NLDN flashes have been reprocessed (Kenneth Cummins, personal
892 communication) from 2015 through 2021 to ensure that the classification of IC and CG flashes is
893 done consistently with data prior to 2015. Trend analysis of NLDN CG flashes from 2003 (a major
894 upgrade of the NLDN network hardware) through 2022 (William Koshak, personal
895 communication) shows a HC reduction in CG flashes over CONUS, comparing the mean CG
896 flashes over 2003-2004 with the mean over 2021 -2022. Within this period a major decrease
897 (~25%) in CONUS CG flashes occurred from 2011 to 2012. Flashes in 2013 remained low, but
898 recovered by 2014-2015. A major decrease (~27%) occurred from 2019 to 2020, with a small
899 increase in 2021. These results have been obtained from ongoing efforts by Dr. William Koshak
900 of the NASA Marshall Space Flight Center, and are presently part of a draft manuscript by lead
901 author Koshak that extends and refines the earlier work in Koshak et al. (2015). Details concerning
902 these trends will be contained in that manuscript.

903 A possible contributing factor to the CONUs decline in CG flashes over 2003 to 2021 is the
904 substantial decrease in aerosol. Surface annual average PM2.5 concentrations averaged over
905 CONUS decreased by 37% from 2000 to 2021 according to the EPA National Air Quality Trends
906 Report (https://www.epa.gov/air-trends/air-quality-national-summary). However, no decrease in
907 CONUS annual average PM2.5 was seen from 2019 to 2020. As mentioned previously, AOD may
908 be a better indicator of the aerosol amount that may become incorporated into thunderstorm clouds.
909 Sanap (2021) showed negative anomalies of AOD of ~0.1 in portions of CONUS in March and
910 April 2020 and 0.1 to 0.2 in May 2020. The major decrease in CONUS CG flashes from 2011 to
911 2012 has been related to drought conditions during Summer 2012 over the South Central and
912 Southeastern US (Koshak et al., 2015). The reason for the number of CONUS flashes remaining

lower in 2013 is uncertain. Koehler (2020) analyzed 26 years (1993 – 2018) of NLDN CG lightning data to construct a thunder-day climatology for CONUS. Positive anomalies from the 26-year mean were found from Texas to Colorado during 2003 to 2007, and negative anomalies in this region during 2008 to 2012. These anomalies were consistent with precipitation anomalies associated with ENSO.

Holzworth et al. (2021) analyzed primarily CG lightning data from WWLLN for June, July, and August for the years 2010 through 2020. The ratio of lightning strokes north of 65° N latitude to the total global strokes increased by a factor of three over this period. This increase occurred as the surface temperature anomaly in this region increased by 0.3°C (see Holzworth et al., 2021). These results suggest a substantial increase in upper tropospheric NO_x and subsequent ozone production at high northern latitudes.

3.5.3.   Future Lightning Trends

Parameterizations in global chemistry and climate models have been developed for lightning flash rate. These schemes typically use kinematic, thermodynamic or microphysical variables from the model as predictors. In some studies such predictors have simply been applied to output from multiple climate models. This is the case with the Romps et al. (2014) work, which showed that when a lightning parameterization scheme using CAPE x Precipitation Rate is applied to 11 climate models an increase in CG lightning by 12 +/- 5% per degree Celsius of climate warming was computed. This work simply used the 12-hour resolution time series of spatial means of these variables over CONUS as input. Changes in IC lightning flashes were not considered. IC flashes typically outnumber CG flashes by a factor of 3 averaged over CONUS. Therefore, the result of this work is unknown with respect to the amount of change in LNO_x emission. Romps et al. (2018) updated their analysis using CAPE from 3-hourly North American Regional Reanalysis (NARR) data and hourly precipitation from NOAA River Forecast Centers, finding that CAPE x Precipitation Rate captures the spatial, seasonal, and diurnal variations of NLDN CG flash rate over land, but does not predict the pronounced land-ocean contrast in flash rates. Therefore, these analyses are of limited value in estimating trends of LNO_x over broader-scale regions. Romps et al (2019) tested four lightning proxies in a cloud-resolved 4-km resolution simulation over CONUS with the Weather Research and Forecasting (WRF) model, and over the tropical oceans with a Radiative Convective Equilibrium model. The proxies were CAPE x Precipitation Rate, precipitation with vertical velocity > 10 m/s, vertical ice flux at the 260K isotherm, and vertical integral of cloud ice and graupel product. The fractional change in proxy values per 1 degree Celsius of warming over CONUS was +8 to +16%. Over the tropical oceans the changes in proxy values per degree ranged from +12% for CAPE x Precipitation Rate to -1% for ice flux and -3% for the cloud ice and graupel product. Therefore, over broad regions of the Earth, there is great uncertainty on future trends in lightning.

Finney et al. (2016; 2018) compared lightning projections for 2100 using vertical ice flux (Finney et al., 2014) and cloud-top height parameterizations for flash rate in the UK Chemistry and Aerosols Model. They obtained -15% global change in total flash rate with ice flux under a strong global warming scenario (see Finney et al., 2018), which was composed of a greater decrease in the tropics and small increases in mid-latitudes. In terms of LNO_x emissions this work using the ice flux scheme produced -0.15 TgN K^{-1} change over the years from 2000 to 2100, implying less O_3 production. With the cloud-top height scheme they obtained +0.44 TgN K^{-1} LNO_x change, implying increased O_3 production. However, the ice flux scheme provided a more realistic

959 representation of global lightning for present day. Therefore, the negative LNOx emissions change
960 from this scheme may be more realistic. If indeed the ice flux scheme better represents the current
961 distribution of lightning, both the Romps and Finney results suggest LC increase in LNOx
962 emission in future climate, and possibly a small global decrease. Murray (2018) points out that the
963 ice flux scheme is a closer representation of the underlying charging mechanism, but this scheme
964 needs to be tested in multiple global chemistry and climate models.

965

3.5.4.   Recent findings concerning LNOx PE

967 Recent satellite-based estimates of LNOx production (Figure 23) have suggested a possible flash
968 rate dependence of LNOx production per flash (Bucsela et al., 2019; Allen et al., 2019; 2021).
969 Smaller values of LNOx PE in these studies were found to be associated with high flash rates,
970 likely due to smaller flashes in these conditions (Bruning and Thomas, 2015). Allen et al. (2021a)
971 noted positive correlations (Figure 23) of LNOx PE with flash energy and with flash multiplicity
972 (number of strokes per flash). Laboratory studies by Wang et al. (1998) found a positive correlation
973 between peak current and LNOx production. Koshak et al. (2015) found an 8% increase in peak
974 current from the 2003-2007 period to the 2008-2012 period that accompanied the 12.8% decrease
975 in CG flashes. These findings make it difficult to project future LNOx production given only a
976 prediction of future lightning flashes.

977
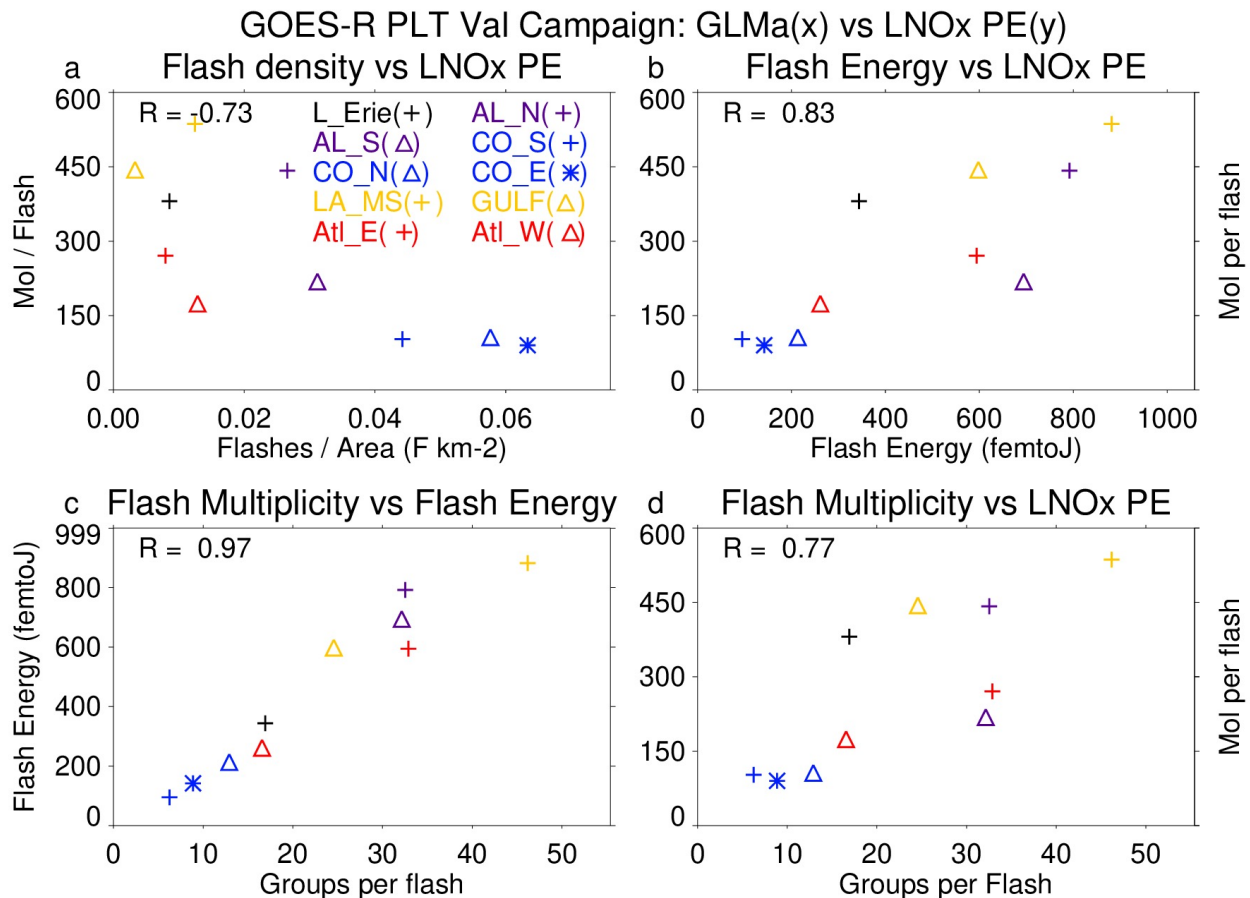
979 Figure 23. Scatterplots showing the GLMa-derived relationship between (a) LNOx PE (mol per
980 flash) and flash density (flashes km−2), (b) LNOx PE and flash energy (fJ), (c) flash energy and

981   flash multiplicity, and (d) LNO_x PE and flash multiplicity. Colors are used to separate flight days
982   while symbols are used to separate system within each flight day. Correlations are shown in the
983   upper right. LNOx PE derived from airborne remote sensor, the Geo-CAPE Airborne Simulator
984   (GCAS) during the GOES-R Post-launch Test field campaign. GLMa indicates Geostationary
985   Lightning Mapper data adjusted for missing data. From Allen et al. (2021a).

986

987   ### 3.5.5. Impacts of LNOx on upper tropospheric O_3

988   The literature concerning the effects of lightning NO_x production on upper tropospheric ozone
989   focuses on photochemical ozone production in storm outflow The STERAO-A storm simulation
990   by DeCaria et al. (2005) indicated that additional ozone production attributable to lightning NO
991   within the storm cloud during the lifetime of the storm was very small (~2 ppbv). However,
992   simulation of the photochemistry over the 24 hours following the storm showed that an additional
993   10 ppbv of ozone production in the upper troposphere can be attributed to lightning NO production.
994   Convective transport of HO_x precursors led to the generation of a HO_x plume, which substantially
995   aided the downstream ozone production. Ott et al. (2007) simulated the July 21, 1998 EULINOX
996   thunderstorm. During the storm, the inclusion of lightning NO_x in the model combined with
997   convectively-transported boundary layer NO_x from the Munich, Germany region resulted in
998   sufficiently large NO_x mixing ratios to cause a small titration loss of ozone (on average less than
999   4 ppbv) at all model levels. Simulations of the chemical environment in the 24 hours following the
1000   storm show on average a small increase in the net production of ozone at most levels resulting
1001   from lightning NO_x, maximizing at approximately 5 ppbv per day at 5.5 km. Between 8 and 10.5
1002   km, lightning NO_x caused decreased net ozone production. Ren et al. (2008) found that net
1003   tropospheric ozone production proceeded at a median rate of ~11 ppbv per day above 9 km in the
1004   Intercontinental Transport Experiment (INTEX-A) in which the effects of frequent deep
1005   convection over the United States dominated the upper troposphere. Apel et al. (2012) noted that
1006   a box model calculation indicated a net ozone increase of ~10 ppbv over a few hours following
1007   observed convection with lightning over Canada in the Arctic Research of the Composition of the
1008   Troposphere from Aircraft and Satellite (ARCTAS) experiment. Apel et al. (2015) performed box
1009   modeling of the chemistry downwind of two DC3 storms in northeast Colorado on June 22, 2012
1010   finding greater ozone production over 2 days (14 ppbv) in the southern storm with more LNO_x
1011   than in the northern storm (11 ppbv). Brune et al. (2018) studied ozone production in the outflow
1012   of the June 21, 2012 DC3 mesoscale convective system. Their Box model calculations yielded a
1013   13 ppbv increase in ozone over 5 hours, similar to the observed 14 ppbv increase. This rate of
1014   increase is larger than others in the literature, perhaps because for a portion of the 5 hours the
1015   outflow was in cirrus cloud, in which photolysis rates may have been larger than clear-sky values
1016   due to multiple scattering. Using a regional chemistry model, Pickering et al. (2023) estimated that
1017   net ozone production in the upper tropospheric outflow of a severe high flash rate storm observed
1018   over Oklahoma proceeded at a rate of 10-11 ppbv day^{-1} during the first 24 hours of downwind
1019   transport. Downwind photochemical production of ozone due to LNO_x accounted for much of the
1020   recovery of upper tropospheric ozone following large reductions due to convective transport of
1021   lower ozone boundary layer air.

1022   ### 3.5.6. Summary of LNO_x

1023 LNO_x is responsible for the largest fraction of upper tropospheric ozone in the tropics year-round
1024   and in the mid-latitudes in summer. Effects on longwave radiation due to ozone are most sensitive
1025   due to the ozone near the tropopause. Therefore, it is of great importance to have knowledge of
1026   the trends in ozone in this region that are due to changes in frequency and characteristics of

1027 lightning flashes. Considerable uncertainty remains concerning trends in global thunder days. No
1028 long-term trend in global flash rates has been found. However, regionally important trends have
1029 been noted in CONUS and in China, which tend to be correlated to the decreasing atmospheric
1030 aerosol content. An increasing trend at Arctic latitudes has been noted, as that region rapidly
1031 warms. Future trends in flash rate also are uncertain, with conflicting predictions coming from
1032 models with differing flash rate parameterizations. Flash characteristics (e.g., flash rate, flash
1033 extent, flash energy or peak current, intracloud fraction) have been found to have important
1034 implications for LNO_x production per flash. Insufficient knowledge of these characteristics on a
1035 global scale makes it highly uncertain to estimate changes in LNO_x production, even with
1036 knowledge of flash rate trends.

1037

1038 **3.6. Soil NO and HONO emissions and their impacts on O_3**

1039 Nitrous acid (HONO) is produced from microbial activity in soils with a similar mechanism and
1040 strength as NO (Oswald et al., 2013). This emission source may partially account for the current
1041 mismatch between observed and simulated HONO levels in the lower troposphere (Su et al.,
1042 2011; Yang et al., 2020). Zhang et al. (2016) estimate a 29 % contribution of soil-HONO to the
1043 HONO sources in China. This may also contribute substantially to OH production with important
1044 implications for the HO_x and O_3 budget. To account for this emission source and assess the
1045 global potential for atmospheric pollution soil-HONO emissions have been parameterized based
1046 on the HONO/NO emission ratio measured at multiple field samples (taken from different
1047 regions of the world) and up-scale it to the 4 major land cover types applied to the whole globe.
1048 The study estimates a global emission source of 7 TgN/yr from soil-HONO in 2009 (Emmerichs
1049 et al., 2023). This is at the lower end of the estimated range of 7.4-12 TgN/yr presented by Wu et
1050 al. (2022) for 2017 who employ an empirical and statistical model in combination with
1051 observations. Due to the importance of NO and HONO soil emissions for the O_3 budget their
1052 variability and historical and future trends are described here and linked to O_3. Additionally, we
1053 discuss a modification of the soil NO emission scheme.

1054 **3.6.1.   Global modeling of reactive nitrogen emissions from soil**

1055 In this section, we present a short overview of the soil-NO emission algorithms and estimates for
1056 regional and global emissions. The emission of nitrogen oxides (NO) from the soil is the major
1057 source of NO_x in unpolluted regions accounting for 15-25 % of global emissions (Weng et al.,
1058 2020, Vinken et al., 2014). Thereby, NO is produced from the nitrification in soil (microbial
1059 activity) and depends non-linearly on soil properties like pH, carbon and nutrient content,
1060 temperature, and soil moisture (Gödde and Conrad 2000, Oswald et al. 2013). Model algorithms
1061 estimate soil-NO emissions with a function dependent on biological and meteorological drivers.
1062 The common empirical approach by Yienger and Levy (1995), which is used in the current
1063 CMIP6 simulations (Szopa et al. 2022), is based on a biome-specific emission factor, soil
1064 temperature, precipitation, and the canopy uptake reduction factor. The resulting global estimate
1065 is in the range of 3.3-7.7 TgN/yr which is, however, only at the lower end of the more recent
1066 model and observation-based estimates. The Yienge and Levy (1995) approach generally
1067 underestimates soil NO for all landcover types except in the tundra and rainforest due to the
1068 pulsing parameterization, which describes a large NOx release at the wetting of very dry soil and
1069 the subsequent rapid decay (Steinkamp et al., 2009). This is accounted for in the more
1070 mechanistic approach by Hudman et al. (2012) representing pulsing of the emissions following
1071 dry spells and N-inputs from chemical fertilizer and atmospheric N-deposition. This approach
1072 calculates spatial and temporal patterns of soil moisture, temperature, pulsing, fertilizer, manure

1073 and atmospheric N deposition and biome overall replacing the emission factors by Yienger and
1074 Levy (1995) which yields in comparison 34 % more annual global soil emissions of nitrogen
1075 oxide (10.7 TgN/yr). Satellite top-down estimates range from 7.9 TgN/yr (Miyazaki et al., 2017:
1076 2005-2014, assimilation of satellite data sets) to 16.7 TgN/yr (Vinken et al., 2014; GEOS-Chem
1077 and OMI). The emission of soil-NO varies regionally with small sources in Australia (~0.5
1078 TgN/yr), Europe, Russia and Southern Hemisphere (SH) Africa (0.7 TgN/yr, 0.8 TgN/yr),
1079 America (0.9-1 TgN/yr) and high values in S.E. Asia and Northern Hemisphere (NH) Africa (2-
1080 2.1 TgN/yr). The emission estimates (here for 0.25° lat. × 0.3125° lon.) increase with resolution
1081 in some regions like Europe by 38 % (Weng et al., 2020).

1082 Nitrous acid (HONO), a major OH source, is also produced from microbial activity in soils with
1083 a similar mechanism and strength as NO (Oswald et al., 2013). This additional emission source
1084 may account for the current mismatch between models and measurements representing HONO
1085 levels in the lower troposphere (Su et al., 2011; Yang et al., 2020). Soil emissions of HONO play
1086 a major role in the daytime-HONO concentrations in rural areas (in the lowest layers) where
1087 traffic emissions and NO_2 heterogeneous reactions occur less than in urban areas (Wu et al.
1088 2022). HONO photolysis is a main OH source and impacts the oxidation capacity of the
1089 atmosphere (Zhang 2016, 2019). Therefore, this may also contribute significantly to OH
1090 production with important implications for the HO_x and O_3 budget.

1091 ### 3.6.2. Variability and trends of soil emissions of NO and HONO in the last 15 years

1092 The magnitude of soil emissions varies strongly with season where the emissions rise from
1093 January and July by a factor of 2.5 (Weng et al., 2020). This follows the meteorological
1094 variability as for instance, heavy rainfall over dry grasslands/forests causes a pulse of soil NO
1095 emissions coupled with the usage of fertilizer (Hudman et al., 2012). According to the CCMI
1096 simulations by Jöckel et al. (2016) (following the future ('medium high') climate scenario
1097 RCP6.0 the soil NO emissions show a positive trend since pre-industrial times with a steeper
1098 increase of up to 0.3 TgN/decade from the year 2000. As soil emissions of HONO rely on the
1099 same biogeochemical process with similar dependencies on temperature and water content as NO
1100 also increased from 2000 to 2019.

1101 For soil-HONO, however, the trend over 2005-2019 is much smaller, most pronounced in
1102 Central Africa (Figure 25). Thereby, the highest positive monthly anomalies occur mainly in the
1103 5 most recent years which is likely due to the more frequent heat wave occurrence, e.g. in Europe
1104 and North America. Overall, Africa relates the most (~30%) to the global anomaly (Figure 24 -
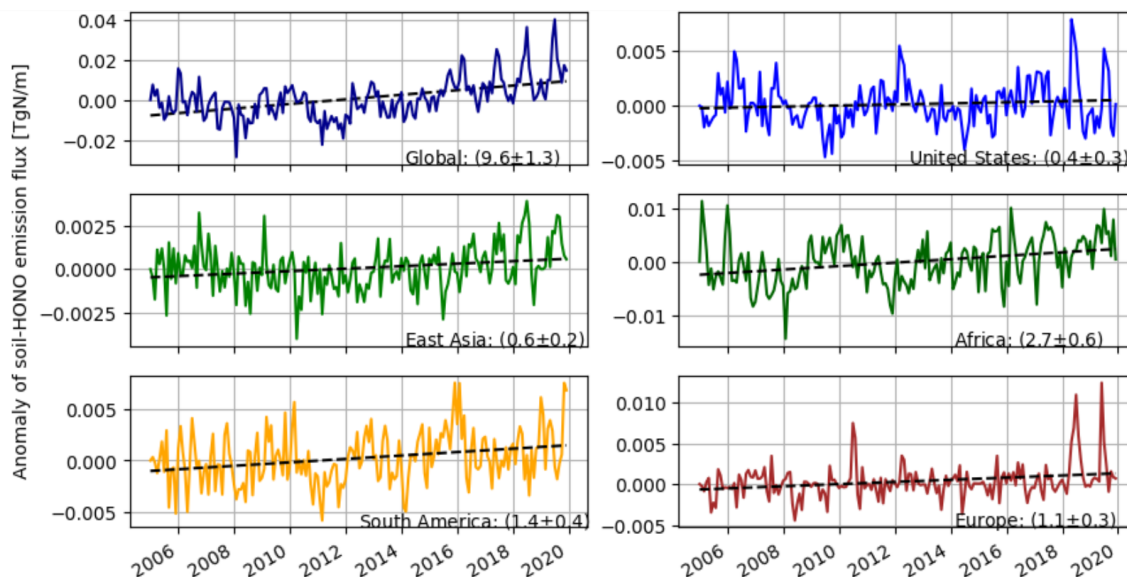1105 Figure 25).

1106
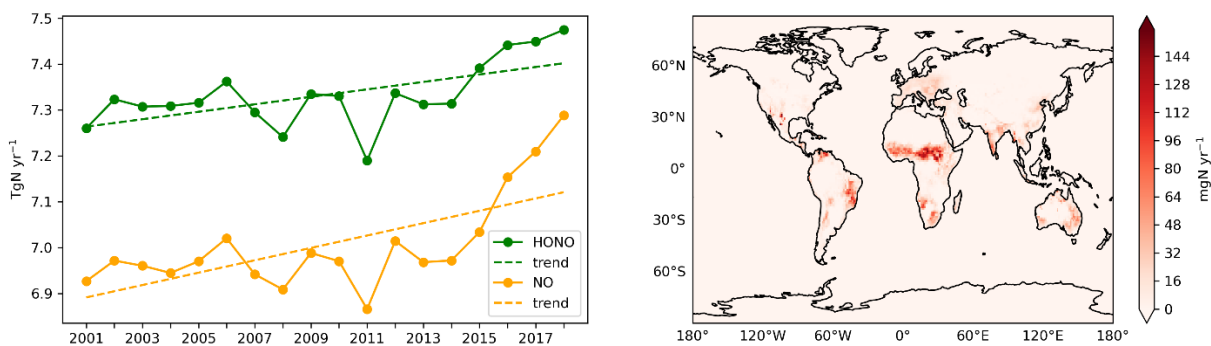
1107

1108   Figure 24: Time series of soil-HONO and soil-NO emissions and their trends (left) and the mean
1109   global distribution of the soil-HONO emission trend for 2005-2019 based on monthly anomalies
1110   (right).

1111

1112

1113

1114

1115   Figure 25: Monthly anomalies of HONO emissions from soil (de-seasonalized). The trend is
1116   given in 10^{-5}, including the uncertainty estimate (2*standard deviation).

3.6.3.   Canopy Reduction Factor

1118   Most NO soil emission models (Yienger and Levy, 1995; Hudman et al., 2012) rely on an
1119   empirical canopy reduction scheme which represents loss processes in plants as the diffusion of
1120 NO_2 through the stomata and direct deposition to the cuticle. In particular, a large fraction of
1121 NO_x (and peroxyacyl nitrate) loss during the night may be only explainable by non-stomatal
1122   processes (Delaria et al., 2020b). Mechanistically, the canopy reduction can be described by an
1123   efficient NOx deposition to plants. Thus, Delaria et al. (2020a) points out that models already
1124   represent the uptake by vegetation and do not need to use a canopy reduction scheme. The
1125   potential change of NO soil emissions is shown by employing the global model
1126   ECHAM/MESSy (1°x1°) with an explicit trace gas uptake at stomata and cuticle (Emmerichs et
1127   al., 2021) for two different seasons in 2005 and 2006. Removing the canopy reduction factor in
1128   the model leads to a HC increase of soil NO emissions highest over tropical forests (Figure 26).
1129   The temporal variation follows the vegetational growth as in the Northern Hemisphere summer
1130   50% higher emissions occur. These findings are reasonable as Hudman et al. (2012) estimated
1131   that the canopy reduction scheme overall lowers the NO emissions by 10-15% in grasslands and
1132   up to 85% over forests (GEOS-Chem at 2°×2.5° in 2006). Consequently, improper accounting
1133   for the canopy reduction factor may imply a strong underestimation of the soil-N in densely
1134   forested regions and globally by about 31% (2005-2006).

1135
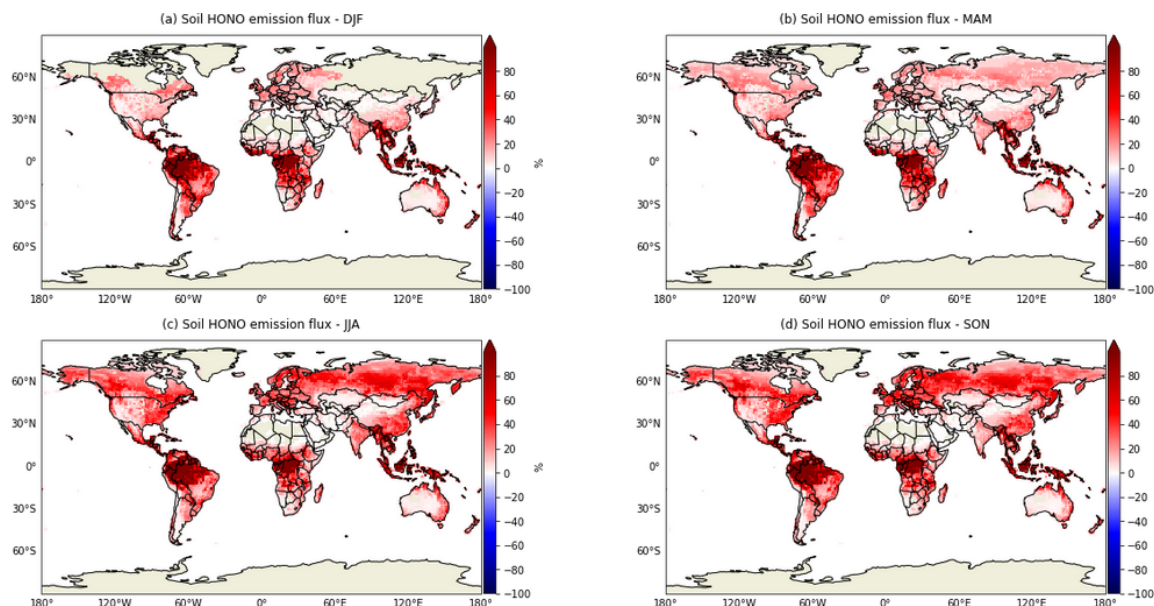
Figure 26: Relative difference Canopy Reduction soil HONO

3.6.4. Projections of soil NO and variability in different climates

The future land use is predicted to change as a consequence of the growing demand for nutrition and biofuels which implies an increasing use of fertilizer. Consequently, NO soil emissions are estimated to rise by ~28% during the century to 11.5 TgN/yr at the end of 2100 (Fowler et al., 2015). Similarly, Liu et al. (2021) estimate an increasing soil NO emission of 8.9 TgN/yr by the year 2050 due to intensive nitrification processes.

An increase of LAI by 10 %, in contrast, would lead to 1% lower emissions. In addition, several responses are expected from the changing climate. In fact, the 1°C higher temperature would cause ~5% increase in emissions (Weng et al., 2020). Following the future ('medium high') climate scenario RCP6.0 (Representative Concentration Pathway, 6 W/m2 radiative forcing until 2500, stabilization after 2150) used for the CMIP5 (Climate Model Intercomparison Project) simulations. Jöckel et al. (2016) suggest an increase of ~15 % in soil NO emissions due to increasing soil temperature (an increase of soil microbes) from present-day (2010) until 2100. However, the most significant implications for large-scale denitrification activity are changing rainfall and the regional hydrological cycles (Fowler et al., 2015). In general, soil NO_x will play a more important role in the global budget in the troposphere due to the decreasing anthropogenic emissions in the future. Therefore, increasing NOx-soil emissions may slow down the decrease of O3 in response to declining anthropogenic emissions (Wu et al. 2022).

3.6.5. Next steps with biogeochemical models implemented in ESMs

Uncertainties of modeling soil nitrogen emissions are associated with the model input and parameters (Wang and Chen 2012). Process-based biogeochemical models which also consider the complexity of soil emission processes as DNDC (Denitrification–Decomposition) are needed (Li et al., 2011). The capability to represent interactive biogeochemical cycles allows for instance for the online calculation of crop nutrition from soil. Also, a model like CLM5 distinguishes between natural and agricultural soils which more accurately predicts the fertilizer

1165 usage (Fung et al., 2022). Resolving the soil and litter biogeochemical dynamics vertically, in
1166 addition, lead to a more efficient retainment and recycling of N by the ecosystem (Koven et al.,
1167 2013). However, these models should be calibrated to multiple sites (Wang et al., 2019) which is
1168 limited by the availability of measurement data, especially when it comes to global modeling.

1169

1170 **4. Conclusion**

1171 In this article, we investigate temporal and spatial trends and variability of tropospheric ozone in
1172 relation to its precursors using satellite products, ozonesonde measurements, and model
1173 simulations. Our results show that ozone has positive trends at all latitudes and column depths
1174 regardless of the tropopause height within ±100 hPa. The positive trends in the 30-60ºN band are
1175 due to increasing trends over Canada and Alaska and are slightly offset by the small negative
1176 trends over the northeastern US and Europe. The lower trends in the bands 30-60ºN and 30-60ºS
1177 are due to the offsetting impact of negative trends over Eastern US and Europe in the north, and
1178 Australia and South Africa in the south, respectively. The decreasing trends of TrC-O_3 over parts
1179 of the northeastern US and Europe are likely due to the decreasing trend of TrC-NO_2, which is
1180 due to the effective measures applied over the last two decades to mitigate air pollution in these
1181 regions. TrC-HCHO trends are decreasing in the Eastern US, some parts of northern and western
1182 Africa, and western and northern Europe, and increasing in South Asia, central Africa, northern
1183 Australia, and Brazil. TrC-HCHO trends are consistent with that of TrC-O_3 over northeastern US
1184 and Europe. Simulated O_3 and its precursors are in good agreement with satellite measurements.
1185 Considering different latitude bands, the TrC-O_3 highest trends are simulated between 30º S and
1186 60º N, consistent with calculated trends based on satellite observations. The middle and upper
1187 troposphere make the largest contributions to the simulated TrC-O_3 trend globally, with large
1188 contributions from the upper troposphere driving the simulated TrC-O_3 trend at 30°S-30°N and
1189 counteracting the negative TrC-O_3 trend in the southern midlatitudes.

1190 We have also shed light on NO_X lightning and its relation to ozone trends. LNO_x is responsible
1191 for the largest fraction of upper tropospheric ozone in the tropics year-round and in the mid-
1192 latitudes in summer. Ozone Radiative forcing is due to the ozone near the tropopause. An
1193 increasing trend of LNO_x at Arctic latitudes has been noted, as that region rapidly warms.
1194 However, future trends in flash rate are uncertain, with conflicting predictions coming from
1195 models with differing flash rate parameterizations. Soil HONO emissions had their highest
1196 positive monthly anomalies mainly in the 5 most recent years which is likely due to the more
1197 frequent heat wave occurrence, e.g. in Europe and North America. Soil HONO trends are highest
1198 in Africa accounting for ~30% of the global anomaly. Soil NO_x emissions could play an
1199 important role in the tropospheric NO_x global budget due to the decreasing anthropogenic
1200 emissions in the future. Therefore, the expected increase in NO_x-soil emissions may slow down
1201 the decrease of O_3 in response to declining anthropogenic emissions. Overall, this study
1202 presented a comprehensive overview of tropospheric ozone trends in relation to its precursors in
1203 different spatial and temporal scales.

1204 Competing interests: At least one of the (co-)authors is a member of the editorial board of
1205 Atmospheric Chemistry and Physics

1217

5.   References

1219   Allen, D., Pickering, K., Duncan, B., and Damon, M. (2010), Impact of lightning NO
1220   emissions on North American photochemistry as determined using the Global
1221   Modeling Initiative (GMI) model, *J. Geophys. Res*.,115, D22301,
1222   doi:10.1029/2010JD014062.

1223   Allen, D. J., Pickering, K. E., Pinder, R. W., Henderson, B. H., Appel, K. W., and Prados, A.
1224   (2012), Impact of lightning-NO on eastern United States photochemistry during the
1225   summer of 2006 as determined using the CMAQ model, *Atmos. Chem.
1226   Phys*., 12, 1737-1758, doi:10.5194/acp-12-1737-2012.

1227   Allen, D. J., Pickering, K. E., Bucsela, E., van Geffen, J., Lapierre, J., Koshak, W., & Eskes,
1228   H. (2021b). Observations of Lightning NOx production from Tropospheric Ozone
1229   Monitoring Instrument Case Studies over the United States, *J. Geophys. Res*., 126
1230   (10), https://doi.org/10.1029/2020JD034174.

1231   Allen, D. J., Pickering, K. E., Lamsal, L., Mach, D., Quick, M. G., Lapierre, J., Janz, S.,
1232   Koshak, W., Kowalewski, M. & Blakeslee, R. (2021a), Observations of Lightning
1233 NO_x production from GOES-R Post Launch Test Field Campaign Flights, *J. Geophys.
1234   Res.*, 126 (8), https://doi.org/10.1029/2020JD033769.

1235   Allen, D., J., Pickering, K. E., Bucsela, E., Krotkov, N., and Holzworth, R. (2019), Lightning
1236 NO_x Production in the Tropics as Determined Using OMI NO_2 Retrievals and
1237   WWLLN Stroke Data, J. Geophys. Res., https://doi.org/10.1029/2018JD029824.

1238   Apel, E. C., J. R. Olson, J. H. Crawford, R. S. Hornbrook, A. J. Hills, C. A. Cantrell, L. K.
1239   Emmons, D. J. Knapp, S. Hall, R. L. Mauldin III, A. J. Weinheimer, A. Fried, D. R.
1240   Blake, J. D. Crounse, J. M. St. Clair, P. O. Wennberg, G. S. Diskin, H. E. Fuelberg,
1241   A. Wisthaler, T. Mikoviny, W. Brune, and D. D. Riemer, (2012) Impact of the deep
1242   convection of isoprene and other reactive trace species on radicals and ozone in the
1243   upper troposphere, *Atmos. Chem. Phys*., 12, 1135–1150, www.atmos-chem-
1244   phys.net/12/1135/2012/doi:10.5194/acp-12-1135-2012.

1245   Apel, E. C., et al. (2015), Upper tropospheric ozone production from lightning NOx-
1246   impacted convection: Smoke ingestion case study from the DC3 campaign, *J.
1247   Geophys. Res. Atmos*., 120, doi:10.1002/2014JD022121.

1248   Archibald, A.T., et al. 2020.Tropospheric Ozone Assessment Report: A critical review of
1249   changes in the tropospheric ozone burden and budget from 1850 to 2100. Elem Sci
1250   Anth, 8: 1. DOI: https://doi.org/10.1525/elementa.2020.034, 2020.

ASDC, MOPITT CO gridded monthly means (Near and Thermal Infrared Radiances) V009 [Data set]. NASA Langley Atmospheric Science Data Center DAAC. Retrieved from https://doi.org/10.5067/TERRA/MOPITT/MOP03JM.009, 2024.

Barret, B., De Mazière, M., and Mahieu, E.: Ground-based FTIR measurements of CO from the Jungfraujoch: characterisation and comparison with in situ surface and MOPITT data, Atmos. Chem. Phys., 3, 2217–2223, https://doi.org/10.5194/acp-3-2217-2003, 2003.

Bauwens, M.; Compernolle, S.; Stavrakou, T.; Müller, J.; Gent, J.; Eskes, H.; Levelt, P.F.; van der A, R.; Veefkind, J.P.; Vlietinck, J.; et al. Impact of Coronavirus Outbreak on NO2 Pollution Assessed Using TROPOMI and OMI Observations. Geophys. Res. Lett. 2020, 47.

Beirle, S., H. Huntrieser, and T Wagner (2010), Direct satellite observation of lightning-produced NOx, *Atmos. Chem. Phys.*, 10(22), 10965-10986, doi:10.5194/acp-10-10965.

Boersma, K., Eskes, H., Richter, A., De Smedt, I., Lorente, A., Beirle, S., Van Geffen, J., Peters, E., Van Roozendael, M., and Wagner, T.: QA4ECV NO$_2$ tropospheric and stratospheric vertical column data from OMI (Version 1.1) (data set), Royal Netherlands Meteorological Institute (KNMI), https://doi.org/10.21944/qa4ecv-no2-omi-v1.1, 2017a.

Boersma, K., Eskes, H., Richter, A., De Smedt, I., Lorente, A., Beirle, S., Van Geffen, J., Peters, E., Van Roozendael, M., and Wagner, T.: QA4ECV NO$_2$ tropospheric and stratospheric vertical column data from GOME-2 (Version 1.1) (data set), Royal Netherlands Meteorological Institute (KNMI), https://doi.org/10.21944/qa4ecv-no2-gome2a-v1.1, 2017b.

Boersma, K., Eskes, H., Richter, A., De Smedt, I., Lorente, A., Beirle, S., Van Geffen, J., Peters, E., Van Roozendael, M., and Wagner, T.: QA4ECV NO$_2$ tropospheric and stratospheric vertical column data from SCIAMACHY (Version 1.1) (data set), Royal Netherlands Meteorological Institute (KNMI), https://doi.org/10.21944/qa4ecv-no2-scia-v1.1, 2017c.

Boersma, K. F., Eskes, H. J., Richter, A., De Smedt, I., Lorente, A., Beirle, S., van Geffen, J. H. G. M., Zara, M., Peters, E., Van Roozendael, M., Wagner, T., Maasakkers, J. D., van der A, R. J., Nightingale, J., De Rudder, A., Irie, H., Pinardi, G., Lambert, J.-C., and Compernolle, S. C.: Improving algorithms and uncertainty estimates for satellite NO2 retrievals: results from the quality assurance for the essential climate variables (QA4ECV) project, Atmos. Meas. Tech., 11, 6651–6678, https://doi.org/10.5194/amt-11-6651-2018, 2018.

Brune, W. H., et al. (2018) Atmospheric oxidation in the presence of clouds during the Deep

Convective Clouds and Chemistry (DC3) study, Atmos. Chem. Phys., 18, 14493–14510, 2018, https://doi.org/10.5194/acp-18-14493-2018.

Bruning, E. C. & Thomas, R. J. (2015), Lightning channel length and flash energy determined from moments of the flash area distribution, *J. Geophys. Res. Atmos.*, 120, 8925–8940, doi:10.1002/2015JD023766

Buchholz, R.R.; Deeter, M.N.;Worden, H.M.; Gille, J.; Edwards, D.P.; Hannigan, J.W.; Jones, N.B.; Paton-Walsh, C.; Griffith, D.W.T.; Smale, D.; et al. Validation of MOPITT carbon monoxide using ground-based Fourier transform infrared spectrometer data from NDACC. Atmos. Meas. Tech. 2017, 10, 1927–1956.

Buchholz, R. R., Worden, H. M., Park, M., Francis, G., Deeter, M. N., Edwards, D. P., Emmons, L. K., Gaubert, B., Gille, J., Martinez-Alonso, S., Tang, W., Kumar, R., Drummond, J. R., Clerbaux, C., George, M., Coheur, P.-F., Hurtmans, D., Bowman, K. W., Luo, M., Payne, V. H., Worden, J. R., Chin, M., Levy, R. C., Warner, J., Wei, Z., and Kulawik, S. S.: Air pollution trends measured from Terra: CO and AOD over industrial, fire-prone, and background regions, Remote Sens. Environ., 256, 112275, https://doi.org/10.1016/j.rse.2020.112275, 2021.

Bucsela, E. J., K. E. Pickering, T. L. Huntemann, R. C. Cohen, A. Perring, J. F. Gleason, R. J. Blakeslee, R. I. Albrecht, R. Holzworth, J. P. Cipriani, D. Vargas-Navarro, I. Mora-Segura, A. Pacheco-Hernández, S. Laporte-Molina, (2010) Lightning-generated NO_x seen by OMI during NASA's TC^4 experiment, *J. Geophys. Res.*, 115, D00J10, doi:10.1029/2009JD013118.

Bucsela, E., Pickering, K. E., Allen, D., Holzworth, R., and Krotkov, N. (2019), Midlatitude lightning NO_x Production Efficiency Inferred from OMI and WWLLN Data, *J. Geophys. Res.*, https://doi.org/10.1029/2019JD030561.

Canadell, J.G., P.M.S. Monteiro, M.H. Costa, L. Cotrim da Cunha, P.M. Cox, A.V. Eliseev, S. Henson, M. Ishii, S. Jaccard, C. Koven, A. Lohila, P.K. Patra, S. Piao, J. Rogelj, S. Syampungani, S. Zaehle, and K. Zickfeld: Global Carbon and other Biogeochemical Cycles and Feedbacks. In Climate Change 2021: The Physical Science Basis. Contribution of Working Group I to the Sixth Assessment Report of the Intergovernmental Panel on Climate Change [Masson-Delmotte, V., P. Zhai, A. Pirani, S.L. Connors, C. Péan, S. Berger, N. Caud, Y. Chen, L. Goldfarb, M.I. Gomis, M. Huang, K. Leitzell, E. Lonnoy, J.B.R. Matthews, T.K. Maycock, T. Waterfield, O. Yelekçi, R. Yu, and B. Zhou (eds.)]. Cambridge University Press, Cambridge, United Kingdom and New York, NY, USA, pp. 673–816, doi: 10.1017/9781009157896.007, 2021.

Cazorla, M. and Herrera, E.: An ozonesonde evaluation of spaceborne observations in the Andean tropics, Sci Rep, 12, https://doi.org/10.1038/s41598-022-20303-7, 2022.

Chang K-L, Petropavlovskikh I, Cooper OR, Schultz MG, Wang T. Regional trend analysis of surface ozone observations from monitoring networks in eastern North America, Europe and East Asia. Elem Sci Anth., 5:50. DOI: 10.1525/elementa.243, 2017.

Chang, K.-L., Cooper, O. R., Gaudel, A., Petropavlovskikh, I., and Thouret, V.: Statistical regularization for trend detection: an integrated approach for detecting long-term trends from sparse tropospheric ozone profiles, Atmos. Chem. Phys., 20, 9915–9938, https://doi.org/10.5194/acp-20-9915-2020, 2020.

Chang, K.-L., Cooper, O. R., Gaudel, A., Allaart, M., Ancellet, G., Clark, H., et al. (2022). Impact of the COVID-19 economic downturn on tropospheric ozone trends: An uncertainty weighted data synthesis for quantifying regional anomalies above western North America and Europe. *AGU Advances*, 3, e2021AV000542. https://doi.org/10.1029/2021AV000542, 2022.

Chang K-L, Martin G. Schultz, Gerbrand Koren, Niklas Selke, Guidance note on best statistical practices for TOAR analyses, https://doi.org/10.48550/arXiv.2304.14236, 2023.

Chang, K.-L., Cooper, O. R., Gaudel, A., Petropavlovskikh, I., Effertz, P., Morris, G., and McDonald, B. C.: Technical note: Challenges of detecting free tropospheric ozone trends in a sparsely sampled environment, EGUsphere [preprint], https://doi.org/10.5194/egusphere-2023-2739, 2024.

Chen, Z., Jane Liu, Xiushu Qie, Xugeng Cheng, Mengmiao Yang, Lei Shu, Zhou Zang, Stratospheric influence on surface ozone pollution in China, Nature Communications, 10.1038/s41467-024-48406-x, **15**, 1, 2024.

Christiansen, A., Mickley, L. J., Liu, J., Oman, L. D., and Hu, L.: Multidecadal increases in global tropospheric ozone derived from ozonesonde and surface site observations: can models reproduce ozone trends?, Atmos Chem Phys, 22, 14751–14782, https://doi.org/10.5194/acp-22-14751-2022, 2022.

Cooper, O. R., Schultz, M. G., Schröder, S., Chang, K. L., Gaudel, A., Benítez, G. C., Cuevas, E., Fröhlich, M., Galbally, I. E., Molloy, S., Kubistin, D., Lu, X., McClure-Begley, A., Nédélec, P., O'Brien, J., Oltmans, S. J., Petropavlovskikh, I., Ries, L., Senik, I., Sjöberg, K., Solberg, S., Spain, G. T., Spangl, W., Steinbacher, M., Tarasick, D., Thouret, V., and Xu, X.: Multi-decadal surface ozone trends at globally distributed remote locations, Elementa, 8, https://doi.org/10.1525/elementa.420, 2020.

Cummings, K. A., T. L. Huntemann, and K. E. Pickering (2013), Cloud-resolving chemistry simulation of a Hector thunderstorm, *Atmos. Chem. Phys*., 13(5), 2757-2777, doi:10.5194/acp-13-2757.

DeCaria, A., K. Pickering, G. Stenchikov, J. Scala, J. Stith, J. Dye, B. Ridley, and P. Laroche, A cloud-scale model study of lightning-generated NO_x in an individual thunderstorm during STERAO-A, *J. Geophys. Res*., 105, 11,601-11,616, 2000.

DeCaria, A. J., K. E. Pickering, G. L. Stenchikov, and L. E. Ott (2005), Lightning-generated NOx and its impact on tropospheric ozone production: A three-dimensional modeling study of a STERAO-A thunderstorm, *J. Geophys. Res*., *110*, D14303, doi:10.1029/2004JD005556. Deeter, M., Francis, G., Gille, J., Mao, D., Martínez-Alonso, S., Worden, H., Ziskin, D., Drummond, J., Commane, R., Diskin, G., and McKain, K.: The MOPITT Version 9 CO product: sampling enhancements and validation, Atmos. Meas. Tech., 15, 2325–2344, https://doi.org/10.5194/amt-15-2325-2022, 2022.

De Smedt, I., Theys, N., Yu, H., Danckaert, T., Lerot, C., Compernolle, S., Van Roozendael, M., Richter, A., Hilboll, A., Peters, E., Pedergnana, M., Loyola, D., Beirle, S., Wagner, T., Eskes, H., van Geffen, J., Boersma, K. F., and Veefkind, P.: Algorithm theoretical baseline for formaldehyde retrievals from S5P TROPOMI and from the QA4ECV project, Atmos. Meas. Tech., 11, 2395–2426, https://doi.org/10.5194/amt-11-2395-2018, 2018 Fadnavis, S., Sagalgile, A., Sonbawne, S., Vogel, B., Peter, T., Wienhold, F. G., Dirksen, R., Oelsner, P., Naja, M., and Müller, R.: Comparison of ozonesonde measurements in the upper troposphere and lower Stratosphere in Northern India with reanalysis and chemistry-climate-model data, Sci Rep, 13, 7133, https://doi.org/10.1038/s41598-023-34330-5, 2023.

Duncan, B. N., Strahan, S. E., Yoshida, Y., Steenrod, S. D., and Livesey, N.: Model study of the cross-tropopause transport of biomass burning pollution, Atmos. Chem. Phys., 7, 3713–3736, https://doi.org/10.5194/acp-7-3713-2007, 2007.

Elguindi, N., Granier, C., Stavrakou, T., Darras, S., Bauwens, M., Cao, H., Chen, C., Denier van der Gon, H. A. C., Dubovik, O., Fu, T. M., Henze, D. K., Jiang, Z., Keita, S., Kuenen, J. J. P., Kurokawa, J., Liousse, C., Miyazaki, K., Müller, J. F., Qu, Z., Solmon, F., and Zheng, B.: Intercomparison of Magnitudes and Trends in Anthropogenic Surface Emissions From Bottom-Up Inventories, Top-Down Estimates, and Emission Scenarios, Earths Future, 8, e2020EF001520, https://doi.org/10.1029/2020EF001520, 2020.

Elshorbany, Y. F., Kurtenbach, R., Wiesen, P. Lissi, E., Rubio, M., Villena, G., Gramsch, E., Rickard, A. R., Pilling, M. J., Kleffmann. J.: Oxidation capacity of the city air of Santiago, Chile, *Atmospheric Chemistry and Physics*, **9**, 2257-2273, 2009.

Elshorbany, Y. F, Barnes, I., Becker, K. H, Kleffmann, J., and Wiesen, P.: Sources and Cycling of Tropospheric Hydroxyl Radicals-An Overview, *Zeitschrift für Physikalische Chemie*, 224, 967-987, DOI:10.1524/zpch.2010.6136, 2010.

Elshorbany, Y. F., Kleffmann, J., Hofzumahaus, A., Kurtenbach, R., Wiesen, P., Dorn,H.-P., Schlosser, E., Brauers, T., Fuchs, H., Rohrer, F., Wahner, A., Kanaya, Y., Yoshino, A., Nishida, S., Kajii, Y., Martinez, M., Rudolf, M., Harder, H., Lelieveld, J., , Elste, T., Plass-Dülmer, C., Stange, G., and Berresheim, H.: HO_x Budgets during HOxComp: a Case Study of HO_x Chemistry under NO_x limited Conditions, J. Geophys. Res., 117, D03307, doi: 10.1029/2011JD017008, 2012.

Elshorbany, Y. F., Crutzen, P. J., Steil, B., Pozzer, A., Tost, H., and Lelieveld, J.: Global and regional impacts of HONO on the chemical composition of clouds and aerosols, Atmos. Chem. Phys., 14, 1167–1184, https://doi.org/10.5194/acp-14-1167-2014, 2014.

Elshorbany, Y. F.; Hannah C. Kapper; Jerald R. Ziemke;Scott A. Parr; (2021). The Status of Air Quality in the United States During the COVID-19 Pandemic: A Remote Sensing Perspective . Remote Sensing, doi:10.3390/rs13030369, 2021.

Fadnavis et al., 2024, in preparation.

Fehr, T., H. Höller, and H. Huntrieser (2004), Model study on production and transport of lightning-produced NOx in a EULINOX supercell storm, *J. Geophys. Res.*, *109*, D09102, doi:10.1029/2003JD003935.

Finney. D. L., R. M. Doherty, O. Wild, H. Huntrieser, H. C. Pumphrey, and A. M. Blyth (2014), Using cloud ice flux to parameterize large-scale lightning, *Atmos. Chem. Phys*., 14, 12665–12682, www.atmos-chem-phys.net/14/12665/2014/ doi:10.5194/acp-14-12665-2014.

Finney, D. L., R. M. Doherty, O. Wild, P. J. Young, and A. Butler (2016), Response of lightning NO*x* emissions and ozone production to climate change: Insights from the Atmospheric Chemistry and Climate Model Intercomparison Project, *Geophys. Res. Lett*., 43, 5492–5500, doi:10.1002/2016GL068825.

Finney, D. L., R. M. Doherty, O. Wild, D. S. Stevenson, I. A. MacKenzie, and A. M. Blyth (2018), A projected decrease in lightning under climate change, *Nature Climate Change*, 8, 210-213.

Fiore, A. M., Jacob, D. J., Field, B. D., Streets, D. G., Fernandes, S. D., and Jang, C.: Linking air pollution and climate change: The case for controlling methane, Geophys. Res. Lett., 29, 1919, doi:10.1029/2002GL015601, 2002.

Fiore, A. M., L. W. Horowitz, E. J. Dlugokencky, and J. J. West (2006), Impact of meteorology and emissions on methane trends, 1990–2004, *Geophys. Res. Lett.*, 33, L12809, doi:10.1029/2006GL026199.

Fisher, B. L., Lamsal, L. N., Fasnacht, Z., Oman, L. D., Joiner, J., Krotkov, N. A., ... & Yang, E. S.: Revised estimates of NO2 reductions during the COVID-19 lockdowns using updated TROPOMI NO2 retrievals and model simulations. Atmospheric Environment, 326, 120459, 2024.

Fleming, Z.L., Doherty, R.M., von Schneidemesser, E., Malley, C.S., Cooper, O.R., Pinto, J.P., Colette, A., Xu, X., Simpson, D., Schultz, M.G., Lefohn, A.S., Hamad, S., Moolla, R., Solberg, S. and Feng, Z., Tropospheric Ozone Assessment Report: Present-day ozone distribution and trends relevant to human health. 2018. Elem Sci Anth, 6(1), p.12. DOI: 10.1525/elementa.73.

Flynn, C. M., K. E. Pickering, J. H. Crawford, A. Weinheimer, K. L. Thornhill, C. Loughner, P. Lee, Variability of O_3 and NO_2 profile shapes during DISCOVER-AQ: Implications for satellite observations and comparisons to model-simulated profiles, *Atmos. Environ.*, 147, 133-156, 2016.

Fortems-Cheiney, A., Chevallier, F., Pison, I., Bousquet, P., Szopa, S., Deeter, M. N., and Clerbaux, C.: Ten years of CO emissions as seen from Measurements of Pollution in the Troposphere (MOPITT), J. Geophys. Res., 116, D05304, https://doi.org/10.1029/2010JD014416, 2011.

Fortems-Cheiney, A., Chevallier, F., Pison, I., Bousquet, P., Saunois, M., Szopa, S., Cressot, C., Kurosu, T. P., Chance, K., and Fried, A.: The formaldehyde budget as seen by a global-scale multi-constraint and multi-species inversion system, Atmos. Chem. Phys., 12, 6699–6721, https://doi.org/10.5194/acp-12-6699-2012, 2012.

Forster, P., T. Storelvmo, K. Armour, W. Collins, J.-L. Dufresne, D. Frame, D.J. Lunt, T. Mauritsen, M.D. Palmer, M. Watanabe, M. Wild, and H. Zhang, 2021: The Earth's Energy Budget, Climate Feedbacks, and Climate Sensitivity. In Climate Change 2021: The Physical Science Basis. Contribution of Working Group I to the Sixth Assessment Report of the Intergovernmental Panel on Climate Change [Masson-Delmotte, V., P. Zhai, A. Pirani, S.L. Connors, C. Péan, S. Berger, N. Caud, Y. Chen, L. Goldfarb, M.I. Gomis, M. Huang, K. Leitzell, E. Lonnoy, J.B.R. Matthews, T.K. Maycock, T. Waterfield, O. Yelekçi, R. Yu, and B. Zhou (eds.)]. Cambridge University Press, 923 Cambridge, United Kingdom and New York, NY, USA, pp. 923–1054, doi:10.1017/9781009157896.009, 2021.

Fullekrug, M. E. Williams, C. Price, S. Goodman, R. Holzworth, K. Virts, and D. Buechler (2022) Sidebar 2.1: Lightning, in State of the Climate: 2021, *Bull. Amer. Meteor. Soc.*, 108, S79-S81, doi:10.1175/BAMS-D-22-0092.1

Fung, K. M., Val Martin, M., and Tai, A. P. K.: Modeling the interinfluence of fertilizer-induced NH3 emission, nitrogen deposition, and aerosol radiative effects using modified CESM2, Biogeosciences, 19, 1635–1655, https://doi.org/10.5194/bg-19-1635-2022, 2022.

Gaubert, B., Emmons, L. K., Raeder, K., Tilmes, S., Miyazaki, K., Arellano Jr., A. F., Elguindi, N., Granier, C., Tang, W., Barré, J., Worden, H. M., Buchholz, R. R., Edwards, D. P., Franke, P., Anderson, J. L., Saunois, M., Schroeder, J., Woo, J.-H., Simpson, I. J., Blake, D. R., Meinardi, S., Wennberg, P. O., Crounse, J., Teng, A., Kim, M., Dickerson, R. R., He, H., Ren, X., Pusede, S. E., and Diskin, G. S.: Correcting model biases of CO in East Asia: impact on oxidant distributions during KORUS-AQ, Atmos. Chem. Phys., 20, 14617–14647, https://doi.org/10.5194/acp-20-14617-2020, 2020.

Gaudel, A., Cooper, O.R., Ancellet, G., Barret, B., Boynard, A., Burrows, J.P., Clerbaux, C., Coheur, P.-F., Cuesta, J., Cuevas, E., Doniki, S., Dufour, G., Ebojie, F., Foret, G., Garcia, O., Granados Muños, M.J., Hannigan, J.W., Hase, F., Huang, G., Hassler, B., Hurtmans, D., Jaffe, D., Jones, N., Kalabokas, P., Kerridge, B., Kulawik, S.S., Latter, B., Leblanc, T., Le Flochmoën, E., Lin, W., Liu, J., Liu, X., Mahieu, E., McClure-Begley, A., Neu, J.L., Osman, M., Palm, M., Petetin, H., Petropavlovskikh, I., Querel, R., Rahpoe, N., Rozanov, A., Schultz, M.G., Schwab, J., Siddans, R., Smale, D., Steinbacher, M., Tanimoto, H., Tarasick, D.W., Thouret, V., Thompson, A.M., Trickl, T., Weatherhead, E., Wespes, C., Worden, H.M., Vigouroux, C., Xu, X., Zeng, G. and Ziemke, J., Tropospheric Ozone Assessment Report: Present-day distribution and trends of tropospheric ozone relevant to climate and global atmospheric chemistry model evaluation, Elem Sci Anth, 6(1), p.39. DOI: 10.1525/elementa.291, 2018.

Gelaro, Ronald, et al. "The modern-era retrospective analysis for research and applications, version 2 (MERRA-2)." *Journal of climate* 30.14 (2017): 5419-5454.

Ghude, S.D., Van der A, R.J., Beig, G., Fadnavis, S., Polade, S.D.: Satellite derived trends in NO2 over the major global hotspot regions during the past decade and their inter-comparison. Environ. Pollut. 157, 1873–1878. https://doi.org/10.1016/j.envpol.2009.01.013, 2009.

Glotfelty, T., Zhang, Y., Karamchandani, P., and Streets, D. G.: Will the role of intercontinental transport change in a changing climate?, Atmos. Chem. Phys., 14, 9379–9402, https://doi.org/10.5194/acp-14-9379-2014, 2014.

Gödde and Conrad: https://doi.org/10.1007/s003740000247

Granier, C., Bessagnet, B., Bond, T., D'Angiola, A., Denier van der Gon, H., Frost, G. J., ... & van Vuuren, D. P.: Evolution of anthropogenic and biomass burning emissions of air pollutants at global and regional scales during the 1980–2010 period. *Climatic change*, *109*, 163-190, 2011.

Grewe, V., Brunner, D., Dameris, M., Grenfell, J. L., Hein, R., Shindell, D., & Staehelin, J. (2001), Origin and variability of upper tropospheric nitrogen oxides and ozone at northern mid-latitudes, *Atmos. Env.*, 35, 3421-3433.

Griffiths, P. T., Murray, L. T., Zeng, G., Shin, Y. M., Abraham, N. L., Archibald, A. T., Deushi, M., Emmons, L. K., Galbally, I. E., Hassler, B., Horowitz, L. W., Keeble, J., Liu, J., Moeini, O., Naik, V., O'Connor, F. M., Oshima, N., Tarasick, D., Tilmes, S.,

1509 Turnock, S. T., Wild, O., Young, P. J., and Zanis, P.: Tropospheric ozone in CMIP6
1510 simulations, Atmos. Chem. Phys., 21, 4187–4218, https://doi.org/10.5194/acp-21-
1511 4187-2021, 2021.

1512 Gulev, S.K., P.W. Thorne, J. Ahn, F.J. Dentener, C.M. Domingues, S. Gerland, D. Gong,
1513 D.S. Kaufman, H.C. Nnamchi, J. Quaas, J.A. Rivera, S. Sathyendranath, S.L. Smith,
1514 B. Trewin, K. von Schuckmann, and R.S. Vose: Changing State of the Climate
1515 System. In Climate Change 2021: The Physical Science Basis. Contribution of
1516 Working Group I to the Sixth Assessment Report of the Intergovernmental Panel on
1517 Climate Change [Masson-Delmotte, V., P. Zhai, A. Pirani, S.L. Connors, C. Péan, S.
1518 Berger, N. Caud, Y. Chen, L. Goldfarb, M.I. Gomis, M. Huang, K. Leitzell, E.
1519 Lonnoy, J.B.R. Matthews, T.K. Maycock, T. Waterfield, O. Yelekçi, R. Yu, and B.
1520 Zhou (eds.)]. Cambridge University Press, Cambridge, United Kingdom and New
1521 York, NY, USA, pp. 287–422, doi: 10.1017/9781009157896.004, 2021.

1522 Hoor, P., Borken-Kleefeld, J., Caro, D., Dessens, O., Endresen, O., Gauss, M., Grewe, V.,
1523 Hauglustaine, D., Isaksen, I. S. A., Jöckel, P., Lelieveld, J., Myhre, G., Meijer, E.,
1524 Olivie, D., Prather, M., Schnadt Poberaj, C., Shine, K. P., Staehelin, J., Tang, Q., van
1525 Aardenne, J., van Velthoven, P., and Sausen, R.: The impact of traffic emissions on
1526 atmospheric ozone and OH: results from QUANTIFY, Atmos. Chem. Phys., 9, 3113–
1527 3136, https://doi.org/10.5194/acp-9-3113-2009, 2009.

1528 Holzworth, R. H., Brundell, J. B., McCarthy, M. P., Jacobson, A. R., Rodger, C. J., &
1529 Anderson, T. S. (2021). Lightning in the Arctic. *Geophysical Research Letters*, 48,
1530 e2020GL091366.
1531 https://doi.org/10.1029/2020GL091366.

1532 Hov, Ö., Hesstvedt, E. & Isaksen, I. Long-range transport of tropospheric ozone. *Nature* **273**,
1533 341–344. https://doi.org/10.1038/273341a0, 1978.

1534 Hubert, D., Heue, K.-P., Lambert, J.-C., Verhoelst, T., Allaart, M., Compernolle, S., Cullis,
1535 P. D., Dehn, A., Félix, C., Johnson, B. J., Keppens, A., Kollonige, D. E., Lerot, C.,
1536 Loyola, D., Maata, M., Mitro, S., Mohamad, M., Piters, A., Romahn, F., Selkirk, H.
1537 B., da Silva, F. R., Stauffer, R. M., Thompson, A. M., Veefkind, J. P., Vömel, H.,
1538 Witte, J. C., and Zehner, C.: TROPOMI tropospheric ozone column data: geophysical
1539 assessment and comparison to ozonesondes, GOME-2B and OMI, Atmos Meas Tech,
1540 14, 7405–7433, https://doi.org/10.5194/amt-14-7405-2021, 2021.

1541 Hudman et al., (2012) www.atmos-chem-phys.net/12/7779/2012/

1542 Huntrieser, H., U. Schumann, H. Schlager, H. Höller, A. Giez, H.-D. Betz, D. Brunner, C.
1543 Forster, O. Pinto Jr., and R. Calheiros (2008), Lightning activity in Brazilian
1544 thunderstorms during TROCCINOX: Implications for NOx production, *Atmos. Chem.*
1545 *Phys.*, *8*, 21–953.

1546 Huntrieser, H., H. Schlager, M. Lichtenstern, P. Stock, T. Hamburger, H. Hoeller, K.
1547 Schmidt, H.-D. Betz, A. Ulanovsky, and F. Ravegnani (2011) Mesoscale convective
1548 systems observed during AMMA and their impact on the NOx and O3 budget over
1549 West Africa, Atmos. Chem. Phys., 11, 2503–2536, www.atmos-chem-
1550 phys.net/11/2503/2011, doi:10.5194/acp-11-2503-2011

Ichoku, C., & Ellison, L.: Global top-down smoke-aerosol emissions estimation using satellite fire radiative power measurements. *Atmospheric Chemistry and Physics*, *14*(13), 6643-6667, 2014.

IPCC, AR5, chrome-extension://efaidnbmnnnibpcajpcglclefindmkaj/https://www.ipcc.ch/site/assets/uploads/2018/03/TAR-06.pdf, 2018.

Isaksen, I.S.A.; Berntsen, T.K.; Dalsøren, S.B.; Eleftheratos, K.; Orsolini, Y.; Rognerud, B.; Stordal, F.; Søvde, O.A.; Zerefos, C.; Holmes, C.D. Atmospheric Ozone and Methane in a Changing Climate. Atmosphere, 5, 518-535. https://doi.org/10.3390/atmos5030518, 2014.

Itahashi, S., Mathur, R., Hogrefe, C., Napelenok, S. L., and Zhang, Y.: Modeling stratospheric intrusion and trans-Pacific transport on tropospheric ozone using hemispheric CMAQ during April 2010 – Part 2: Examination of emission impacts based on the higher-order decoupled direct method, Atmos. Chem. Phys., 20, 3397–3413, https://doi.org/10.5194/acp-20-3397-2020, 2020.

Janssens-Maenhout, G., Pagliari, V., Guizzardi, D., & Muntean, M.: Global emission inventories in the emission database for global atmospheric research (EDGAR)– Manual (I*). Gridding: EDGAR emissions distribution on global gridmaps, Publications Office of the European Union, Luxembourg, 775, 2013.*

Jin, X., Fiore, A., Boersma, K. F., Smedt, I. D., and Valin, L.: Inferring Changes in Summertime Surface Ozone–NOx –VOC Chemistry over U.S. Urban Areas from Two Decades of Satellite and Ground-Based Observations, Environmental Science Technology, 54, 6518–6529, https://doi.org/10.1021/acs.est.9b07785, 2020

J. Jung, Y. Choi, S. Mousavinezhad, D. Kang, J. Park, A. Pouyaei, *et al.:* Changes in the ozone chemical regime over the contiguous United States inferred by the inversion of NOx and VOC emissions using satellite observation, Atmos. Res., 270, 106076, https://doi.org/10.1016/j.atmosres.2022.106076, 2022

Kang, D., K. Foley, R. Mathur, S. Roselle, K. Pickering, and D. Allen, Lightning NO_X Production in CMAQ Part II – Performance Evaluations, *Geosci. Model Devel.*, 12, 4409–4424, https://doi.org/10.5194/gmd-12-4409-2019, 2019.

Kaynak, B., Hu, Y., Martin, R. V., Russell, A. G., Choi, Y., & Wang, Y. (2008). The effect of lightning NOx production on surface ozone in the continental United States. Atmospheric Chemistry and Physics, 8, 5151–5159.

Koven et al., (2013) https://bg.copernicus.org/articles/10/7109/2013/

Kitagawa, N., (1989) Long-term variations in thunder-day frequencies in Japan. J. Geophys. Res., 94, 13 183–13 189, https://doi.org/10.1029/JD094iD11p13183.

Koehler, T. L. (2020) Cloud-to-Ground Lightning Flash Density and Thunderstorm Day Distributions over the Contiguous United States Derived from NLDN Measurements: 1993–2018, *Mon. Weather Rev.*, DOI: 10.1175/MWR-D-19-0211.1

Kopacz, M., Jacob, D. J., Fisher, J. A., Logan, J. A., Zhang, L., Megretskaia, I. A., Yantosca, R. M., Singh, K., Henze, D. K., Burrows, J. P., Buchwitz, M., Khlystova, I., McMillan, W. W., Gille, J. C., Edwards, D. P., Eldering, A., Thouret, V., and Nedelec, P.: Global estimates of CO sources with high resolution by adjoint inversion of multiple satellite

datasets (MOPITT, AIRS, SCIAMACHY, TES), Atmos. Chem. Phys., 10, 855–876, https://doi.org/10.5194/acp-10-855-2010, 2010.

Koshak, W., Peterson, H., Biazar, A., Khan, M., & Wang, L. (2014). The NASA Lightning Nitrogen Oxides Model (LNOM): application to air quality modeling. *Atmospheric Research*, *135*, 363-369.

Koshak, W.J., Cummins, K.L., Buechler, D.E., Vant-Hull, B., Blakeslee, R.J., Williams, E.R. and Peterson, H.S. (2015) Variability of CONUS lightning in 2003–12 and associated impacts. *Journal of Applied Meteorology and Climatology*, **54**, 15– 41, https://doi.org/10.1175/JAMC-D-14-0072.1.

Krizan, P. and Lastovicka, J.: Trends in positive and negative ozone laminae in the Northern Hemisphere, Journal of Geophysical Research: Atmospheres, 110, https://doi.org/https://doi.org/10.1029/2004JD005477, 2005.

Labow, G. J., Ziemke, J. R., McPeters, R. D., Haffner, D. P., and Bhartia, P. K.: A total ozone-dependent ozone profile climatology based on ozonesondes and Aura MLS data, Journal of Geophysical Research: Atmospheres, 120, 2537–2545, https://doi.org/10.1002/2014JD022634, 2015.

Labrador, L. J., Kuhlmann, R. V., and Lawrence, M. G. (2005), The effects of lightning-produced NOx and its vertical distribution on atmospheric chemistry: sensitivity simulations with MATCH-MPIC, *Atmos. Chem. Phys*., 5, 1815-1834.

Lacis, A. A., Wuebbles, D. J., and Logan, J. A. (1990), Radiative forcing of climate by changes in the vertical distribution of ozone, *J. Geophys. Res*., 95, 9971-9982.

Lamsal, L. N, Duncan, B. N., Yoshida, Y., Krotkov, N. A., Pickering, K. E., Streets, D. G., Zifeng Lu, Z.: U.S. NO2 trends (2005–2013): EPA Air Quality System (AQS) data versus improved observations from the Ozone Monitoring Instrument (OMI), Atmospheric Environment, https://doi.org/10.1016/j.atmosenv.2015.03.055, 2015.

Lapierre, J. L., Laughner, J. L., Geddes, J. A., Koshak, W. J., Cohen, R. C., Pusede, S. E. (2020), Observing U.S. regional variability in lightning NO$_2$ production rates, J. Geophys. Res., 125 (5), https:/doi.org/10.1029/2019JD031362.

Lavigne, T., C. Liu, and N. Liu, (2019) How does the trend in thunder days relate to the variation of lightning flash density? J. Geophys. Res. Atmos., 124, 4955–4974, https://doi.org/10.1029/2018JD029920

Lefohn, AS, Malley, CS, Smith, L, Wells, B, Hazucha, M, Simon, H, Naik, V, Mills, G, Schultz, MG, Paoletti, E, De Marco, A, Xu, X, Zhang, L, Wang, T, Neufeld, HS, Musselman, RC, Tarasick, D, Brauer, M, Feng, Z, Tang, H, Kobayashi, K, Sicard, P, Solberg, S and Gerosa, G, 2018. Tropospheric ozone assessment report: Global ozone metrics for climate change, human health, and crop/ecosystem research. Elem Sci Anth, 6: 28. DOI: 10.1525/elementa.279.

Lelieveld, J.; P. J. Crutzen (1991). The role of clouds in tropospheric photochemistry. , 12(3), 229–267. doi:10.1007/bf00048075

Liaskos, C. E., Allen, D. J., & Pickering, K. E. (2015), Sensitivity of tropical tropospheric composition to lightning NOx production as determined by replay simulations with GEOS-5, *J. Geophys. Res. Atmos*., 120, 8512–8534, doi:10.1002/2014JD022987.

Liu, J., Jose M. Rodriguez, Luke D. Oman, Anne R. Douglass, Mark A. Olsen, Lu Hu, Stratospheric impact on the Northern Hemisphere winter and spring ozone interannual variability in the troposphere, Atmospheric Chemistry and Physics, 10.5194/acp-20-6417-2020, **20**, 11, 6417-6433, 2020.

Liu, Y., Williams, E. R., Guha, A., & Said, R. (2021), How will lightning change during the pollution-reduced COVID-19 pandemic period? A data study on the global lightning activity, AGU Fall Meeting 2021.

Liu et al., (2021) https://acp.copernicus.org/articles/21/17743/2021/

Liu, J., Strode, S. A., Liang, Q., Oman, L.D., Colarco, P. R., Fleming, E. L., et al. (2022). Change in tropospheric ozone in the recent decades and its contribution to global total ozone. Journal of Geophysical Research: Atmospheres, 127, e2022JD037170. https://doi.org/10.1029/2022JD037170

Li et al. (2011) https://doi.org/10.1016/j.chnaes.2010.11.006

Luecken, D. J.; Napelenok, S. L.; Strum, M.; Scheffe, R.; Phillips, S. Sensitivity of ambient atmospheric formaldehyde and ozone to precursor species and source types across the united states. *Environ. Sci. Technol.*, *52*, 4668– 4675, DOI: 10.1021/acs.est.7b05509, 2018

Marais, E. A., Jacob, D. J., Choi, S., Joiner, J., Belmonte-Rivas, M., Cohen, R. C., et al. (2018). Nitrogen oxides in the global upper troposphere: interpreting cloud-sliced NO_2 observations from the OMI satellite instrument, *Atmospheric Chemistry and Physics*, https://doi.org/10.5194/acp-18-17017-2018

Marais, E. A., Jacob, D. J., Kurosu, T. P., Chance, K., Murphy, J. G., Reeves, C., Mills, G., Casadio, S., Millet, D. B., Barkley, M. P., Paulot, F., and Mao, J.: Isoprene emissions in Africa inferred from OMI observations of formaldehyde columns, Atmos. Chem. Phys., 12, 6219–6235, https://doi.org/10.5194/acp-12-6219-2012, 2012.

Martin, R. V., Sauvage, B., Folkins, I., Sioris, C. E., Boone, Bernath, C. P., & Ziemke, J. (2007), Space-based constraints on the production of nitric oxide by lightning, *J. Geophys. Res.*, 112, D09309, doi:10.1029/2006JD007831.

Matandirotya, N.R., Burger, R. An assessment of NO_2 atmospheric air pollution over three cities in South Africa during 2020 COVID-19 pandemic. *Air Qual Atmos Health* **16**, 263–276 (2023). https://doi.org/10.1007/s11869-022-01271-3

McDuffie, E. E., Smith, S. J., O'Rourke, P., Tibrewal, K., Venkataraman, C., Marais, E. A., Zheng, B., Crippa, M., Brauer, M., and Martin, R. V.: A global anthropogenic emission inventory of atmospheric pollutants from sector- and fuel-specific sources (1970–2017): an application of the Community Emissions Data System (CEDS), Earth Syst. Sci. Data, 12, 3413–3442, https://doi.org/10.5194/essd-12-3413-2020, 2020.

Meng, L., Liu, J., Tarasick, D. W., Randel, W. J., Steiner, A. K., Wilhelmsen, H., Wang, L., and Haimberger, L. (2021). Continuous rise of the tropopause in the Northern Hemisphere over 1980–2020. Science Advances, https://doi.org/10.1126/sciadv.abi8065, 2021.

Mills G, Pleijel H, Malley CS, Sinha B, Cooper OR, Schultz MG, Neufeld HS, Simpson D, Sharps K, Feng Z, Gerosa G, Harmens H, Kobayashi K, Saxena P, Paoletti E, Sinha V, Xu X,. Tropospheric Ozone Assessment Report: Present-day tropospheric ozone

distribution and trends relevant to vegetation. Elem Sci Anth. 2018;6(1):47. DOI: 10.1525/elementa.302.

Miyazaki, K., H. J. Eskes, K. Sudo, and C. Zhang, (2014) Global lightning NO_x production estimated by an assimilation of multiple satellite data sets, *Atmos. Chem Phys.*, 14, 3277–3305, www.atmos-chem-phys.net/14/3277/2014/doi:10.5194/acp-14-3277-2014.

Miyazaki, K., Bowman, K., Sekiya, T., Eskes, H., Boersma, F., Worden, H., Livesey, N., Payne, V. H., Sudo, K., Kanaya, Y., Takigawa, M., and Ogochi, K.: Updated tropospheric chemistry reanalysis and emission estimates, TCR-2, for 2005–2018, Earth Syst. Sci. Data, 12, 2223–2259, https://doi.org/10.5194/essd-12-2223-2020, 2020.

McPeters, R. D. and Labow, G. J.: Climatology 2011: An MLS and sonde derived ozone climatology for satellite retrieval algorithms, Journal of Geophysical Research: Atmospheres, 117, n/a-n/a, https://doi.org/10.1029/2011JD017006, 2012.

Molod, A., Takacs, L., Suarez, M., and Bacmeister, J.: Development of the GEOS-5 atmospheric general circulation model: evolution from MERRA to MERRA2, Geosci. Model Dev., 8, 1339–1356, https://doi.org/10.5194/gmd-8-1339-2015, 2015.

Murray, L. T. (2018), An uncertain future for lightning, *Nature Climate Change*, 8, 191-192.

Murray, L. T. (2016), Lightning NO_x and Impacts on Air Quality, Curr Pollution Rep (2016) 2:115–133, DOI 10.1007/s40726-016-0031-7

Murray, L. T., D. J. Jacob, J. A. Logan, R. C. Hudman, and W. J. Koshak (2012), Optimized regional and interannual variability of lightning in a global chemical transport model constrained by LIS/OTD satellite data, *J. Geophys. Res.*, 117, D20307, doi:10.1029/2012JD017934.

Nault, B. A., Garland, C., Wooldridge, J. L., Brune, W. H., Campuzano-Jost, P., Crounse, J. D., et al. (2016). Observational Constraints on the Oxidation of NO_x in the Upper Troposphere, *The Journal of Physical Chemistry A*, *120* (9), 1468-1478, doi: 10.1021/acs.jpca.5b07824

Nault, B. A., Laughner, J. L., Wooldridge, P. J., Crounse, J. D., Dibb, J., Diskin, et al. (2017). Lightning NO_x emissions: reconciling measured and modeled estimates with updated NO_x chemistry. *Geophysical Research Letters*, 44, 9479–9488.

Newton, R., Vaughan, G., Ricketts, H. M. A., Pan, L. L., Weinheimer, A. J., and Chemel, C.: Ozonesonde profiles from the West Pacific Warm Pool: measurements and validation, Atmos Chem Phys, 16, 619–634, https://doi.org/10.5194/acp-16-619-2016, 2016.

Nielsen, J. Eric, et al. "Chemical mechanisms and their applications in the Goddard Earth Observing System (GEOS) earth system model." *Journal of Advances in Modeling Earth Systems* 9.8 (2017): 3019-3044.

NOAA, https://gml.noaa.gov/ccgg/trends_ch4/, 2024. Last visited: August 2nd, 2024.

Nussbaumer, C. M., Fischer, H., Lelieveld, J., and Pozzer, A.: What controls ozone sensitivity in the upper tropical troposphere?, Atmos. Chem. Phys., 23, 12651–12669, https://doi.org/10.5194/acp-23-12651-2023, 2023.

Oleribe OO, Suliman AAA, Taylor-Robinson SD, Corrah T. Possible Reasons Why Sub-Saharan Africa Experienced a Less Severe COVID-19 Pandemic in 2020. *J Multidiscip Healthc*. 2021;14:3267-3271, https://doi.org/10.2147/JMDH.S331847, 2021.

Oltmans, SJ, Lefohn, AS, Shadwick, D, Harris, JM, Scheel, HE, et al.: Recent tropospheric ozone changes — A pattern dominated by slow or no growth, *Atmos. Environ*, 2013.

Orbe, C., Oman, L. D., Strahan, S. E., Waugh, D. W., Pawson, S., Takacs, L. L., and Molod, A. M. (2017). Large-scale atmospheric transport in GEOS replay simulations. Journal of Advances in Modeling Earth Systems, 9, 2545–2560. https://doi.org/10.1002/2017MS001053

Ott, L. E., K. E. Pickering, G. L. Stenchikov, H. Huntrieser, and U. Schumann (2007), Effects of lightning NOx production during the 21 July European Lightning Nitrogen Oxides Project storm studied with a three-dimensional cloud-scale chemical transport model, *J. Geophys. Res.*, *112*, D05307, doi:10.1029/2006JD007365.

Ott, L. E., K. E. Pickering, G. L. Stenchikov, D. J. Allen, A. J. DeCaria, B. Ridley, R.-F. Lin, S. Lang, and W.-K. Tao (2010), Production of lightning NOx and its vertical distribution calculated from three-dimensional cloud-scale chemical transport model simulations*, J. Geophys. Res.*, *115*, D04301,doi:10.1029/2009JD011880Philipona, R., C. Mears, M. Fujiwara, P. Jeannet, P. Thorne, G. Bodeker, L. Haimberger, M. Hervo, C. Popp, G. Romanens, W. Steinbrecht, R. Stubi, R. Van Malderen, adiosondes show that after decades of cooling, the lower stratosphere is now warming. J. Geophys. Res. Atmos. 123, 12509–12522 (2018).

Pickering, K. E, A. M. Thompson, R. R. Dickerson, W. T. Luke, D. P. McNamara, J. P. Greenberg, and P. R. Zimmerman, Model calculations of tropospheric ozone production potential following observed convective events, *J. Geophys. Res.*, 95:14,049-14,062, 1990.

Pickering, K. E., Y. Wang, W.-K. Tao, C. Price, and J.-F. Mueller, Vertical distributions of lightning NO_x for use in regional and global chemical transport models, *J. Geophys. Res.*, 103: 31,203-31,216, 1998.

Pickering, K. E., E. Bucsela, D. Allen, A. Ring, R. Holzworth, and N. Krotkov (2016), Estimates of lightning NO*x* production based on OMI NO_2 observations over the Gulf of Mexico, *J. Geophys. Res. Atmos.*, 121, doi:10.1002/2015JD024179.

Pickering, K. E., Y. Li, K. A. Cummings, M. C. Barth, D. J. Allen, E. Bruning, (2023) Lightning NO_x in the May 29-30, 2012 Deep Convective Clouds and Chemistry (DC3) Severe Storm and its Downwind Chemical Consequences, *J. Geophys. Res.-Atmos.*, to be submitted.

Pinto, O., Jr., K. P. Naccarato, and I. R. C. A. Pinto, 2013: Thunderstorm incidence in southeastern Brazil estimated from different data sources. Ann. Geophys., 31, 1213–1219, https://doi.org/10.5194/angeo-31-1213-2013.

Prodromos Zanis, Dimitris Akritidis, Steven Turnock, Vaishali Naik, Sophie Szopa, Aristeidis K Georgoulias, Susanne E Bauer, Makoto Deushi, Larry W Horowitz, James Keeble, Climate change penalty and benefit on surface ozone: a global perspective based on CMIP6 earth system models, Environmental Research Letters, Volume 17, Number 2, DOI: https://doi.org/10.1088/1748-9326/ac4a34.

Pollack, I. B., C. R. Homeyer, T. B. Ryerson, K. C. Aikin, J. Peischl, E. C. Apel, T. Campos, F. Flocke, R. S. Hornbrook, D. J. Knapp, et al. (2016), Airborne quantification of upper tropospheric NOx production from lightning in deep convective storms over the United States Great Plains, *J. Geophys. Res. Atmos.*, 121, 2002–2028, doi:10.1002/2015JD023941.

Prather, M. J. and D. J. Jacob (1997) A persistent imbalance in HO$_x$ and NO$_x$ photochemistry of the upper troposphere driven by deep tropical convection, *Geophys. Res. Lett.*, 24, 3189 – 3192.

Price, C., J. Penner, and M. Prather (1997), NO$_x$ from lightning 1. Global distribution based on lightning physics, *J. Geophys. Res.*, *102* (D5), 5929-5941.

Price, C. G., (2013) Lightning Applications in Weather and Climate Research, *Surv. Geophys*. (2013) 34:755–767, DOI 10.1007/s10712-012-9218-7

Putero, D., Cristofanelli, P., Chang, K.-L., Dufour, G., Beachley, G., Couret, C., Effertz, P., Jaffe, D. A., Kubistin, D., Lynch, J., Petropavlovskikh, I., Puchalski, M., Sharac, T., Sive, B. C., Steinbacher, M., Torres, C., and Cooper, O. R.: Fingerprints of the COVID-19 economic downturn and recovery on ozone anomalies at high-elevation sites in North America and western Europe, Atmos. Chem. Phys., 23, 15693–15709, https://doi.org/10.5194/acp-23-15693-2023, 2023.

Qie, K., Qie, X., & Tian, W. (2021), Increasing trend of lightning activity in the South Asian region, Science Bulletin, 66 (1), 78-84.

Qie, K., Tian, W., Wang, W., Wu, X., Yuan, T., Tian, H., Luo, J., Zhang, R., & Want, T. Regional trends of lightning activity in the tropics and subtropics, Atmos. Res., 242 (2020), Article 104960, 10.1016/j.atmosres.2020.104960

Randel, W. J., L. Polvani, F. Wu, D. E. Kinnison, C.-Z. Zou, C. Mears, Troposphere stratosphere temperature trends derived from satellite data compared with ensemble simulations from WACCM. J. Geophys. Res. Atmos. 122, 9651–9667 (2017).

Ravetta, F., G. Ancellet, A. Colette, and H. Schlager (2007), Long-range transport and tropospheric ozone variability in the western Mediterranean region during the Intercontinental Transport of Ozone and Precursors (ITOP-2004) campaign, *J. Geophys. Res.*, 112, D10S46, doi:10.1029/2006JD007724, 2007.

Ren, X., J. R. Olson, J. H. Crawford, W. H. Brune, J. Mao, R. B. Long, G. Chen, M. A. Avery, G. W. Sachse, J. D. Barrick, G. S. Diskin, L. G. Huey, Alan Fried, Ronald C. Cohen, Brian Heikes, Paul Wennberg, Hanwant B. Singh, Donald R. Blake, Richard E. Shetter,(2008) HOx Chemistry during INTEX–A 2004: Observation, Model Calculations and comparison with previous studies, *J. Geophys. Res.*, 113, D05310, doi:10.1029/2007JD009166.

Ridley, B., Ott, L., Pickering, K., Emmons, L., Montzka, D., Weinheimer, A., et al. (2004), Florida thunderstorms: A faucet of reactive nitrogen to the upper troposphere, J. Geophys. Res., 109 (D17), 10.1029/2004JD004769.

Romps, D. M., Seeley, J. T., Vollaro, D., & Molinar, J. (2014), Projected increase in lightning strikes in the United States due to global warming, *Science*, 851-854.

Romps, D. M., Charn, A. B., Holzworth, R. H., Lawrence, W. E.,Molinari, J., & Vollaro, D. (2018). CAPE times P explains lightning over land but not the land-ocean contrast.

Geophysical Research Letters, *45*, 12,623–12,630.
https://doi.org/10.1029/2018GL080267

Romps, D. M. (2019). Evaluating the future of lightning in cloud-resolving models.
Geophysical Research Letters, *46,* https://doi.org/10.1029/2019GL085748

Sanap, S. D. (2021) Global and regional variations in aerosol loading during COVID-19

imposed lockdown, *Atmos. Environ.*, 246, https://doi.org/10.1016/j.atmosenv.2020.118132.

Sauvage, B., R. V. Martin, A. van Donkelaar, and J. R. Ziemke (2007) Quantification of the
factors controlling tropical tropospheric ozone and the South Atlantic maximum, *J.
Geophys. Res.*, 112, D11309, doi:10.1029/2006JD008008.

Sanap, S. D. (2021) Global and regional variations in aerosol loading during COVID-19

imposed lockdown, *Atmos. Environ.*, 246, https://doi.org/10.1016/j.atmosenv.2020.118132.

Sauvage, B., R. V. Martin, A. van Donkelaar, and J. R. Ziemke (2007) Quantification of the
factors controlling tropical tropospheric ozone and the South Atlantic maximum, *J.
Geophys. Res.*, 112, D11309, doi:10.1029/2006JD008008.

Sanap, S. D. (2021) Global and regional variations in aerosol loading during COVID-19

imposed lockdown, *Atmos. Environ.*, 246, https://doi.org/10.1016/j.atmosenv.2020.118132.

Saunois, M., R. Stavert, A., Poulter, B., Bousquet, P., G. Canadell, J., B. Jackson, R., A.
Raymond, P., J. Dlugokencky, E., Houweling, S., K. Patra, P., Ciais, P., K. Arora, V.,
Bastviken, D., Bergamaschi, P., R. Blake, D., Brailsford, G., Bruhwiler, L., M.
Carlson, K., Carrol, M., Castaldi, S., Chandra, N., Crevoisier, C., M. Crill, P., Covey,
K., L. Curry, C., Etiope, G., Frankenberg, C., Gedney, N., I. Hegglin, M., Höglund-
Isaksson, L., Hugelius, G., Ishizawa, M., Ito, A., Janssens-Maenhout, G., M. Jensen,
K., Joos, F., Kleinen, T., B. Krummel, P., L. Langenfelds, R., G. Laruelle, G., Liu, L.,
MacHida, T., Maksyutov, S., C. McDonald, K., McNorton, J., A. Miller, P., R.
Melton, J., Morino, I., Müller, J., Murguia-Flores, F., Naik, V., Niwa, Y., Noce, S.,
O'Doherty, S., J. Parker, R., Peng, C., Peng, S., P. Peters, G., Prigent, C., Prinn, R.,
Ramonet, M., Regnier, P., J. Riley, W., A. Rosentreter, J., Segers, A., J. Simpson, I.,
Shi, H., J. Smith, S., Paul Steele, L., F. Thornton, B., Tian, H., Tohjima, Y., N.
Tubiello, F., Tsuruta, A., Viovy, N., Voulgarakis, A., S. Weber, T., Van Weele, M.,
R. Van Der Werf, G., F. Weiss, R., Worthy, D., Wunch, D., Yin, Y., Yoshida, Y.,
Zhang, W., Zhang, Z., Zhao, Y., Zheng, B., Zhu, Q., Zhu, Q., and Zhuang, Q.: The
global methane budget 2000-2017, Earth Syst Sci Data, 12,
https://doi.org/10.5194/essd-12-1561-2020, 2020.

Sauvage, B., R. V. Martin, A. van Donkelaar, and J. R. Ziemke (2007) Quantification of the
factors controlling tropical tropospheric ozone and the South Atlantic maximum, *J.
Geophys. Res.*, 112, D11309, doi:10.1029/2006JD008008.

Schumann, U., and H. Huntrieser (2007), The global lightning-induced nitrogen oxides
source, *Atmos. Chem. Phys*., 7, 3823-3907.

Seguel, R. J., Castillo, L., Opazo, C., Rojas, N. Y., Nogueira, T., Cazorla, M., Gavidia-
Calderón, M., Gallardo, L., Garreaud, R., Carrasco-Escaff, T., and Elshorbany, Y.:
Changes in South American Surface Ozone Trends: Exploring the Influences of

1849   Precursors and Extreme Events, EGUsphere [preprint],
1850   https://doi.org/10.5194/egusphere-2024-328, 2024.

1851   Sen, P (1968). Estimated of the regression coefficient based on Kendall's Tau. J Am Stat
1852   Assoc 39:1379-1389

1853   Shi, Z., H. Wang, Y. Tan, L. Li, C. Li, (2020) Influence of aerosols on lightning activities in
1854   central eastern parts of China, *Atmos Sci Lett.*, 21:e957,
1855   https://doi.org/10.1002/asl.957.

1856   Sokhi, R. S., Singh, V., Querol, X., Finardi, S., Targino, A. C., Andrade, M. de F., Pavlovic,
1857   R., Garland, R. M., Massagué, J., Kong, S., Baklanov, A., Ren, L., Tarasova, O.,
1858   Carmichael, G., Peuch, V. H., Anand, V., Arbilla, G., Badali, K., Beig, G.,
1859   Belalcazar, L. C., Bolignano, A., Brimblecombe, P., Camacho, P., Casallas, A.,
1860   Charland, J. P., Choi, J., Chourdakis, E., Coll, I., Collins, M., Cyrys, J., da Silva, C.
1861   M., Di Giosa, A. D., Di Leo, A., Ferro, C., Gavidia-Calderon, M., Gayen, A.,
1862   Ginzburg, A., Godefroy, F., Gonzalez, Y. A., Guevara-Luna, M., Haque, S. M.,
1863   Havenga, H., Herod, D., Hõrrak, U., Hussein, T., Ibarra, S., Jaimes, M., Kaasik, M.,
1864   Khaiwal, R., Kim, J., Kousa, A., Kukkonen, J., Kulmala, M., Kuula, J., La Violette,
1865   N., Lanzani, G., Liu, X., MacDougall, S., Manseau, P. M., Marchegiani, G.,
1866   McDonald, B., Mishra, S. V., Molina, L. T., Mooibroek, D., Mor, S., Moussiopoulos,
1867   N., Murena, F., Niemi, J. V., Noe, S., Nogueira, T., Norman, M., Pérez-Camaño, J.
1868   L., Petäjä, T., Piketh, S., Rathod, A., Reid, K., Retama, A., Rivera, O., Rojas, N. Y.,
1869   Rojas-Quincho, J. P., San José, R., Sánchez, O., Seguel, R. J., Sillanpää, S., Su, Y.,
1870   Tapper, N., Terrazas, A., Timonen, H., Toscano, D., Tsegas, G., Velders, G. J. M.,
1871   Vlachokostas, C., von Schneidemesser, E., VPM, R., Yadav, R., Zalakeviciute, R.,
1872   and Zavala, M.: A global observational analysis to understand changes in air quality
1873   during exceptionally low anthropogenic emission conditions, Environ Int, 157,
1874   https://doi.org/10.1016/j.envint.2021.106818, 2021.

1875   Souri, A. H., Johnson, M. S., Wolfe, G. M., Crawford, J. H., Fried, A., Wisthaler, A., Brune,
1876   W. H., Blake, D. R., Weinheimer, A. J., Verhoelst, T., Compernolle, S., Pinardi, G.,
1877   Vigouroux, C., Langerock, B., Choi, S., Lamsal, L., Zhu, L., Sun, S., Cohen, R. C.,
1878   Min, K.-E., Cho, C., Philip, S., Liu, X., and Chance, K.: Characterization of errors in
1879   satellite-based HCHONO2 tropospheric column ratios with respect to chemistry,
1880   column-to-PBL translation, spatial representation, and retrieval uncertainties,
1881   Atmospheric Chemistry and Physics, 23, 1963–1986, https://doi.org/10.5194/acp-23-
1882   1963-2023, 2023

1883   Stauffer, R. M., Thompson, A. M., Kollonige, D., Tarasick, D., Van Malderen, R., Smit, H.
1884   G. J., Vömel, H., Morris, G., Johnson, B. J., Cullis, P., and et al.: An Examination of
1885   the Recent Stability of Ozonesonde Global Network Data, Earth and Space Science
1886   Open Archive, 48, https://doi.org/10.1002/essoar.10511590.1, 2022.

1887   Steinbrecht, W., Claude, H., Köhler, U., and Hoinka, K. P.: Correlations between tropopause
1888   height and total ozone: Implications for long-term changes, J. Geophys. Res., 103,
1889   19183–19192, https://doi.org/10.1029/98JD01929, 1998.

1890   Steinbrecht, W., Kubistin, D., Plass-Dülmer, C., Davies, J., Tarasick, D. W., von der
1891   Gathen, P., et al.: COVID-19 crisis reduces free tropospheric ozone across the Northern
1892   Hemisphere. *Geophysical Research Letters*, 48, e2020GL091987.
1893   https://doi.org/10.1029/2020GL091987, 2021

Steiner, A. K., F. Ladst.dter, W. J. Randel, A. C. Maycock, Q. Fu, C. Claud, H. Gleisner, L. Haimberger, S. -P. Ho, P. Keckhut, T. Leblanc, C. Mears, L. M. Polvani, B. D. Santer, T. Schmidt, V. Sofieva, R. Wing, C. -Z. Zou, Observed temperature changes in the troposphere and stratosphere from 1979 to 2018. J. Climate 33, 8165–8194 (2020).

Stohl, A., Bonasoni, P., Cristofanelli, P., Collins, W., Feichter, J., Frank, A., Forster, C., Gerasopoulos, E., Gäggeler, H., James, P., Kentarchos, T., Kromp-Kolb, H., Krüger, B., Land, C., Meloen, J., Papayannis, A., Priller, A., Seibert, P., Sprenger, M., Roelofs, G. J., Scheel, H. E., Schnabel, C., Siegmund, P., Tobler, L., Trickl, T., Wernli, H., Wirth, V., Zanis, P., and Zerefos, C.: Stratosphere-troposphere exchange: A review, and what we have learned from STACCATO, J. Geophys. Res., 108, 8516, https://doi.org/10.1029/2002JD002490, 2003.

Strahan, S. E., Duncan, B. N., and Hoor, P. (2007). Observationally derived transport diagnostics for the lowermost stratosphere and their application to the GMI chemistry and transport model. Atmospheric Chemistry and Physics, 7(9), 2435–2445. https://doi.org/10.5194/acp-7-2435-2007.

Sue et al. 2011: https://doi.org/10.1126/science.1208839

Schultz, M.G., Schröder, S., Lyapina, O., Cooper, O., Galbally, I., Petropavlovskikh, I., von Schneidemesser, E., Tanimoto, H., Elshorbany, Y., Naja, M., Seguel, R., Dauert, U., Eckhardt, P., Feigenspahn, S., Fiebig, M., Hjellbrekke, A.-G., Hong, Y.-D., Christian Kjeld, P., Koide, H., Lear, G., Tarasick, D., Ueno, M., Wallasch, M., Baumgardner, D., Chuang, M.-T., Gillett, R., Lee, M., Molloy, S., Moolla, R., Wang, T., Sharps, K., Adame, J.A., Ancellet, G., Apadula, F., Artaxo, P., Barlasina, M., Bogucka, M., Bonasoni, P., Chang, L., Colomb, A., Cuevas, E., Cupeiro, M., Degorska, A., Ding, A., Fröhlich, M., Frolova, M., Gadhavi, H., Gheusi, F., Gilge, S., Gonzalez, M.Y., Gros, V., Hamad, S.H., Helmig, D., Henriques, D., Hermansen, O., Holla, R., Huber, J., Im, U., Jaffe, D.A., Komala, N., Kubistin, D., Lam, K.-S., Laurila, T., Lee, H., Levy, I., Mazzoleni, C., Mazzoleni, L., McClure-Begley, A., Mohamad, M., Murovic, M., Navarro-Comas, M., Nicodim, F., Parrish, D., Read, K.A., Reid, N., Ries, L., Saxena, P., Schwab, J.J., Scorgie, Y., Senik, I., Simmonds, P., Sinha, V., Skorokhod, A., Spain, G., Spangl, W., Spoor, R., Springston, S.R., Steer, K., Steinbacher, M., Suharguniyawan, E., Torre, P., Trickl, T., Weili, L., Weller, R., Xu, X., Xue, L. and Zhiqiang, M., Tropospheric Ozone Assessment Report: Database and Metrics Data of Global Surface Ozone Observations. 2017. Elem Sci Anth, 5, p.58. DOI: 10.1525/elementa.244.

Szopa, S., Naik, V., Adhikary, B., Artaxo, P., Berntsen, T., Collins, W.D., Fuzzi, S., Gallardo, L., Kiendler-Scharr, A., Klimont, Z., Liao, H., Unger, N., and Zanis, P.: Short-Lived Climate Forcers. In *Climate Change 2021:* The Physical Science Basis. Contribution of Working Group I to the Sixth Assessment Report of the Intergovernmental Panel on Climate Change [Masson-Delmotte, V., P. Zhai, A. Pirani, S.L. Connors, C. Péan, S. Berger, N. Caud, Y. Chen, L. Goldfarb, M.I. Gomis, M. Huang, K. Leitzell, E. Lonnoy, J.B.R. Matthews, T.K. Maycock, T. Waterfield, O. Yelekçi, R. Yu, and B. Zhou (eds.)]. Cambridge University Press, Cambridge, United Kingdom and New York, NY, USA, pp. 817–922, doi:10.1017/9781009157896.008, 2021.

Tarasick, D., Galbally, I.E., Cooper, O.R., Schultz, M.G., Ancellet, G., Leblanc, T., Wallington, T.J., Ziemke, J., Liu, X., Steinbacher, M., Staehelin, J., Vigouroux, C., Hannigan, J.W., García, O., Foret, G., Zanis, P., Weatherhead, E., Petropavlovskikh, I., Worden, H., Osman, M., Liu, J., Chang, K.-L., Gaudel, A., Lin, M., Granados-Muñoz, M., Thompson, A.M., Oltmans, S.J., Cuesta, J., Dufour, G., Thouret, V., Hassler, B., Trickl, T. and Neu, J.L., 2019. Tropospheric Ozone Assessment Report: Tropospheric ozone from 1877 to 2016, observed levels, trends and uncertainties. Tropospheric Ozone Assessment Report: Tropospheric ozone from 1877 to 2016, observed levels, trends and uncertainties. Elem Sci Anth, 7(1), p.39. DOI : 10.1525/elementa.376, 2019.

Thompson, A. M., Witte, J. C., Sterling, C., Jordan, A., Johnson, B. J., Oltmans, S. J., Fujiwara, M., Vömel, H., Allaart, M., Piters, A., Coetzee, G. J. R., Posny, F., Corrales, E., Diaz, J. A., Félix, C., Komala, N., Lai, N., Ahn Nguyen, H. T., Maata, M., Mani, F., Zainal, Z., Ogino, S., Paredes, F., Penha, T. L. B., Silva, F. R., Sallons-Mitro, S., Selkirk, H. B., Schmidlin, F. J., Stübi, R., and Thiongo, K.: First Reprocessing of Southern Hemisphere Additional Ozonesondes (SHADOZ) Ozone Profiles (1998–2016): 2. Comparisons With Satellites and Ground-Based Instruments, Journal of Geophysical Research: Atmospheres, 122, https://doi.org/10.1002/2017JD027406, 2017.

Tsivlidou, M., Sauvage, B., Barret, B., Wolff, P., Clark, H., Bennouna, Y., Blot, R., Boulanger, D., Nédélec, P., Le Flochmoën, E., and Thouret, V.: Tropical tropospheric ozone and carbon monoxide distributions: characteristics, origins and control factors, as seen by IAGOS and IASI, Atmos. Chem. Phys. Discuss. (preprint), https://doi.org/10.5194/acp-2022-686, in review, 2022.

Turnock, S. T., Allen, R. J., Andrews, M., Bauer, S. E., Deushi, M., Emmons, L., Good, P., Horowitz, L., John, J. G., Michou, M., Nabat, P., Naik, V., Neubauer, D., O'Connor, F. M., Olivié, D., Oshima, N., Schulz, M., Sellar, A., Shim, S., Takemura, T., Tilmes, S., Tsigaridis, K., Wu, T., and Zhang, J.: Historical and future changes in air pollutants from CMIP6 models, Atmos. Chem. Phys., 20, 14547–14579, https://doi.org/10.5194/acp-20-14547-2020, 2020.

Theil, H. (1950), "A rank-invariant method of linear and polynomial regression analysis. I, II, III", Nederl. Akad. Wetensch., Proc., 53: 386–392, 521–525, 1397–1412.

Trickl, T., Bärtsch-Ritter, N., Eisele, H., Furger, M., Mücke, R., Sprenger, M., and Stohl, A.: High-ozone layers in the middle and upper troposphere above Central Europe: potential import from the stratosphere along the subtropical jet stream, Atmos. Chem. Phys., 11, 9343–9366, https://doi.org/10.5194/acp-11-9343-2011, 2011.

Verma, S., Yadava, P. K., Lal, D. M., Mall, R. K., Harshbardhan, K., & Payra, S. (2021), Role of Lightning NO_x in ozone formation: A review, Pure and Applied Geophysics, 178, 1425-1443.

Wang, H., Shi, Z., Wang, X., Tan, Y., Wang, H., Li, L., & Lin, X. (2021), Cloud-to-Ground Lightning Response to Aerosol over Air-Polluted Urban Areas in China. *Remote Sens. 13*, 2600. https://doi.org/10.3390/rs13132600

Wang, H., Lu, X., Jacob, D. J., Cooper, O. R., Chang, K.-L., Li, K., Gao, M., Liu, Y., Sheng, B., Wu, K., Wu, T., Zhang, J., Sauvage, B., Nédélec, P., Blot, R., and Fan, S.: Global

tropospheric ozone trends, attributions, and radiative impacts in 1995–2017: an integrated analysis using aircraft (IAGOS) observations, ozonesonde, and multi-decadal chemical model simulations, Atmos Chem Phys, 22, 13753–13782, https://doi.org/10.5194/acp-22-13753-2022, 2022.

Wang, Y., A. W. DeSilva, G. C. Goldenbaum, and R. R. Dickerson, (1998) Nitric oxide production by simulated lightning: Dependence on current, energy, and pressure, *J. Geophys. Res.,* 103, 19,149-19,159.

Wilcox, R. (2001). Fundamentals of Modern Statistical Methods: Substantially Improving Power and Accuracy. Springer Science and Business Media.

Williams, R. S., Hegglin, M. I., Kerridge, B. J., Jöckel, P., Latter, B. G., and Plummer, D. A.: Characterising the seasonal and geographical variability in tropospheric ozone, stratospheric influence and recent changes, Atmos. Chem. Phys., 19, 3589–3620, https://doi.org/10.5194/acp-19-3589-2019, 2019.

Wu, D., Zhang, J., Wang, M., An, J., Wang, R., Haider, H., et al. (2022). Global and regional patterns of soil nitrous acid emissions and their acceleration of rural photochemical reactions. Journal of Geophysical Research: Atmospheres, 127, e2021JD036379. https://doi.org/10.1029/2021JD036379

WMO, 1992, International Meteorological Vocabulary (2nd ed.), Geneva: Secretariat of the World Meteorological Organization. 1992. p. 636. ISBN 978-92-63-02182-3)

Wang and Chen, 2012: https://doi.org/10.1016/j.geoderma.2011.11.009

Xue, X., Ren, G. Y., Xu, X. D., Sun, X. B., Yang, G. W., Zhang, P. F., & Zhang, S. Q. (2021), The trends of warm-season thunderstorm and lightning days in China and the influence of environmental factors, J. Geophys. Res., 126 (15), 10.1029/2021JD034950.

Yang, X., and Z. Li, 2014: Increases in thunderstorm activity and relationships with air pollution in southeast China*, J. Geophys. Res. Atmos.*, 119, 1835–1844, doi:10.1002/2013JD021224.

Yin, Y., Chevallier, F., Ciais, P., Broquet, G., Fortems-Cheiney, A., Pison, I., and Saunois, M.: Decadal trends in global CO emissions as seen by MOPITT, Atmos. Chem. Phys., 15, 13433–13451, https://doi.org/10.5194/acp-15-13433-2015, 2015.

Young, P.J., Naik, V., Fiore, A.M., Gaudel, A., Guo, J., Lin, M.Y., Neu, J.L., Parrish, D.D., Rieder, H.E., Schnell, J.L., Tilmes, S., Wild, O., Zhang, L., Ziemke, J.R., Brandt, J., Delcloo, A., Doherty, R.M., Geels, C., Hegglin, M.I., Hu, L., Im, U., Kumar, R., Luhar, A., Murray, L., Plummer, D., Rodriguez, J., Saiz-Lopez, A., Schultz, M.G., Woodhouse, M.T. and Zeng, G. Tropospheric Ozone Assessment Report: Assessment of global-scale model performance for global and regional ozone distributions, variability, and trends. 2018. Elem Sci Anth, 6(1), p.10. DOI: 10.1525/elementa.265.

Zeng, G., Morgenstern, O., Braesicke, P., Pyle, J.A., 2010. Impact of stratospheric ozone recovery on tropospheric ozone and its budget: impact of ozone recovery on tropospheric ozone. Geophys. Res. Lett. 37, n/a-n/a. https://doi.org/10.1029/2010GL042812.

2024 Yetong Li, Yan Xia, Fei Xie, Yingying Yan, Influence of stratosphere-troposphere exchange
2025 on long-term trends of surface ozone in CMIP6, Atmospheric Research, 297, doi:
2026 https://doi.org/10.1016/j.atmosres.2023.107086, 2024.

2027 Zhang, X., Yin, Y., van der A, R., Lapierre, J. L., Chen, Q., Kuang, X., Yan, S., Chen, J., He,
2028 C., and Shi, R. (2020), Estimates of lightning NO_x production based on high-
2029 resolution OMI NO_2 retrievals over the continental US, Atmos. Meas. Tech., 13,
2030 1709–1734, https://doi.org/10.5194/amt-13-1709-2020 .

2031 Zhang et al., 2020: https://doi.org/10.1016/j.atmosenv.2020.117596

2032 Zhang, L., T. Wang, Q. Zhang, J. Zheng, Z. Xu, and M. Lv (2016), Potential sources of nitrous
2033 acid (HONO) and their impacts on ozone: A WRF-Chem study in a polluted subtropical
2034 region, J. Geophys. Res. Atmos., 121, 3645–3662, doi:10.1002/2015JD024468.

2035 Zheng, B.; Chevallier, F.; Yin, Y.; Ciais, P.; Fortems-Cheiney, A.; Deeter, M.N.; Parker,
2036 R.J.; Wang, Y.; Worden, H.M.; Zhao, Y. Global atmospheric carbon monoxide
2037 budget 2000-2017 inferred from multi-species atmospheric inversions. *Earth Sys. Sci.*
2038 *Data*, *11*, 1411–1436, https://doi.org/10.5194/essd-11-1411-2019, 2019